# DEVELOPMENT OF A FIBRE OPTICS DAYLIGHTING/HIGH-CONCENTRATION PHOTOVOLTAIC DEVICE


Università
di Catania

**GIUSEPPE MATTIA LO PICCOLO**

**Ph.D. 2021**

Università di Catania

# DEVELOPMENT OF A FIBRE OPTICS DAYLIGHTING/HIGH-CONCENTRATION PHOTOVOLTAIC DEVICE

*Submitted in partial fullfilment of the requirements for the degree of Doctor of Philosophy (Ph.D.) in Material Science and Nanotechnology*


*Author*:

Giuseppe Mattia Lo Piccolo

*Advisors*:

Simonpietro Agnello

Marco Cannas



UNIONE EUROPEA
Fondo Sociale Europeo

Ministero dell'Università e della Ricerca

PON RICERCA E INNOVAZIONE 2014 - 2020

*One of the greatest challenge in this world is knowing enough about a subject to think you are right but not enough about the subject to know you are wrong.*

NEIL DEGRASSE TYSON

# Contents

# Introduction

In recent years, the climate change has become one of the most important issues and the need for new technologies based on renewable energy sources is now accepted by the world community. A clear example of this "clean energy revolution" is the recent development of high-concentration photovoltaic (HCPV) systems for the electricity supply of commercial and residential buildings. These devices are generally on a primary optics which concentrates the sunlight onto highly efficient photovoltaic cells for its conversion into electric energy. Multi-junction cells are often preferred to traditional single-junction cells due to their ability to absorb a wider portion of the solar spectrum and guarantee a higher conversion efficiency. However, their fragile layered structure is highly sensible to adverse weather and environmental conditions and they are often subject to physical damaging when exposed to moisture, pollutants, thermal, or mechanical stress. A possible solution to this problem is to remove the cells from the HCPV support structure and install them in a sheltered place where external conditions are more easily controlled. By doing this, the transport of light from the concentrator to the cells would be left to waveguides having both a high transparency in the solar spectral range and a high resistance to concentrated light. In this scenario, the transmitted light may be used not only for current generation but also to directly illuminate interior spaces without the need of artificial lighting. In this way, the new fibre optics-based system may function as an hybrid device featuring both a daylighting (DL) and an HCPV function. Recent studies report the use fibre optics-based daylighting systems used to illuminate indoor environments with natural light. However, these prototypes only focus on low concentration light transmission and therefore they are not able to meet the light demand of a building without the aid of artificial lighting.

The objective of this research is to extend the use of optical fibres to HCPV sys-

tems and develop a proof-of-concept hybrid DL/HCPV module for the illumination and energy supply of buildings. More in detail, we aimed at upgrading an existing outdoor HCPV system and convert it into an hybrid system. The strategy adopted to achieve this goal covers several front topics and can be outlined as follows:

- Optimisation of the concentrator–optical fibre coupling;
- Transmission and resistance tests on optical fibres;
- Development of a prototypical DL/HCPV module.

This thesis is divided into six chapters. Chapters 1 and 2 are dedicated, respectively, to the discussion of the existing solar-energy-based technologies and the structural and optical properties of silica glasses. The photo-induced creation of point defects is also reviewed, with a particular emphasis on the defects absorbing ultraviolet and visible light. Chapter 3 provides the detailed description of the current HCPV system and the set-ups used for the measurements. In Chapter 4, 5, and 6 the experimental results are presented and discussed. The subdivision of these chapters reflects the three different stages of the investigation which can be summarised as: (i) the ray-tracing study of the HCPV system and its upgrade with different secondary optics; (ii) the investigation of the effect of broad-band and monochromatic concentrated light on optical fibres; and (iii) the realisation and performance evaluation of the fibre-based DL/HCPV module.

This project was funded by the Italian National Operational Programme for “Research and Innovation” (PON R&I 2014–2020) under grant agreement No. DOT1308583 and was developed in line with the strategic objectives of the European Framework Programme Horizon 2020. The research was developed together with the industrial partner IDEA Srl and the academic partner “Université Jean Monnet Saint-Étienne” which greatly contributed to the preliminary study and development of the hybrid DL/HCPV module.

# Chapter 1

# Solar energy technologies

## 1.1 The current world energy situation

Modern society is based on the capability of humankind to convert energy from one form to another. Since the Second Industrial Revolution (1870–1914), the development of the electricity sector and the greater use of fossil fuels has shaped the society structure and supported the progress towards a better quality of life. According to the bp Statistical Review of World Energy 2020 [1], the global primary energy consumption (PEC) in 2019 was of 162,194 TWh. China was the world's biggest driver of energy, accounting for 24% of the overall consumption. The United States and Europe were the next two largest contributors with a share of approximately 16% and 14%, respectively. Despite an annual increase of 2131 TWh, 2019's PEC growth rate slowed down to 1.3%, less than half of the rate recorded in the previous year (2.8%). This drop was mainly due to the general downtrend of global economy and a reduced energy consumption in the industry and building sectors. In fact, due to a warmer winter, the energy required for space and water heating decreased, and so did the demand for fuels for electricity generation [2]. Oil continued to be the most significant energy source, holding a 33.1% share of the energy mix (Fig. 1.1). Coal hit the lowest level (27.0%) since 2003 while natural gas and renewables shares rose to record highs of 24.2% and 5.0%, respectively. Nuclear energy lagged behind with only 4.3% of the market share and hydroelectricity kept stable at around 6%.

As of 2018, the buildings and construction sector accounted for 36% of the total energy consumption and 39% of carbon dioxide emissions [3, 4]. Without any

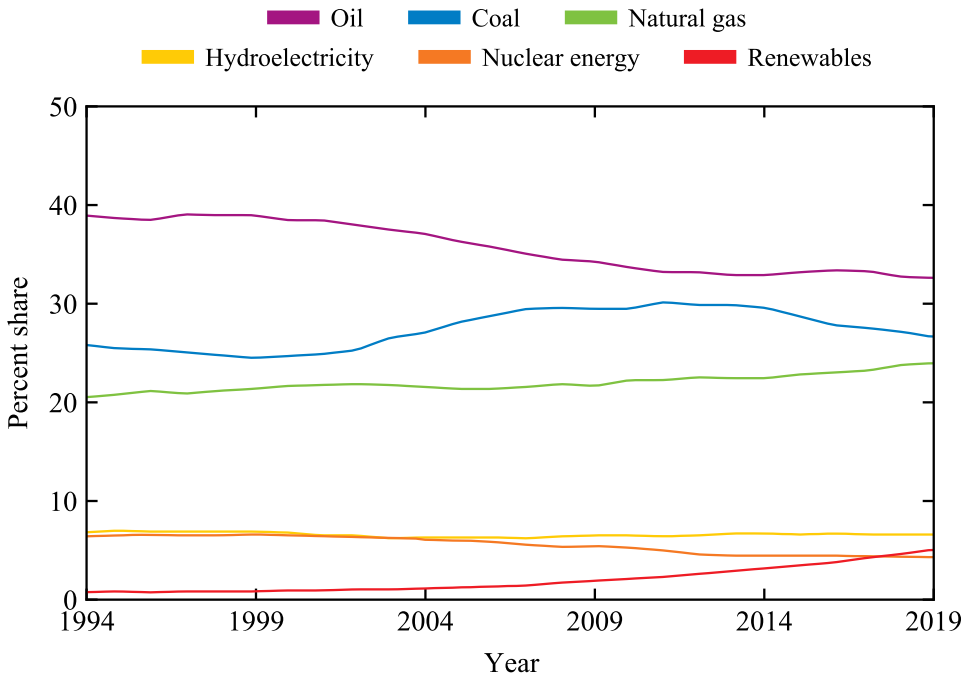


**Figure 1.1.** Shares of global primary energy consumption by fuel [1].

further climate policies, the final energy use of buildings is expected to grow 1% per annum, reaching a PEC share of around 48% by 2050. Conversely, by adopting new measures aimed at reducing carbon emissions by over 95% in the next 30 years, the increase of energy use in buildings will be limited to 0.1% per annum [4]. This latter case is called the "Net Zero Scenario" and is characterised by the progressive decline of traditional energy sources in favour of green energy-based technologies. It will bring renewables to a primary energy share of 30% to 60%, with solar and wind power dominating the market with an overall installed capacity of up to 14 TW [4, 5].

## 1.2 Solar radiation

The Sun is a sphere of intensely hot gases of radius $R_\odot = 6.957 \times 10^8$ m lying at the centre of the Solar System at an average distance $D_{se} = 1.495 \times 10^{11}$ m from the Earth. Its effective temperature, *i.e.* the temperature of a black body emitting the same amount of energy, is 5777 K. The source of this energy is the nuclear fusion taking place in its core where, every second, $6.00 \times 10^{11}$ kg of hydrogen is converted into $5.96 \times 10^{11}$ kg of helium. The missing $4 \times 10^9$ kg are converted to heat and light which propagate outwards in every direction. In order to describe how energy flows from the Sun to the Earth — and in general from a source to a receiving surface — some basic radiometric and photometric concepts need to be

introduced first.

**Radiant energy,** $Q$

Energy emitted, reflected, transmitted, or received in the form of electromagnetic waves. In the SI system it is measured in joule (J).

**Radiant flux or radiant power,** $\Phi$

Radiant energy per unit time transferred from a surface or point to another surface or point:

$$\Phi = \frac{\partial Q}{\partial t}. \qquad [\mathrm{W}]$$

Its SI unit is the watt (W). The corresponding photometric quantity is the **luminous flux** ($\Phi_\mathrm{v}$) which is the measure of the power of light as perceived by the human eye. It can be directly measured with a lux meter or calculated by weighting the radiant flux for the spectral response of the eye. Its international unit of measurement is the lumen (lm).

**Radiance,** $L$

Radiant flux emitted, reflected, transmitted, or received by a surface per unit solid angle ($\partial\Omega$) per unit projected area ($\partial A \cos\theta$):

$$L = \frac{\partial^2 \Phi}{\partial\Omega\, \partial A \cos\theta}. \qquad \left[\frac{\mathrm{W}}{\mathrm{sr}\cdot\mathrm{m}^2}\right]$$

It can be expressed as a function of the wavelength ($\lambda$), in which case it is called spectral radiance:

$$L_\lambda = \frac{\partial L}{\partial \lambda}. \qquad \left[\frac{\mathrm{W}}{\mathrm{sr}\cdot\mathrm{m}^2\cdot\mathrm{nm}}\right]$$

**Irradiance or flux density,** $E$

Radiant flux received by a surface per unit area. If we define the projected solid angle as $\cos\theta\, d\Omega$, the irradianced can be calculated as:

$$E = \frac{\partial \Phi}{\partial A} = \int L \cos\theta\, d\Omega. \qquad \left[\frac{\mathrm{W}}{\mathrm{m}^2}\right]$$

Its partial derivative with respect to the wavelength is called spectral irradiance and is defined as

$$E_\lambda = \frac{\partial E}{\partial \lambda}. \qquad \left[\frac{\mathrm{W}}{\mathrm{m}^2\cdot\mathrm{nm}}\right]$$

In photometry, the total luminous flux incident on a surface per unit area is called **illuminance** ($E_\mathrm{v}$) and is measured in lux ($\mathrm{lx} = \mathrm{lm}\cdot\mathrm{m}^{-2}$).

**Radiosity, $J$**

Radiant flux leaving a surface per unit area. Considering that radiation can be emitted, reflected, or transmitted by the surface, the radiosity is defined as

$$J = \frac{\partial \Phi}{\partial A} = J_{em} + J_r + J_{tr}, \qquad \left[\frac{\mathrm{W}}{\mathrm{m}^2}\right]$$

$J_{em}$ is also called the **excitance** ($M$) and corresponds to the emitted component of the radiosity of the surface.

According to these definitions, the energy produced by the Sun can be expressed in terms of the radiant flux emitted by its surface, which is equal to $3.83 \times 10^{26}$ W. Due to the spatial relation between the Earth and the Sun, only a small portion of this flux reaches our eyes. The air mass zero irradiance ($E_{\mathrm{AM0}}$) is the solar irradiance received by a surface perpendicular to the Sun's rays at the edge of the Earth's atmosphere. Its value is nearly constant throughout the year and is equal to $1367\ \mathrm{W \cdot m^{-2}}$ [6]. In the solar photovoltaics community, this quantity is often referred to as the solar constant or the average total solar irradiance. By reporting $E_{\mathrm{AM0}}$ as a function of the wavelength we obtain the extraterrestrial AM0 solar spectrum shown in Fig. 1.2 . The other spectra shown in the figure are discussed below.

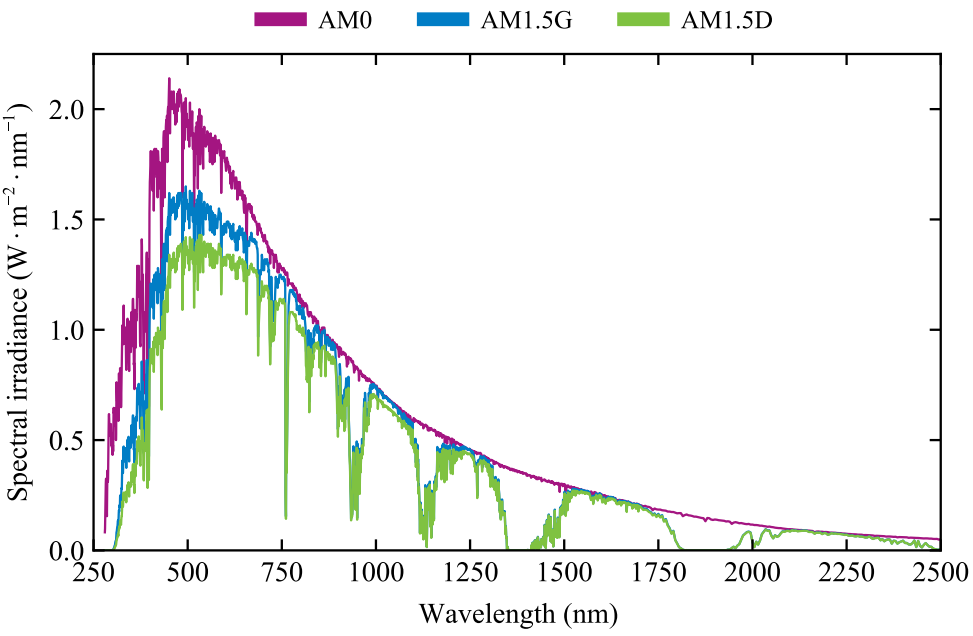


**Figure 1.2.** Spectral irradiance for the ASTM G–173–03 standard extraterrestrial (AM0), global (AM1.5G), and direct + circumsolar (AM1.5D) solar spectra [7].

When sunlight passes through Earth's atmosphere, a significant amount of radiation is lost due to (i) selective gaseous absorption, (ii) molecular (Rayleigh) scat-

tering, and (iii) particle (Mie) scattering [8]. The first phenomenon is caused by gasses such as $O_2$, $O_3$, $H_2O$, and $CO_2$ which absorb ultraviolet (UV) and infrared (IR) light and reduce the solar flux at the ground by $\sim$23%. Rayleigh scattering is proportional to $\lambda^{-4}$ and its effects on atmospheric transmittance is significant only at $\lambda < 600\,\text{nm}$. Since shorter wavelengths are more strongly scattered than longer wavelength, blue light is deviated more efficiently than red light and this causes the sky to appear blue. On the contrary, the intensity of Mie scattering depends only weakly on $\lambda$ and becomes independent of it when the size of the particle exceeds the wavelength of the incoming radiation. A typical example of this phenomenon is the white colour of clouds determined by the scattering from water droplets [9]. The portion of scattered sunlight redirected towards the Earth is called the diffuse radiation. On average, it accounts for 10% of the light reaching the ground. The remaining part corresponds to the direct beam solar radiation, that is the light directly coming from the Sun without being scattered (see Fig. 1.3). The sum of the diffuse and direct solar radiation is called the global solar radiation.

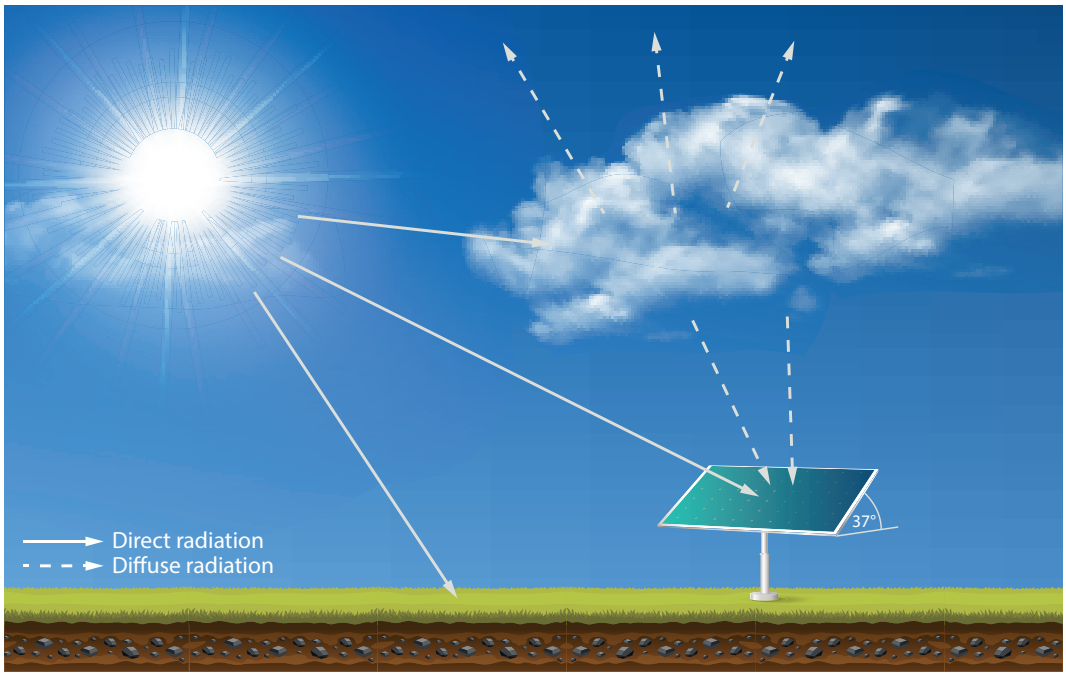


**Figure 1.3.** Schematic diagram of the components of solar radiation through the atmosphere. Solid lines represent direct solar radiation while dashed lines represent diffuse radiation. The receiving surface is tilted 37° from the horizontal as specified by the ASTM standard.

The energy delivered by direct radiation depends on the path length through the atmosphere. When the Sun is at the zenith (zenith angle $\theta_s = 0$), its rays are perpendicular to the Earth's surface and the shortest path ($D_0$) is achieved. In this case the sunlight is said to go through one atmosphere or one air mass (AM1). If sunlight

arrives on Earth with a $\theta_s$ greater than zero, it must travel a longer path ($D$) through the atmosphere and the corresponding air mass coefficient is given by

$$\mathrm{AM} = \frac{D}{D_0} \approx \frac{1}{\cos\theta_s}. \tag{1.1}$$

Considering that photovoltaic systems do not generally operate under exactly one atmosphere thickness, an air mass of 1.5 has been chosen as a standard value to compare the performance of different photovoltaic cells and modules [10]. The corresponding AM1.5 spectra are defined as received by an inclined plane tilted 37° from the horizontal towards the equator [10]. The American Society for Testing and Materials (ASTM), in conjunction with the scientific and photovoltaic community, developed a set of standard solar spectra called ASTM G–173–03 featuring the extraterrestrial spectral irradiance (AM0), the global spectral irradiance (AM1.5G), and the direct spectral irradiance (AM1.5D) [7]. For convenience, the second spectrum is normalised to a total irradiance of $1000\,\mathrm{W}\cdot\mathrm{m}^{-2}$ while the third is adjusted to have an integrated irradiance of $900\,\mathrm{W}\cdot\mathrm{m}^{-2}$. These values are commonly referred to as the global normal irradiance (GNI) and direct normal irradiance (DNI). The three ASTM standard spectra are shown in Fig. 1.2.

The geometrical properties of sunlight beams depend on the specific geometry of the Sun–Earth system. If the distance between the two celestial bodies were infinite, the Sun would be a point-like source and its light would arrive to the Earth as a perfectly collimated beam. Since this is not the case, the Sun appears to us as a disk of angular radius

$$\xi_s = \frac{R_\odot}{D_{se}} \approx 4.653\,\mathrm{mrad} \tag{1.2}$$

where $R_\odot$ is the solar radius and $D_{se}$ is the average Sun–Earth distance. The exact value of $\xi_s$ depends on $D_{se}$ and varies seasonally due to the eccentricity of Earth's orbit. The variation, however, is small ($\sim$1.7%) and for all practical application $\xi_s$ can be considered constant. As shown in Fig. 1.4, the finite dimension of the solar disk implies that the direct sunlight reaching the Earth is confined to a cone of half-angle 4.653 mrad.

Under the assumption of radial symmetry and homogeneous flux, the light received by a flat surface on the Earth can be modelled by the function:

$$\bar{L}(\xi) = \begin{cases} 1, & \text{for } 0 \le \xi \le \xi_s \\ \\ 0, & \text{for } \xi > \xi_s \end{cases} \tag{1.3}$$

where $\bar{L}$ is the normalised solar radiance and $\xi$ is the angular distance from the centre of the Sun. This distribution is known as pillbox sunshape (purple line in Fig. 1.5) and is typical of a perfect black-body radiator [11]. In reality, $\bar{L}(\xi)$ does not go to zero but rather tends asymptotically to zero as $\xi \to \infty$. This behaviour is

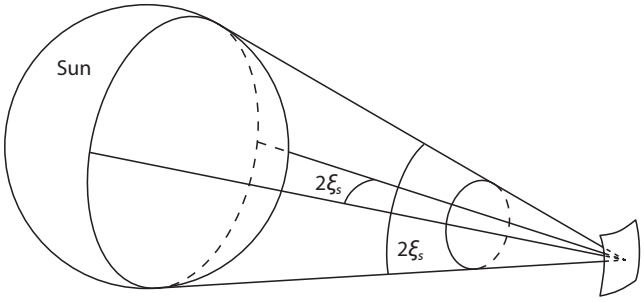


**Figure 1.4.** Geometry of the sun rays as viewed from the Earth.

determined by the limb darkening effect, that is the optical phenomenon causing a gradual dimming of the Sun's luminosity at the edge (limb) of the solar disk. The region of the sky in the vicinity of the solar disk edge has a non-zero radiance and is called the circumsolar region or aureole. The radiation coming from this region is generally considered as part of the direct solar beam and is thus included in most standard spectra (*e.g.* the AM1.5D solar spectrum).

In order to mathematically model the limb-darkened distribution, Buie *et al.* [12] analysed a large number of spectra collected by the Lawrence Berkeley Laboratory [13] and the German Aerospace Centre [14] and proposed the following parametric function:

$$\bar{L}(\xi) = \begin{cases} \dfrac{\cos(0.326\,\xi)}{\cos(0.308\,\xi)}, & \text{for } 0 \leq \xi \leq \xi_s \\ e^{\kappa}\,\xi^{\gamma}, & \text{for } \xi > \xi_s \end{cases} \tag{1.4}$$

where $\gamma$ and $\kappa$ are defined as

$$\kappa = 0.9\ln(13.5\,\mathrm{CSR})\,\mathrm{CSR}^{-0.3} \tag{1.5}$$

$$\gamma = 2.2\ln(0.52\,\mathrm{CSR})\,\mathrm{CSR}^{0.43} - 0.1. \tag{1.6}$$

The circumsolar ratio (CSR) is defined as the ratio between the circumsolar radiance and the global radiance. It depends on many factors (atmospheric conditions, air mass, location, time) but its value for a cloudless sky is generally between 0 and 0.04 [15]. The sunshape obtained from Eq. (1.4) by imposing a CSR of 0.02 is shown in Fig. 1.5.

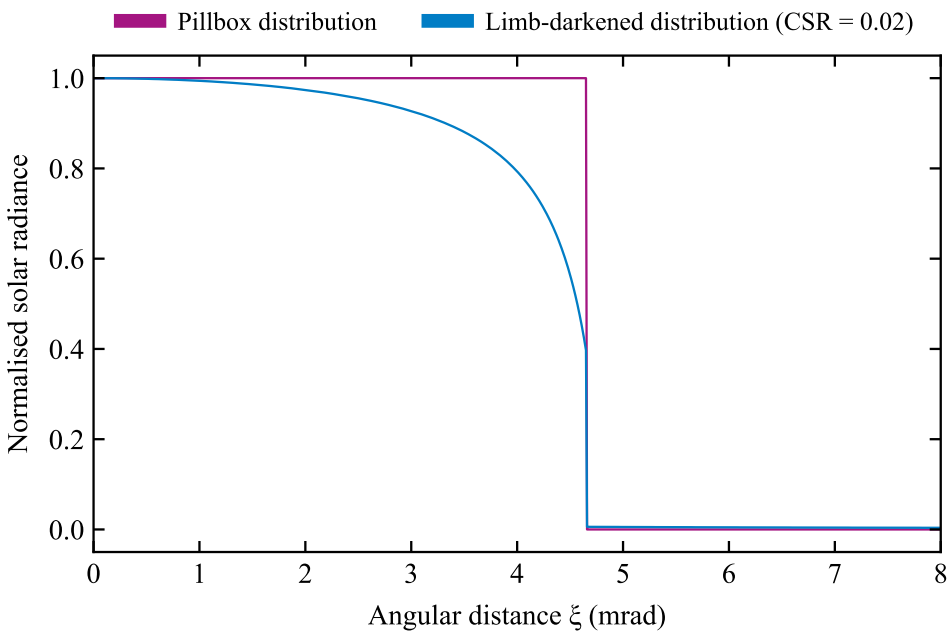


**Figure 1.5.** Pillbox and limb-darkened sunshape profiles.

## 1.3 Concentrating photovoltaics

The levelised cost of electricity from solar photovoltaics (PV) has fallen over the past decade from \$0.378/kWh to the current value of \$0.068/kWh [16]. As a result, the global solar PV capacity reached the record level of 627 GW in 2019, becoming the most competitive option for electricity generation in a wide number of markets [17]. Today, most PV installations use solar panels made of either monocrystalline or amorphous silicon solar cells to generate electricity with efficiencies of about 25% [18]. The technical limitations of these systems, however, push the solar energy industry towards the development of new, more efficient devices such as the concentrating photovoltaic (CPV) systems. This technology established its presence in the energy market in 2006 and today accounts for a total installed capacity of 350 MW [19, 20]. Unlike flat-plate panels, CPV makes use of optical devices to concentrate solar radiation on small solar cells and generate electricity with much higher efficiencies (30% to 43%) [21].

The most important property of a CPV system is the optical concentration ratio, that is the ratio of the irradiance emitted by the concentrating optics ($E_C$) to the irradiance received by the solar cell ($E_A$, where A stands for absorber) [22, 23]. It can be considered as a measure of the system ability to concentrate solar energy and is calculated as

$$C_o = \frac{E_C}{E_A}. \tag{1.7}$$

Since the flux received by the concentrator is in principle equal to that received by

the absorber, the concentration ratio can be expressed as the ratio of the collector aperture to the absorber area:

$$C_g = \frac{A_C}{A_A}. \tag{1.8}$$

According to the concentration ratio, CPV systems are usually classified as:

- Low-concentration photovoltaics (LCPV): $2\times \leq C_g < 10\times$,
- Medium-concentration photovoltaics (MCPV): $10\times \leq C_g < 100\times$,
- High-concentration photovoltaics (HCPV): $100\times \leq C_g < 2000\times$.

LCPV systems are typically based on lightweight structural components and have simple and practical designs. They mostly rely on silicon solar cells and do not require tracking or cooling systems. This makes LCPV a cheap and easy-to-maintain technology which is especially suited for stand-alone applications and building integration [24]. A major drawback of these systems is the low conversion efficiency determined by both the low $C_g$ and the absence of a tracking system. Examples of LCPV systems are compound parabolic concentrators [25–27], prism-based concentrators [28, 29], and V-troughs [30–32].

HCPV is the most recent of the concentrating technologies and is also the one that can potentially bolster new market segments [33]. Since their first appearance, the development of high-concentration systems has been tightly bound to that of multijunction (MJ) solar cells. In fact, while LCPV systems can work with crystalline silicon solar cells, the higher flux densities reached by HCPV systems require the use of new-generation solar cells able to absorb a wider spectrum of sunlight. This ensures a high energy yield per module active area, a high potential market growth rate, and consequently a high potential deployment [33, 34]. On the other hand, these systems are more expensive than conventional PV and are most suited for desert-like areas where smog and dust are not an issue. In addition, the high-precision tracking system needed to get maximum solar energy hinder their building integrability and relegate them to be installed only on rooftops [35]. Medium-concentration photovoltaics stands somewhere in between LCPV and HCPV as for efficiency and weaknesses. In some cases, MCPV systems are used to support the energy demand of buildings but, due to their size, they are more difficult to integrate into buildings than LCPV systems [35].

The general scheme of a concentrating PV system is shown in Fig. 1.6. Even though the terms ‘module’ and ‘system’ are frequently interchanged, technically a module is defined as the assembly comprising the concentrator, the receiver, and their housing structure. Several modules electrically connected and mounted on a supporting (or tracking) structure form a properly called system. The concentrator or primary optical element (POE) is the optical device that harvests sunlight and focuses it on the receiver. Refractive concentrators are usually based on Fresnel

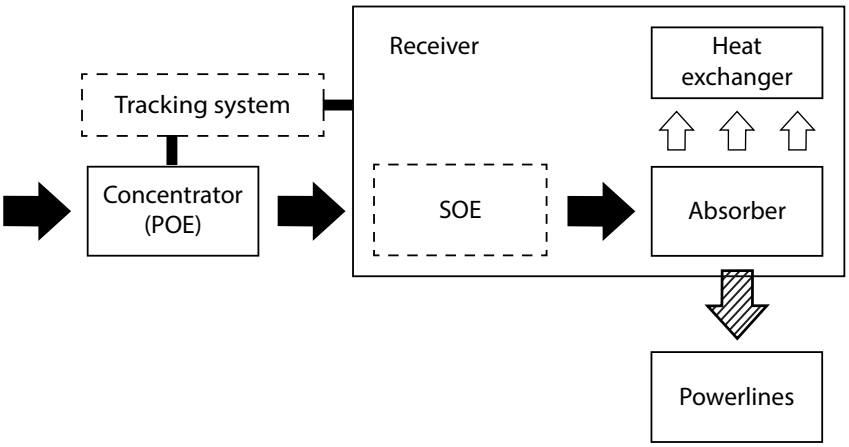


**Figure 1.6.** Schematic drawing of the component parts of a concentrating photovoltaic system. The dashed boxes represent components which are commonly used in HCPV systems but may be not be present in L- and MCPV ones. Adapted from Lovegrove *et al.* [36].

lenses whereas reflective ones can take different forms such as parabolic mirrors, hyperboloid mirrors, compound parabolic concentrators, and dielectric totally internally reflecting concentrators [37]. In general, medium- and high-concentrating POEs are not able to collect diffuse light and can only work with direct beam radiation. In this case, high-precision two-axis trackers are used to maintain the optics aligned with the Sun and to control its position with a precision of 1° or less [38].

The second element along the optical path is the receiver, *i.e.* the portion of the CPV system comprising the secondary optical element (if any), the absorber, the heat exchanger, and the electrical contacts. Secondary optical elements (SOEs) are essential for the correct functioning of HCPV modules but may not be present in L- and MCPV devices. They are placed between the concentrator and the absorber and are used to increase the acceptance angle of the receiver. According to the material they are made of, SOEs can be classified as reflective or dielectric. Devices of the first type are made of metal and work like a funnel to guide concentrated light to a centralised solar receiver. Conversely, those belonging to the second class use either refraction or total internal reflection to deviate the sunlight and concentrate it on the solar cell [39]. The most common reflective SOEs have an inverted conical or inverted truncated pyramid (ITP) shape and are obtained by bending or deep drawing sheet metal [40–42]. The same geometries can be used in diffractive SOEs with the difference that the optics are made of a dielectric material like silicone [43, 44] or glass [45]. Solid SOEs can achieve higher concentration ratios than metallic ones thanks to the fact that the material surrounding the receiver has a higher refractive index than air (as dictated by the "Radiance theorem" [46, 47]).

However, they add to the system a new index-changing interface which can cause reflection losses and thus determine a slightly lower optical efficiency [42].

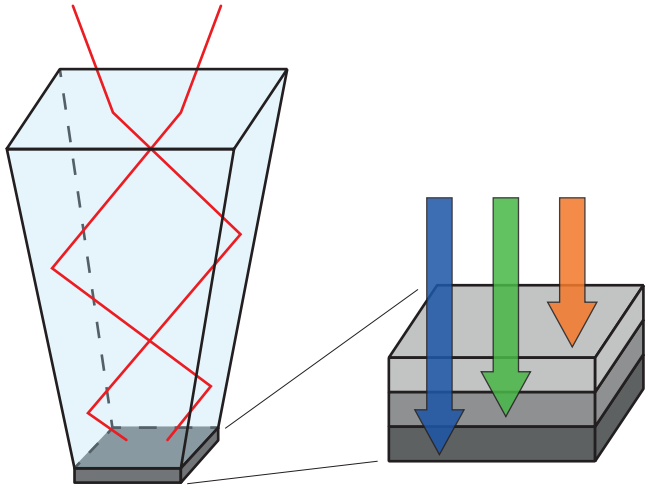

**Figure 1.7.** Main components of an HCPV system receiver: a dielectric inverted truncated pyramid (left) and a multijunction solar cell (right).

Figure 1.7 shows the schematic of an ITP (or kaleidoscope-type SOE) attached to an MJ solar cell. Due to total internal reflection, the sunlight entering the optics is reflected multiple times before reaching the exit face. This permits to reduce the aberrations induced by the primary optics and homogenise the light leaving the ITP [39]. In its simplest configuration, the absorber corresponds to a solar cell glued to the secondary optical element. The most suited cells for CPV applications are the MJ solar cells, especially if $C_g > 100\times$. These have been developed with the specific aim of overcoming the efficiency limits of traditional solar cells and reduce thermalisation losses [48]. Their structure consists of several junctions (subcells) stacked together and connected in series. Each junction is made of different II–VI, III–V, or IV–VI semiconductors and its composition is carefully studied in order to: (i) achieve the maximum conversion efficiency, (ii) generate an electric current similar to that of the other subcells, and (iii) have an absorption range complementary to those of the other subcells. In this way a wider absorption range is covered (generally from 300 to 1900 nm) and a higher power output is obtained. The portion of solar radiation not absorbed by the semiconductors is converted into thermal energy and dissipated as heat. In order to avoid overheating, the receiver is generally coupled to a heat exchanger which absorbs the excess thermal energy and transfers it to a power generator for its conversion to electric energy [49, 50]. This solution is often adopted in medium- and high-concentration PV to preserve the functionality of the solar cells and increase the total conversion efficiency of the system. In this case we talk of concentrated photovoltaic thermal (CPV-T) systems.

## Parabolic geometries

One of the most common concentrators used in CPV systems is the parabolic mirror (or dish) [11, 37, 51–53]. Its surface is defined as part of a circular paraboloid and is generated by revolving a parabola around its focal axis. Due to the geometric properties of the parabola, a plane wavefront collected through the mirror aperture is converted into a spherical wave converging toward a single point called focus. To understand how a parabolic mirror works, we can restrict ourselves to the 2D case and consider the equation of a parabola of focal length $f$ symmetrical about the $y$-axis:

$$y = \frac{x^2}{4f}. \tag{1.9}$$

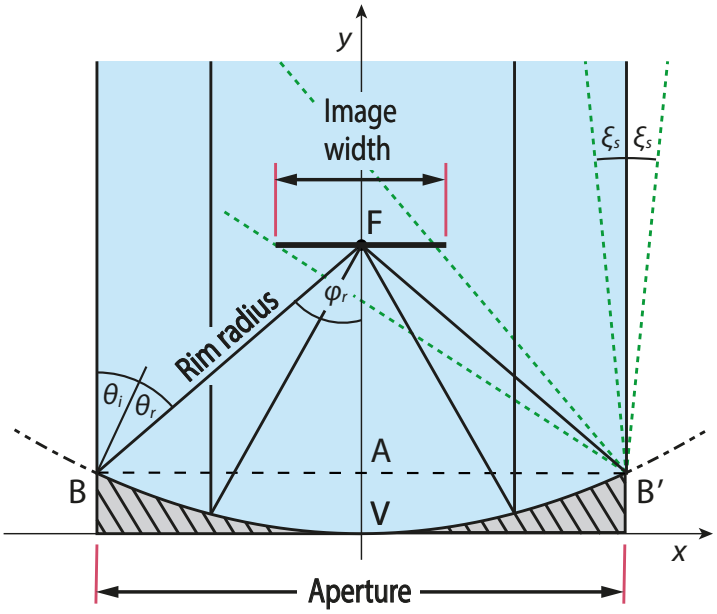


**Figure 1.8.** Cross-section of a parabolic concentrator showing the light path of a collimated (black lines) and a divergent beam (green lines) Adapted from Rabl [54].

As shown in Fig. 1.8, the vertex $V$ coincides with the origin $(0,0)$ while the focus has coordinates $F(0,f)$. When a beam of rays parallel to the $y$-axis hits the surface of the mirror, it is reflected back with an angle equal to the angle of incidence ($\theta_r = \theta_i$) forming a point-like image at the focus $F$ [36, 54–56].

For an non-collimated beam of light like that coming from the Sun, the rays entering the parabola are not concentrated at a point but rather intersect the focal plane forming a finite image of width $W$. Said $a$ the mirror aperture, $W$ is calculated as [54]:

$$W = \frac{2r_r \sin\xi_s}{\cos(\Phi_r + \xi_s)} = \frac{a \sin\xi_s}{\sin\Phi_r \cos(\Phi_r + \xi_s)}. \tag{1.10}$$

Here $\xi_s$ is the angular half-width of the Sun (4.653 mrad), $r_r$ is the rim radius of the

mirror, and $\Phi_r$ is the rim angle subtended by the edges of the reflector at the focus:

$$\Phi_r = \sin^{-1}\left(\frac{\mathrm{AB}}{\mathrm{BF}}\right) = \sin^{-1}\left(\frac{a}{2r_r}\right). \tag{1.11}$$

Equation (1.10) gives the minimal theoretical width of the focal image that would be produced by an ideal parabolic mirror. In reality, each infinitesimal surface element of the mirror reflects a distorted light cone which, intersecting the focal plane, gives rise to an elliptically shaped image. Only the light coming from the area around the vertex $V$ forms a circular image centred at $F$. The superposition of these "partial" images creates a blurred focal image whose radiosity has a maximum at thge focus and decreases radially outwards.

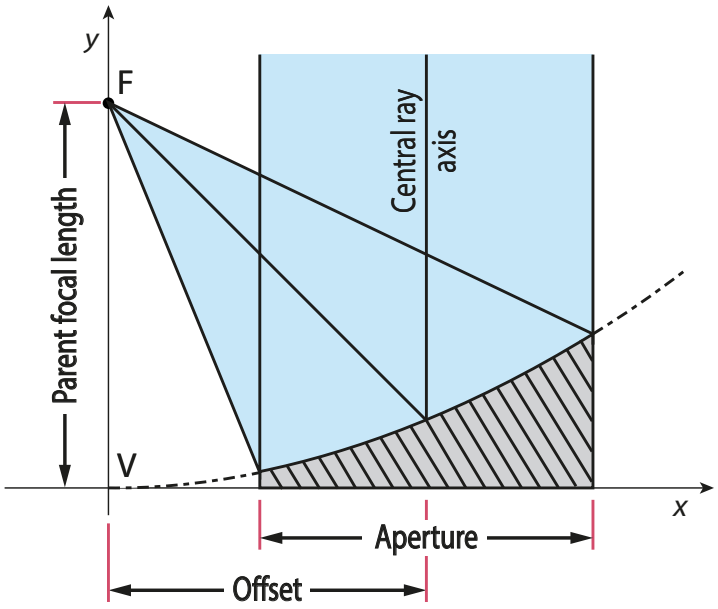


**Figure 1.9.** Cross-section of an off-axis parabolic concentrator showing the light path of a collimated beam.

Unlike standard parabolic mirrors, an off-axis parabolic (OAP) concentrator is a mirror whose reflective surface corresponds to a section of a parent parabolic mirror (Fig. 1.9). The main advantage of this geometry is that the incoming parallel rays are focused to a point $F$ forming an angle with respect to the direction of the incident light. This allows an unrestricted access to the focus and avoids the problem of central obscuration typical of parabolic dishes [57, 58]. As OAP mirrors are not rotationally symmetric, the calculation of the image width is more involved than in the preceding case. However, if the mirror offset is small, the properties of the focal image are similar to those of the parent parabolic mirror and its width can be calculated using Eq. (1.10).

A particular type of parabolic-mirror-based optics is the Cassegrain concentrator (Fig. 1.10), that is an optical design consisting of a concave primary parabolic mir-

ror and a small, convex, hyperbolic secondary mirror inside the focus of the primary one. An optional non-imaging tertiary optics can be placed at the system "prime focus" $F$ to homogenise the reflected beam and couple it to the receiver [59]. The sunlight entering the optics is first reflected by the parabolic mirror as a convergent beam on the hyperbolic mirror which, in turn, directs it through a central aperture in the primary to the focal point beyond. As the light travels along a folded optical path, the bulkiness of the assembly is greatly reduced and the system is much more compact than common Fresnel- or parabolic dish-based systems [60]. Besides the small mechanical size and the low weight, Cassegrain-like concentrators have also the advantages of eliminating spherical aberration, minimising the aperture blockage, and providing a good image contrast.

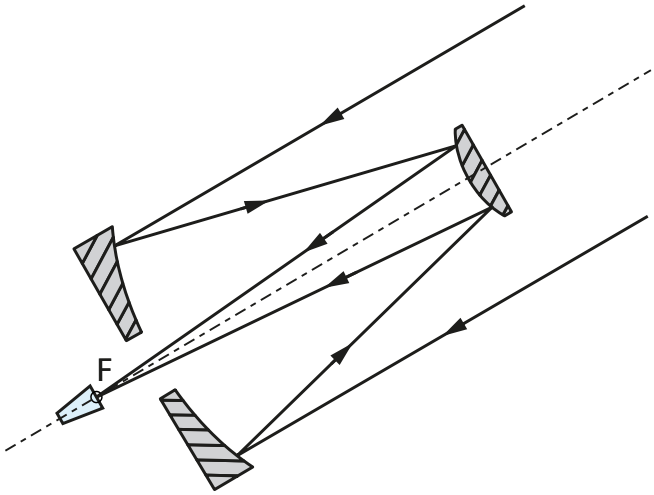


**Figure 1.10.** Cross-section of a three-stage Cassegrain concentrator showing the light path of a collimated beam.

## 1.4 Daylighting systems

Daylighting (DL) systems are devices that use sunlight to illuminate building interiors without requiring the typical light–electricity–light conversion of PV technologies. This approach has the advantage of reducing artificial light use and increasing the energy efficiency of buildings [61, 62]. According to the International Energy Agency [63], daylighting systems can be divided into two major groups: light-guiding and light-transport systems. The first group comprises devices which rely on reflection or refraction to collect natural light and redirect it to the interior of buildings. The simplest and cheapest of these devices is the light shelf, that is an horizontal element placed on a window which reflect additional sunlight into

the room as depicted in Fig. 1.11a [64, 65]. The sunlight beam is usually redirected towards the ceiling in order to avoid glare and protect the occupants from direct sunlight exposure. Light shelves and, more in general, light-guiding systems can reach a maximum depth of 8 to 10 m and can only be used in spaces where windows are already present. If the lease span exceeds 10 m or the room has no view, light-

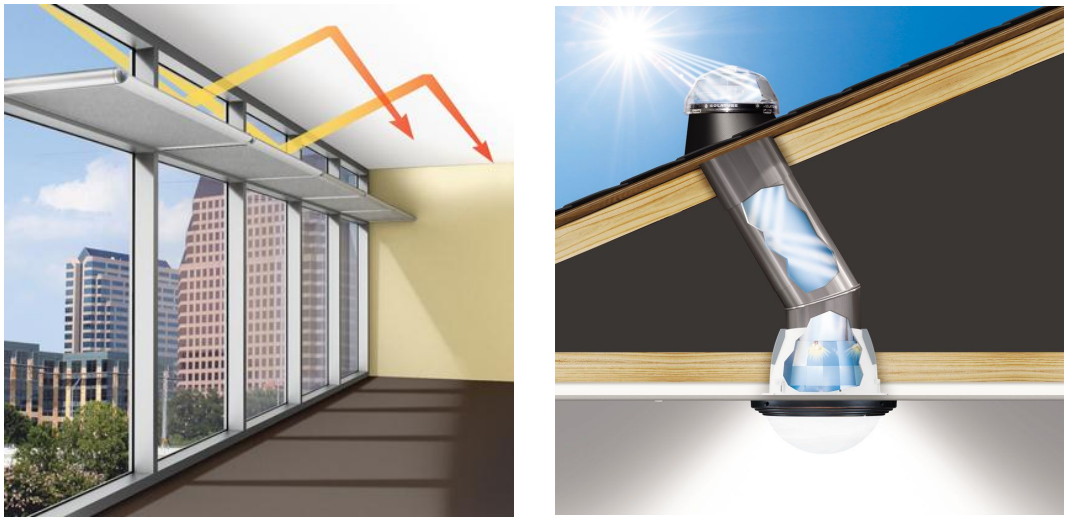

**(a)** **(b)**

**Figure 1.11.** Examples of traditional daylighting systems: (a) light shelves and (b) light pipe.

transport systems could be a better option to cover longer distances inside deep-plan buildings. The oldest and most widespread solution is to use a vertical light pipe (Fig. 1.11b) [66–70]. This system has the advantage of effectively capturing direct beam radiation while avoiding excessive heat and glare patches. It generally consists of three main parts, namely a clear dome, a tube, and one or more diffusers. The dome can be installed on a building roof or façade and has the function of collecting as much sunlight as possible. It is usually made of glass or poly(methyl methacrylate) (PMMA) and is designed in such a way as not to alter the intensity and colour quality of the transmitted light. The tube is either be metallic or dielectric (glass, acrylic plastic, or polycarbonate) and can guide the light up to 50 m. The diffusers take the form of white polycarbonate luminaries or domes and serve to project a uniform light distribution throughout the room. The system is very effective in improving room lighting but its use is limited by the reflectivity of the tube which causes a decrease in the transmitted flux as a function of the distance from the collector. These limitations were addressed in the early 1970's by the Japanese company La Foret Engineering Co., Ltd. which developed the first fibre optics daylighting system [71]. The device, called Himawari Solar Lighting System, is still available on the market and is composed of an array of tracking Fresnel lenses

coupled to quartz optical fibres (Fig. 1.12a). Each lens has a diameter of 95 mm and focuses sunlight on a fibre of 1-mm core diameter, reaching a concentration ratio of approximately 9000× [72, 73]. A more recent fibre-based system called SP4 was presented in 2004 by the Swedish company Parans Solar Lighting, AB [74] with the aim of improving light collection and transport. In this case, the collection of sunlight is performed by an array of 80 pivot-suspended Fresnel lenses coupled to high performance, 0.75-mm core diameter PMMA optical fibres (Fig. 1.12b). The concentration ratio is ∼120×, which is low enough to avoid any photoinduced damages of the plastic optical fibres. The Himawari and the SP4 systems share most of the optical design but also have the same limitations. The most important of these are the high initial cost, the long pay-back period, and the low resistance to adverse meteorological conditions [72, 73, 75]. Furthermore, the luminous flux transmitted by the two system is respectively 26,000 and 11,520 lm, which is just sufficient to illuminate an internal space of up to 50 $m^2$ [76]. This means that neither system is able to satisfy the needs of a large-scale building, nor are they enough to significantly reduce the use of electric lighting. Many other fibre optics daylighting systems have been developed in recent years, but all of them are in a prototype stage and are still under technological development [77–87].


**(a)** **(b)**

**Figure 1.12.** Examples of fibre optics daylighting systems: (a) Himawari Solar Lighting System and (b) Parans SP4 system.

## 1.5 Optical fibres for sunlight transmission

From the analysis of the latest daylighting systems, it emerges that optical fibres (OFs) offer many advantages over traditional light pipes or light-guiding modules. The most noticeable are the possibility of transmitting light over longer distances, the lower cost, and the lower signal loss.

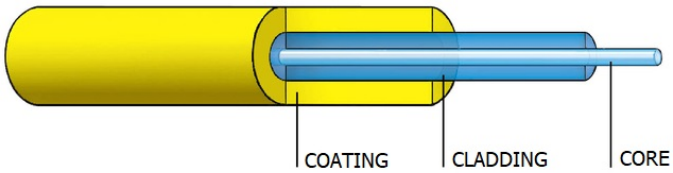


**Figure 1.13.** Structure of a typical optical fiber.

As shown in Fig. 1.13, a typical optical fibre is composed of three main components: the core, the cladding, and the coating. The core is a cylinder made of silica glass ($SiO_2$) or plastic which guides light by total internal reflection. The cladding is a sheath made up of one or more layers of dielectric material in intimate contact with the core. Its role is to confine the light and ensure the waveguide effect. The coating is a plastic or acrylate protective layer and is used to maximise the fibre strength, reduce bending losses, and increase the radius of curvature.

The basic principle underlying the propagation of light in optical fibres is the total internal reflection (TIR). This phenomenon occurs at the interface of two media with different refractive indices and determines the complete reflection of light rays within the given medium from the surrounding surface. Since the core and cladding are made of materials having slightly different refractive indices, the light injected into the core bounces from one side to the other through the whole fibre until reaching its end face. This can be observed in Fig. 1.14 where the optical path of some light rays is shown for a generic optical fibre. Starting from the left-hand side of the diagram, the rays hit the fibre front-end face and are refracted according to Snell's law:

$$n_0 \sin\theta = n_1 \sin\Phi. \tag{1.12}$$

Once inside the core, the rays travel along the fibre until they hit the core–cladding interface. If the angle $\Phi'$ formed with the normal at the point of contact is such that

$$n_1 \sin\Phi' \geq n_2, \tag{1.13}$$

the rays are reflected back and continue their way downstream towards the end of the fibre. If the incidence angle is higher than $\Phi'_c$, the rays are refracted into the

cladding and are no longer properly guided. The smallest angle at which TIR occurs is called the critical angle ($\Phi'_c$) and is given by

$$\sin \Phi'_c = \frac{n_2}{n_1}.$$

Since $\theta$, $\Phi$, and $\Phi'$ are correlated, $\Phi'_c$ determines the maximum incidence angle ($\theta_{max}$) that a ray can make with the axis of the fibre to be subject to TIR. Its value can be derived from Eq. (1.12) by imposing the limiting condition as follows:

$$\begin{aligned} n_0 \sin \theta_{max} &= n_1 \sin \Phi_c \\ &= n_1 \cos \Phi'_c \\ &= n_1 \sqrt{1 - \sin^2 \Phi'_c} \\ &= n_1 \sqrt{1 - \frac{n_2^2}{n_1^2}} \\ &= \sqrt{n_1^2 - n_2^2}. \end{aligned}$$

Since light rays usually travels in air before entering the fibre, the refractive index $n_0$ can be set to 1 and the preceding formula can be simplified to

$$\sin \theta_{max} = \sqrt{n_1^2 - n_2^2}. \tag{1.14}$$

The left-hand member of the equation is generally called the numerical aperture (NA) of the fibre and corresponds to the angle of the cone of light which can be collected by the fibre.

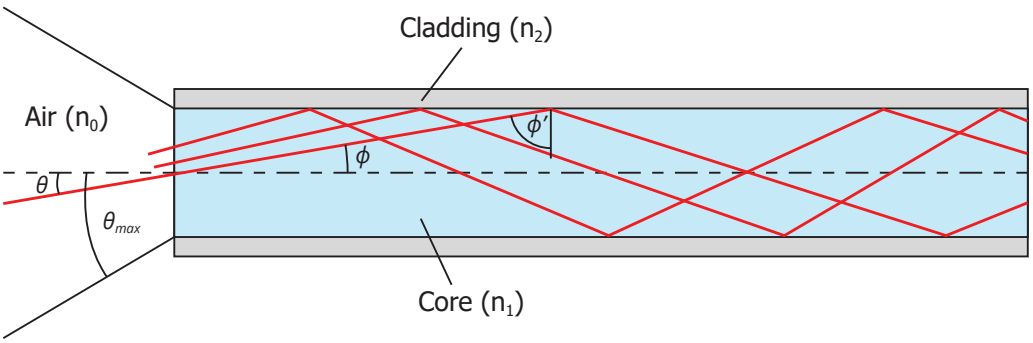


**Figure 1.14.** Ray diagram of light propagating inside an optical fibre.

As illustrated in Fig. 1.14, the light rays guided by an OF can travel along different paths inside the core. Each of these paths is called a mode and depends on both the light wavelength and the variation of the refractive index inside the dielectric medium. Fibres which carry multiple modes at a specific wavelength are called

multimode fibres (MMFs). They generally have thick core diameters, are resistant to bending, and are characterised by a relatively high attenuation. Fibres which carry only one mode are called single-mode fibres (SMFs) and are mainly used for long-range communication thanks to their cost-effectiveness, low attenuation, and low dispersion. Depending on the distribution of the refractive index across the core, MMFs can be classified as step index (SI) or graded index (GI) fibres. The former typology features a core with a uniform refraction index and are used in systems that impose no stringent requirements upon data transmission rate and are preferred when high transmission speed and low signal dispersion are required.

In order to obtain a core with $n_1 > n_2$, the materials used to make optical fibres must be accurately selected. For silica OFs, the matrix of the core is often doped with oxides such as $GeO_2$, $Al_2O_3$, or $P_2O_5$ in order to obtain a high refractive index glass. Alternatively, the cladding can be doped with $B_2O_3$ or fluorine (F) to get a glass with a lower index. The presence of impurities, however, may pose some challenges when the fibre is exposed to high-energy or concentrated light. In fact, the heteratomic centres incorporated into its network can absorb the incoming photons and transform into a stable point defect. This phenomenon is called solarisation or photodarkening and is responsible for a decrease in the fibre transmission efficiency. The same phenomenon is observed in some pure-silica fibres but its effects are generally smaller than for doped OFs.

To overcome these limitations, a special type of fibres has been developed to guarantee a loss-free transmission of UV or concentrated broadband light. These are called solarisation resistant fibres and are generally manufactured by adding gaseous reducing agents (*e.g.* $H_2$) to the silica matrix with the aim of quenching the electron-hole centres formed during irradiation and relaxing the charge-separated state which causes solarisation. There exist also models which rely on polyimide or aluminium coatings to mitigate the effects of UV degradation and enhance the transmission of light at short wavelengths and high-power densities.

The consequences of photodarkening are different in nature and range from a change in the core refractive index to the creation of absorption bands in the UV–Vis spectral domain. This latter phenomenon is generally referred to as radiation induced absorption (RIA) is the major contributor to the loss of radiant power in irradiated OFs. Its effect can be inspect by reporting the variation of the attenuation coefficient of the fibre core as a function of wavelength. In fact, from the Beer–Lambert law

$$\Phi(\lambda) = \Phi_0(\lambda)\, e^{-\alpha(\lambda) l} \tag{1.15}$$

we know that the radiant flux leaving ($\Phi$) leaving an OF depends on the injected flux ($\Phi_0$), the attenuation coefficient of the core medium ($\alpha$), and the length of the

fibre ($l$). By deriving $\alpha$ from the preceding equation we have:

$$\alpha(\lambda) = -\frac{1}{l} \ln \frac{\Phi(\lambda)}{\Phi_0(\lambda)} \tag{1.16}$$

which, expressed in $\mathrm{dB} \cdot \mathrm{m}^{-1}$, reads:

$$\alpha(\lambda) = -\frac{10}{l} \log \frac{\Phi(\lambda)}{\Phi_0(\lambda)}. \tag{1.17}$$

Figure 1.15 shows a series of RIA spectra measured for a $P_2O_5$-doped multimode fibre. Since the damages caused by the transmitted radiation are dose-dependent, the RIA function (*i.e.* the coefficient $\alpha$) is a function of both time and wavelength. Each RIA profile is given by the convolution of the absorption bands created during the light exposure, and its value rises with time as the number of photo-generated point defects increases. The accumulation of defects in the $SiO_2$ matrix is a very important aspect for fibres used in concentration solar applications since its effects may not be visible on new devices but may comport a gradual decrease in the efficiency of CPV systems as these are continuously exposed to concentrated sunlight.

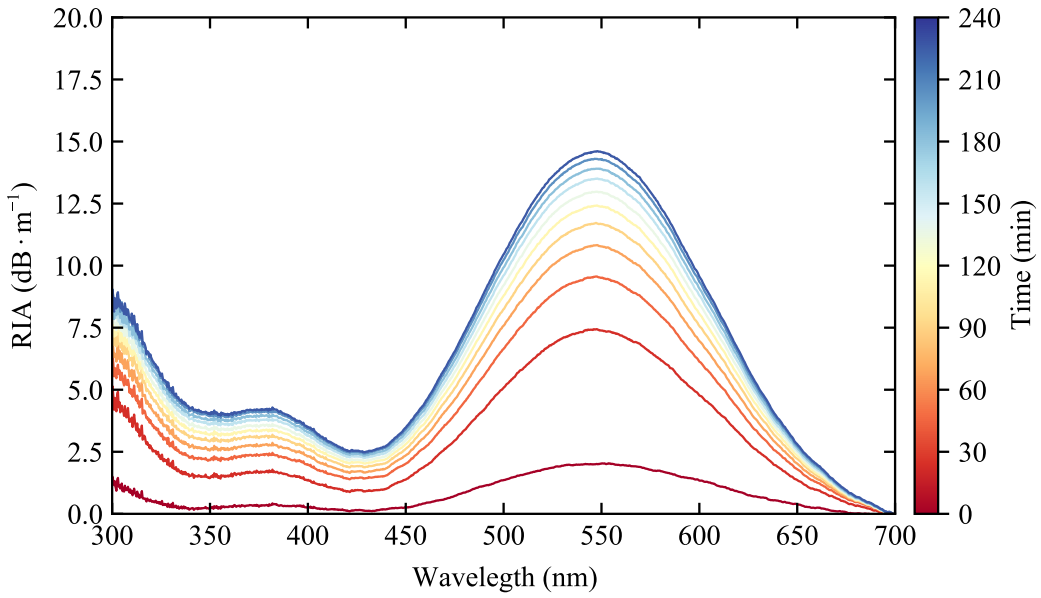


**Figure 1.15.** A typical experimental RIA spectrum of a P-doped optical fibre.

## 1.6 Hybrid systems and future perspectives

Thanks to the improvement in optical fibre performance and the continuous reduction of the manufacturing costs, the future of daylighting is likely directed towards

the development of more efficient OF-based systems. Besides being less expensive and easier to install, these systems will offer the opportunity of simultaneously minimise the amount of artificial light and generate photovoltaic power for on-site use. The idea of a hybrid daylighting/photovoltaic (DL/PV) device has emerged only in recent years and very few studies have been dedicated to this topic. One of the first model was developed by Antón *et al.* in 2007 [88] using a Cassegrain parabolic–hyperbolic concentrator coupled to a three-piece receiver. The first component of the receiver is a 40-cm cylindrical quartz rod which receives the concentrated sunlight and homogenises it by a kaleidoscope effect. The light leaving the rod is directly injected into a bundle of solarisation resistant optical fibres. It was realised by fusing together 144 multimode, pure silica-core, plastic-cladding OFs of diameter 1.8 mm each. At the bundle far end, the fibres are coupled to 144 dual-junction solar cells mounted on a plate located indoors. Despite the complexity of the system and the high concentration ratio reported by the authors (1024×), the fibre excitance has an uneven spatial distribution due to a non-uniform illumination at the rod output. This causes a significant electrical mismatch on the MJ cells and their conversion performance result compromised. The problem was discovered to be related to the presence of microbubbles or opaque regions in the silica matrix of the rod. The field test of the prototype revealed that the maximum achievable efficiency was of 18%.

More recently the same research group presented a new hybrid lighting–CPV module working at a concentration ratio of 476× [89, 90]. In this case, the module concentrator is formed by a tracking parquet of silicon-on-glass lenses subdivided into two different sets. The first set comprises twenty-four $120 \times 120\,\mathrm{mm}^2$ lenses focusing the sunlight on a series of underlying InGaP–InGaAs–Ge solar cells. The second set of lenses consists of the fifteen lenses of $35 \times 35$-$\mathrm{mm}^2$ area placed at the corners of the other lenses and used to inject sunlight into PMMA-core, fluorinated-polymer-cladding, 3-mm diameter OFs. The module proved to be able to simultaneously produce a maximum power of 85 W and an luminous flux of 467 lm.

Despite being just prototypes, the hybrid systems developed by Antón *et al.* are a proof that photovoltaic and daylighting technologies are compatible with each other and their integration into a single module represents an enormous advantage in terms of space requirements and overall cost. To reach the goal of zero-energy buildings, however, many open issues should be addressed for the design of a successful hybrid system. The most important is the power and luminous output. From a survey of the existing technology, it is clear that low-concentration devices are not able to fully support the electrical and illumination need of buildings. For this reason, the future development of hybrid systems should be directed towards higher concentration ratios and thus higher electrical and optical efficiencies. However, increasing the injected flux may lead to a quicker degradation (solarisation) of the

opotical components of the system, expecially the waveguides used to collect the sunlight. The development of DL/HCPV modules should hence be accompanied by a thorough study of the materials suitable to withstand highly concentrated light. Last but not least, the design of a hybrid system should not neglect that its market price should be competitive with other well-established technologies and for this reason the use of highly specialised optics or materials should be kept at minimum due to their general high costs.

# Chapter 2

# Structural and optical properties of silica

## 2.1 Amorphous silica and its polymorphs

$SiO_2$ is the chemical formula of a group of minerals constituting about 95% of Eart's rocks and soils [91, 92]. The most stable polymorph is $\alpha$-quartz, which has a trigonal crystal structure and exists in both a right-handed and a left-handed form. When heated to 573 °C at atmospheric pressure, $\alpha$-quartz transforms into $\beta$-quartz and assumes a hexagonal crystal structure [93, 94]. By further increasing temperature, $\beta$-quartz turns into HP-tridymite (870 °C) and then into $\beta$-cristobalite (1470 °C). At 1713 °C the latter melts into fused silica, which is a homogenous and isotropic amorphous material characterised by a highly randomised structure. Since phase transitions are reversible, a slow cooling of the melt leads to the solidification into $\beta$-cristobalite and then backwards through all the polymorphs down to $\alpha$-quartz. Nonetheless, if the temperature drop is rapid, the system freezes in a metastable state and eventually relaxes to amorphous silica ($a$-$SiO_2$). This non-crystalline polymorph is characterised by a disordered network lacking long-range order and by the presence of low density regions.

The building block of all silica polymorphs is the $[SiO_4]^0$ tetrahedron, that is the structural unit formed by a silicon and four oxygen atoms bonded by mixed covalent/ionic bonds (the superscript zero indicates that the unit is electrically neutral). The covalent character of the bond is determined by the overlap of the Si($sp^3$) and O($2p$) orbitals while its ionic character is given by the Si($3d$)–O($2p$) $\pi$-interactions.

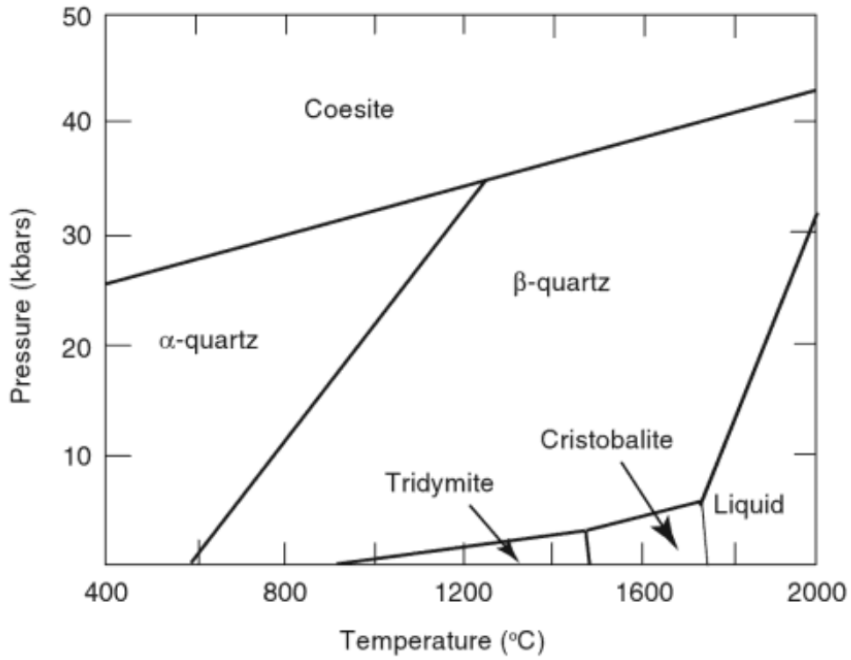


**Figure 2.1.** Phase diagram of $SiO_2$.

This last contribution is also responsible for the short Si–O bond length ($d_{Si–O} = 1.605\,Å$), the increased Si–O–Si angle ($\varphi = 109.47°$), and the variability of the intertetrahedral angles [95–97].

The three-dimensional structure of silica consists of a continuous random network of corner-sharing tetrahedra whose relative position is determined by the Si–O–Si bond angle ($\theta$) and the Si–O–Si–O and O–Si–O–Si torsion angles ($\omega_1$ and $\omega_2$). Many experimental works have attempted to estimate $\theta$ but the reported values greatly vary from reference to reference. The reason for this uncertainty is that the angle is correlated with the Si–O and Si–Si distances and its value cannot be determined from experimental data without making some starting assumptions [98–103]. Taking into account the data reported in the literature and the outcomes of their own simulations, Yuan and Cormack proposed a distribution of Si–O–Si angles with a mean value of 147° and a standard deviation of 10°–13° [104]. This estimation was supported by Carpentier *et al.* who derived a mean value of $147° \pm 11°$ by combining molecular dynamics with first-principles calculations of NMR parameters [99]. In a recent review, Malfait *et al.* proposed the value collected a large set of data and located the most probable Si–O–Si angle at $149° \pm 7°$ [105].

Since the publication of Wright's paper [106], the spacial arrangement of the $SiO_4$ units has always been discussed in terms of the torsion angles $\omega_1$ and $\omega_2$. Using the notation given in Fig. 2.2, these two angles are defined as the dihedrals $O_{(1,2,3)}$–$Si_1$–$O_4$–$Si_2$ and $Si_1$–$O_4$–$Si_2$–$O_{(5,6,7)}$, respectively. From a geometrical point of view, the existence of two independent torsion angles is justified only if a conventional order can be assigned to the structure of silica (as in the case of proteins' primary

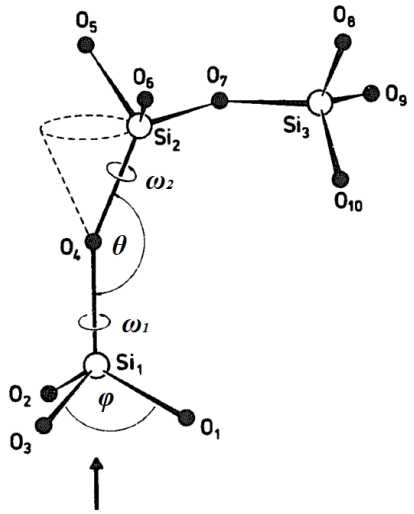


**Figure 2.2.** Definition of the Si–O–Si bond angle $\beta$ and the torsion angles $\omega_1$ and $\omega_2$. Adapted from Write [106].

structure). Since silica network is intrinsically non-oriented, $\omega_1$ and $\omega_2$ are equivalent and carry the same information. For this reason we will only consider the Si–O–Si–O angle which we will call $\omega$. From the data reported in the literature [104, 107], it results that $\omega$ is a continuous function of the Si–O–Si bond angle with maxima around 60°, 180°, and 300°. When two tetrahedra are such that $\omega$ is equal to one of these values, the $O_3Si$–O–$SiO_3$ moiety assumes a staggered conformation (as viewed along the Si-Si axis) and the next-nearest-neighbour oxygen atoms are at the maximum distance from each other.

The analysis of the network topology of silica was first addressed by King who proposed the shortest-path criterion to identify closed paths of alternating Si–O bonds [108]. According to this criterion, a ring is defined as the shortest closed path connecting two oxygen atoms bonded to the same Si atom. If the path is formed by $n$ bonds (or equivalently by $2n$ atoms) the ring is called an $n$-membered ring ($n$-MR) [109, 110]. By applying King's algorithm to $\alpha$-quartz and $\beta$-cristobalite, we find that both polymorphs are composed of regular six-membered rings arranged to form different three-dimensional structures [111]. The former network is made up of interconnected hexagonal and trigonal helices of $SiO_4$ tetrahedra whereas the latter consists of stacked layers of tetrahedra with the individual units alternately pointing up and down [112]. In the case of amorphous silica, the topological analysis results in a broader ring-size distribution and a quasi-random orientation of the tetrahedral units. The most abundant topological structure are six-membered rings, followed by five- and seven-membered ones. The concentration of 3- and 4-MRs is often low but not zero due to the existence of strained Si–O–Si bond which allow the formation of out-of-equilibrium structures [98]. In fact, for regular planar three-membered rings, $\theta$ takes the value of 130.5° whereas for regular planar four-

membered rings its value is 160.5°. In both cases $\theta$ is far from its energetically optimal value (144°–155°) and for this reason small-sized rings tend to release the excess energy by breaking a strained bond and turn into bigger ones [113, 114].

## 2.2 Point defects in silica glasses

While in bulk silica the concentration of three- and four-membered rings is relatively low, silica optical fibres exhibit an increased concentration of small rings caused by the residual stress generated during the manufacturing process [115]. This is due to the rapid cooling of melt silica which results in a more disordered glass structure with a higher concentration of strained Si–O–Si angles. This explains the sensibility of OF to radiation and their higher concentration of point defects [116, 117].

### *E′* centres

The most known defects in crystalline and amorphous $SiO_2$ are the $E'$ centres. As demonstrated by Hosono *et al.* [118], these defects originate from the opening of small-sized rings after exposure to $F_2$-excimer laser light (7.9 eV, 157 nm) as shown in the following reaction:

$$\underset{[SiO_4]^0}{\equiv Si-O-Si\equiv} \longrightarrow \underset{STE}{[\equiv Si^{-}\text{---}{}^{+}O-Si\equiv]^{*}} \longrightarrow \underset{E'}{\equiv Si^{\bullet}} \quad \underset{NBOHC}{{}^{\bullet}O-Si\equiv}. \tag{2.1}$$

The three dashes here represent three different Si–O bonds, the asterisk marks an electronically excited state, and the dot stands for an unpaired electron. The first step of the reaction involves the transition of an electron from the valence to the conduction band and the formation of a self-trapped exciton (STE) consisting in an excited electron ($e^-$) located on a silicon atom and a hole ($h^+$) trapped at one or more neighbouring oxygen atoms [119, 120]. This structure is kept metastable by the spontaneous creation of a localised distortion in the $SiO_2$ network which lowers the total energy of the system and traps the $e^- - h^+$ pair at the distortion site [121]. Shluger theoretically proposed a model in which the exciton self-trapping is accompanied by the weakening of a Si–O bond and the subsequent displacement (0.3 Å) of the oxygen atom towards an interstitial position [122]. Other calculations showed that, after the electronic excitation, the system relaxes to the nearest energy minimum on the excited-state energy surface by breaking a Si–O bond and moving the Si atom into a planar geometry [120, 121]. In this case, the STE features a hole located at the non-bridging oxygen orbital $O_{NB}(2p)$ and an electron localised on the non-bonding $2p$ orbital of the $sp^2$-hybridised Si atom. The hole trapped at the singly coordinated oxygen atom is the candidate for the generation of a stable

defect called non-bridging oxygen hole centre (NBOHC) [123]. Likewise, the three-fold coordinated Si atom is the precursor of the point defect called $E'_\alpha$ centre. The decay of the STE causes the $sp^2$-to-$sp^3$ rehybridisation of the silicon atom and the stabilisation of the pair of point defects. This model was further refined by Donadio and Bernasconi who computationally demonstrated that the defect pair is metastable on the triplet ($T_1$) excited state but spontaneously recombines upon de-excitation to the ground state ($S_0$) due to a charge transfer from the $E'_\alpha$ to the NBOHC [124]. However, by allowing NBOHC to migrate, the system reaches a configuration in which the two defects are 6.3 Å apart and cannot recombine anymore. In this new minimal-energy state, no interaction is possible and the properties of the two defects are virtually equal to those of the isolated centres.

A second pathway for $E'$ centre formation was proved by Tsai and Griscom while studying the effect of ArF excimer laser light (6.4 eV, 193 nm) on silica specimens [125]. The first step of the proposed mechanism consists in the formation of a self-trapped exciton that later evolves as follows:

$$\underset{[SiO_4]^0}{\equiv Si-O-Si\equiv} \longrightarrow \underset{STE}{[\equiv Si^{-}\text{---}{}^{+}O-Si\equiv]^{*}} \longrightarrow \underset{ODC}{\equiv Si-Si\equiv} + O^0. \tag{2.2}$$

Contrarily to reaction (2.1), the non-radiative decay of the STE here leads to the displacement of the oxygen atom and the consequent formation of a stable Frenkel defect pair made of an interstitial $O^0$ atom and a $\equiv Si-Si\equiv$ oxygen vacancy [126]. This can be further excited by a second photon to produce a defect called $E'_\gamma$ centre and a nearly planar $\equiv Si^+$ unit [127, 128]:

$$\underset{ODC}{\equiv Si-Si\equiv} \longrightarrow \underset{E'}{\equiv Si^{\bullet}} \quad {}^{+}Si\equiv + e^{-}. \tag{2.3}$$

Although the major channel for the formation of $E'$ centres has not yet been identified, it appears that the bond-dissociation mechanism (2.1) prevawhereas the Frenkel-type mechanism in (2.2) and (2.3) predominates at lower energies. This view is supported by experimental results showing that the concentration of $E'_\alpha$ and NBOHC defects increases linearly with the pulse energy of $F_2$ lasers (7.9 eV) [118], while that of $E'_\gamma$ centres and $O^0$ increases quadratically with the pulse energy of KrF (5.0 eV) and ArF lasers (6.4 eV) [129, 130]. As a consequence, it has been suggested that the rupture of the Si–O bond in reaction (2.1) is assisted by the absorption of a single photon [131], while the cleavage of the O atom is induced by a two-photon process [125]. Since the photons can be absorbed together or at different times, two different pathways have been proposed for this reaction. If the absorption is not simultaneous, the first photon is responsible for the formation of the STE whereas the second serves to ionise the oxygen vacancy and produce the Si dangling bond [132]. These two steps correspond to reactions (2.2) and (2.3) and each of them is activated by a one-photon absorption. On the other hand, if the two photons are

absorbed at the same time, the reaction goes through a biexciton process in which one of the two STEs decays first and the other supplies the hole that produces the $E'_\gamma$ centre by combining with the ≡Si−Si≡ vacancy [133]. In this case, the reaction (2.3) is better expressed as:

$$\equiv\mathrm{Si}-\mathrm{Si}\equiv + h^+ \longrightarrow \equiv\mathrm{Si}^\bullet \quad {}^+\mathrm{Si}\equiv. \tag{2.4}$$

The centres $E'_\alpha$ and $E'_\gamma$ have different chemical environments but are characterised by the same electronic structure consisting of an unpaired electron localised in an $sp^3$ orbital of an electrically neutral, three-fold coordinated Si atom [134]. The band associated to both defects (Fig. 2.3) is peaked at 5.8 eV (214 nm) with a full width at half maximum (FWHM) of 0.8 eV and an oscillator strength $f = 0.14 \pm 0.01$ [135]. The electronic transition corresponding to this band is still debated but it has been suggested that the OA originates from the charge transfer occurring from valence band states (that is, from the $2p$ orbital of one of the three O atoms bonded to the E′ centre) to the empty state of the Si dangling bond [136]. This is supported by density functional theory calculations showing that the lower part of the absorption spectrum of $a$-$SiO_2$ is given by the superposition of the latter $\mathrm{O}(2p) \longrightarrow \mathrm{Si}(sp^3)$ transition and that from the occupied $\mathrm{Si}(sp^3)$ state to the conduction band [137].

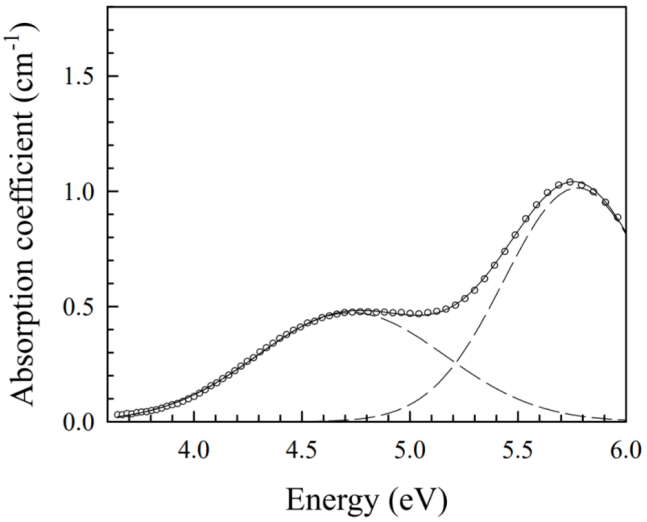


**Figure 2.3.** Optical absorption spectrum of a synthetic silica sample showing two bands assigned to the E′ centre (5.8 eV) and the NBOHC (4.8 eV). Adapted from Cannas *et al.* [138].

A third type of $E'$ defect called $E'_\beta$ is rarely found in amorphous silica and for this reason its atomic structure remains controversial [139]. The commonly accepted model features a $\equiv\mathrm{Si}^\bullet$ moiety coupled with a hydrogen-saturated oxygen vacancy generated as follows [140–142]:

$$\equiv\mathrm{Si}-\mathrm{OH} \longrightarrow \equiv\mathrm{Si}-\mathrm{O}^{\bullet} + \mathrm{H}^{0} \tag{2.5}$$

$$\equiv\mathrm{Si}-\mathrm{Si}\equiv + \mathrm{H}^{0} \longrightarrow \equiv\mathrm{Si}^{\bullet} \quad \mathrm{H}-\mathrm{Si}\equiv. \tag{2.6}$$

These coupled reactions are generally observed in hydrogen-rich silica where the concentration of silanol groups (Si–OH) is high. The first step of the mechanism consists in the breaking of the O–H bond caused by irradiation with $F_2$ lasers or ionising beams. In the second step, the free hydrogen atom ($H^0$) reacts with a precursor already present in the silica network to generate an $E'_\beta$ centre and a neighbouring $\equiv$Si$-$H moiety.

## Non-bridging oxygen hole centre

The non-bridging oxygen hole centre (NBOHC) is the simplest oxygen-related intrinsic defect in silica. It corresponds to a Si atom bonded to an O atom having a dangling bond, that is an unpaired electron in a $2p$-like non-bonding orbital [123]. As seen above, there exists two major pathways through which NBOHCs can be created. The first is called the intrinsic mechanisms and consists in the photolysis of a strained Si–O–Si bond as given in reaction (2.1). The second is the extrinsic mechanism and corresponds to the homolytic cleavage of a silanol bond as shown in reaction (2.5). The predominance of a mechanism over the other is determined by the energy of the excitation beam as well as the nature and concentration of preexisting defects [143].

The electronic structure of NBOHCs was fully described by Suzuki *et al.* using *ab initio* cluster calculations [144]. The proposed energy level diagram is illustrated in Fig. 2.4a. A part from the bonding and antibonding $\sigma$ orbitals, the diagram shows a series of non-bonding orbitals whose degeneracy is lifted by the interaction of the defect with the surrounding atoms. In particular, the non-bonding orbitals of the bridging oxygens are split into two sets of multiply-degenerate $n_{p_x}(\mathrm{O_B})$ and $n_{p_z}(\mathrm{O_B})$ orbitals whereas the lone-pair orbitals of the non-bridging oxygen separates into two $n_{p_x}(\mathrm{O_{NB}})$ and $n_{p_y}(\mathrm{O_{NB}})$ levels. The highest occupied molecular orbital (HOMO) is the singly-occupied $n_{p_y}(\mathrm{O_{NB}})$ orbital whereas the lowest unoccupied molecular orbital (LUMO) coincides with the antibonding $\sigma^*_{p_z}(\mathrm{Si\text{-}O_{NB}})$ orbital. The promotion of electrons from the lower levels to the HOMO gives rise to three OA bands corresponding to three distinct electronic transitions [145, 146]:

(i) An asymmetric Pekarian-shaped band peaked at 1.97 eV (FWHM $= 0.17$ eV, $f \approx 1.5 \times 10^{-4}$ eV) attributed to the $\sigma_{p_z}(\mathrm{Si\text{-}O_{NB}}) \longrightarrow n_{p_y}(\mathrm{O_{NB}})$ transition from the bonding $\sigma$ orbital to the HOMO.

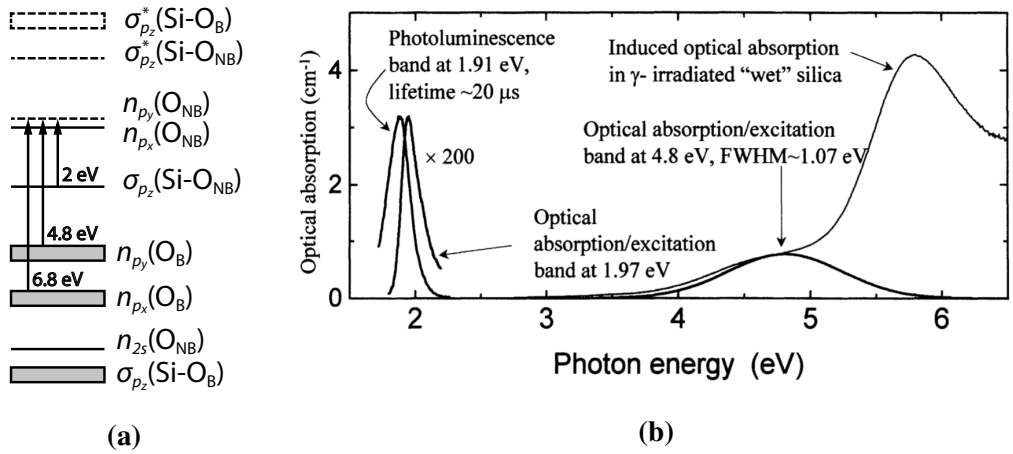


**Figure 2.4.** (a) Energy level diagrams of a non-bridging oxygen hole centre. The arrows correspond to optical transitions while the boxes indicate multiply degenerated levels. Adapted from Suzuki *et al.* [144]. (b) Optical absorption and photoluminescence spectra of $\gamma$-irradiated wet silica illustrating the main optical properties of NBOHC. Reproduced from Skuja [135].

(ii) A band centred at 4.8 eV (FWHM = 1.07 eV, $f \approx 0.05$) originating from the $n_{p_x}(\mathrm{O_B}) \longrightarrow n_{p_y}(\mathrm{O_{NB}})$ transition between the bridging-oxygen lone-pair orbital perpendicular to the Si–O–Si plane and the HOMO.

(iii) A band at 6.8 eV (FWHM $\approx$ 1.8 eV, $f = 0.05$) related to the $n_{p_x}(\mathrm{O_B}) \longrightarrow n_{p_y}(\mathrm{O_{NB}})$ transition from the bridging-oxygen lone-pair orbital lying in the Si–O–Si plane to the HOMO.

The decay of the excited state created by the above transitions gives rise to a photoluminescence (PL) band at 1.91 eV with an FWHM = 0.17 eV and a lifetime of $\sim$20 μs [135, 147]. It could be expected that the excitation from the $\sigma$ orbital to the HOMO imply a weakening of the Si$-$O$^\bullet$ bond and a lengthening of the mean bond distance. However, experimental results indicate that the frequencies of the Si$-$O$^\bullet$ symmetric stretching mode in the ground (890 cm$^{-1}$) and in the excited state (860 cm$^{-1}$) are almost the same and the Stokes shift between the excitation and emission bands is as small as 0.06 eV [148–150]. This anomalous behaviour is caused by the interaction of the doubly-occupied $n_{p_y}(\mathrm{O_{NB}})$ orbital in the excited state with a symmetry-adapted combination of the three empty $\sigma^*_{p_y}$(Si-O$_B$) orbitals [144]. This so-called "negative hyperconjugation" is responsible for the partial delocalisation of the electron density from the oxygen to the silicon atom and the resulting stabilisation of the $\sigma_{p_z}$(Si-O$_{NB}$) MO in the electronically excited NBOHC. In this way it is possible to explain the small electron-phonon coupling and the almost unvaried Si$-$O$^\bullet$ bond length in the ground and the excited state.

## Oxygen-deficiency centres

Oxygen-deficient centres (ODCs) are the simplest type of neutral oxygen monovacancies and are generally observed in the form of Si–Si dimers [151]. They are naturally present in unirradiated silica but their concentration rises considerably when a glass is irradiated with UV, X-ray, or $\gamma$-ray beams [135]. The major formation pathway of ODCs is that given in reaction (2.2) where a photon causes the release of an interstitial oxygen atom from the silica network, leaving behind two undercoordinated Si atoms.

The first spectroscopic studies on ODCs were performed in the mid-1950s by Garino-Canina [152], Mitchell and Paige [153], and Cohen [154], among others. Their results led to the identification of two optical absorption bands called "E-band" (7.6 eV) and "$B_2$-band" (5.0 eV) tentatively assigned to interstitial oxygen atoms and divalent silicon atoms, respectively. In addition, three photoluminescence bands ($\alpha$, $\beta$, and $\gamma$) were observed at approximately 4.3 eV, 3.1 eV, and 2.7 eV, and associated with substitutional Ge atoms at oxygen-vacancy sites. In 1983, O'Reilly and Robertson [155] calculated the electronic structure of the main defects of $SiO_2$ and suggested two different variants for the oxygen-deficient centre. The so-called OCD(I) was though to correspond to a relaxed $\equiv$Si$-$Si$\equiv$ oxygen vacancy while OCD(II) was identified with an unrelaxed $\equiv$Si$\cdots$Si$\equiv$ bond of length 3.06 Å. This picture was partially confirmed by Hosono *et al.* [156] and Imagawa *et al.* [157]who found that, by heating unirradiated $SiO_2$ glasses in either hydrogen or oxygen gas flow, the intensity of the E-band decreased as a function of time. To rationalise this result, they proposed the following reactions in which preexisting ODCs are neutralised by $H_2$ and $O_2$:

$$\equiv\text{Si}-\text{Si}\equiv + \text{H}_2 \longrightarrow \equiv\text{Si}-\text{H} \quad \text{H}-\text{Si}\equiv \tag{2.7}$$

$$\equiv\text{Si}-\text{Si}\equiv + \frac{1}{2}\,\text{O}_2 \longrightarrow \equiv\text{Si}-\text{O}-\text{Si}\equiv. \tag{2.8}$$

This model provided the definitive proof of ODC(I)'s structure and optical activity but did not clarified the nature of the other defect variant. As experimental evidences built up, two alternative structural models were put forth to explain the spectroscopic behaviour of ODC(II). One is the neutral oxygen vacancy ($V_{\text{O}}^0$) model originally proposed in Ref. [155] and subsequently adopted by Imai *et al.* [132, 158] to interpret the effect of ArF and KrF excimer-laser irradiation on dehydrated oxygen-deficient silica. In particular, they observed that the intensity of both the $B_2$-band and the PL $\alpha$-band decreased in a non-linear fashion while the E-band remained at its original intensity level. The analysis of defect concentration vs irradiation time also revealed that $E'$ centres were generated in a dose-dependent manner and that the growth curve could be decomposed into an initial, saturating

part due to ODC(II) and a larger, linear-growth component attributable to ODC(I). The formation mechanism of $E'$ centres was thus proposed to proceed via direct photoionisation of ODCs or hole-trapping as given in reactions (2.3) and (2.4).

The second model, called the twofold-coordinated silicon ($Si_2^0$) model, was proposed by Skuja to interpret the origin of the OA band at 5.03 eV and the PL bands at 4.3 and 2.7 eV [159]. The structure proposed for the ODC(II) was that of a electrically neutral (hence the superscript 0) divalent Si atom bonded to two bridging O atoms (subscript 2) and having a lone pair in an $sp^2$ orbital. The transition giving rise to the $B_2$-band was identified with the $S_0 \longrightarrow S_1$ excitation of the twofold Si atom while those associated with the $\alpha$- and $\gamma$-bands were the transitions $S_1 \longrightarrow S_0$ and $T_1 \longrightarrow S_0$. This model was supported by the studies of Tsai and Griscom [160] which demonstrated that the electron paramagnetic resonance (EPR) properties of ODC(II) were compatible with an $sp^3$ silicon atom bonded to two oxygen and one hydrogen atom. To explain the formation mechanism of the defect, the authors resumed the pathway described by Radtsig [161] which consists in the following two reactions:

$$\equiv\mathrm{Si}-\mathrm{O}^{\bullet} + \mathrm{H}_2 \longrightarrow \equiv\mathrm{Si}-\mathrm{OH} + \mathrm{H}^{\bullet} \tag{2.9}$$

$$=\mathrm{Si}\!:\, + \mathrm{H}^{\bullet} \longrightarrow =\mathrm{Si}^{\bullet}-\mathrm{H}. \tag{2.10}$$

In the first step an NBOHC recombines with an $H_2$ molecule to give a silanol group and a free hydrogen atom. In the second step, the latter reacts with an ODC(II) and converts it into a special variant of $E'$ centre called H(I) centre. Both reactions have been confirmed in a number of experimental and theoretical studies and represent the cornerstone of the $Si_2^0$ model [162–165].

In 1989, the ODC(II) issue got even more complicated when Tohmon *et al.* reported the existence of two accidentally overlapping bands making up the $B_2$-band [166]. The first contribution (called $B_{2\alpha}$) was centred at 5.02 eV (FWHM = 0.35 eV) and was related to two emission bands at 4.42 and 2.7 eV. The other band ($B_{2\beta}$) was peaked at 5.15 eV (FWHM = 0.48 eV) and was linked to the emission at 4.24 eV and 3.16 eV. By analysing the decay lifetime of the photoluminescence (PL), the authors proposed that the $B_{2\alpha}$-band corresponds to the singlet-to-triplet ($S_0 \longrightarrow T_1$) transition of the relaxed $\equiv$Si$-$Si$\equiv$ bond while the corresponding luminescence is due to the inverse transition $T_1 \longrightarrow S_0$. The origin of the $B_{2\beta}$-band was not discussed by the authors but it was subsequently attributed by Kohketsu *et al.* [167] to the $=$Si$\!:$ centre, together with the corresponding 4.24- and 3.16-eV PL bands. Theses assignments were largely criticised mainly because the $B_{2\alpha}$-band lifetime ($\tau \approx 100\,\mu$s) did not match the value of 10 ns reported in many other studies [168–170]. Moreover, Anedda *et al.* observed that the 4.4-eV emission band was due to an intrinsic defect and that it shifted to 4.2 eV when the defect was perturbed by an

unidentified impurity [171]. The two PL bands were thus called $\alpha_I$ and $\alpha_E$, where $I$ stands for intrinsic and $E$ for extrinsic. On the basis of these observations, Skuja reelaborated the $Si_2^0$ model including the possibility for Ge and Sn to form ODC-like defects which could contribute to the optical properties of low-purity and Ge-doped $SiO_2$ glasses. According to this new $T_2^0$ model (with $T$ standing for Si, Ge, or Sn), the divalent =Si: centre is responsible for the OA band peaked at 5.02 eV ($S_0 \longrightarrow S_1$ transition) [170, 172], as well as for the PL $\alpha_I$ ($S_1 \longrightarrow S_0$) and $\beta$ ($T_1 \longrightarrow S_0$) bands [159, 173]. Similarly, the isoelectronic =Ge: defect gives rise to the 5.15-eV OA band and the two PL bands $\alpha_E$ and $\gamma$ (transitions as before). This model has gained a wide acceptance in recent years and is backed up by both theoretical [174–177] and experimental [178–180] investigations.

## 2.3 Extrinsic defects

As described in the $T_2^0$ model, the introduction of dopant species in the $SiO_2$ network produces additional electronic levels which can favour the formation of new intrinsic and extrinsic defects [181]. Standard dopants of silica glasses include germanium ($GeO_2$), aluminium ($Al_2O_3$), phosphorus ($P_2O_5$), and fluorine ($SiF_4$). Each of these species can form a wide number of extrinsic defects which absorb radiation from the UV to the IR domain. In the following sections we will only focus on the colour centres having OA bands in the UV–Vis domain, as this is the spectral range of major interest for solar applications. For a more detailed discussion see the review [182] and references therein.

### Germanium-related point defects

It is well known that the incorporation of germanium into amorphous silica induces the formation of different point defects absorbing both in the visible and the UV range of the electromagnetic spectrum [183]. The three most important defects in Ge-doped silica are called Ge-NBOHC, GLPC, and Ge(1). The first defect has been observed in both irradiated and non-irradiated $GeO_2$:$SiO_2$ glasses and represents the Ge form of the non-bridging oxygen hole centre found in pure silica [184]. Its structure consists in a dangling bond localised on an oxygen atom bonded to a Ge atom ($\equiv Ge-O^{\bullet}$) [148, 185] and it is responsible for an OA band peaked at 1.97 eV (FWHM = 0.26 eV) [185, 186] and a PL band peaked at 1.84 eV (FWHM = 0.16 eV) [187]. The second defect is the germanium lone-pair centre (GLPC) which is just another name for the Ge oxygen-deficient centre GeODC(II) already discussed in the frame of the $T_2^0$ model. As in the case of Ge-NBOHC, GLPC is present in both native and irradiated silica and is responsible for an absorp-

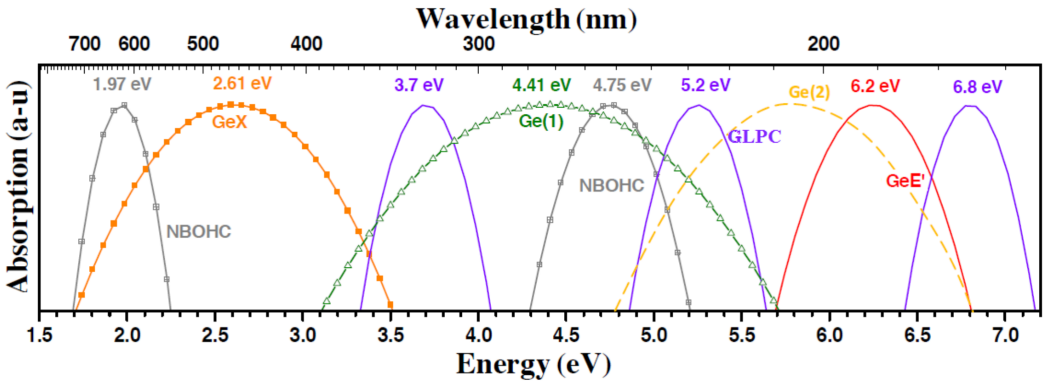


**Figure 2.5.** Absorption bands associated with different Ge-related point defects. Reproduced from Girard *et al.* [196].

tion band at 5.15 eV (the $B_{2\beta}$-band) and for the emission activity at 3.2 and 4.3 eV ($\beta$ and $\alpha_E$ bands) [170, 188]. Under X-ray or UV irradiation, this defect acts as an electron-donor centre towards a second germanium atom according to the reaction [189–192]

$$\underset{\text{GLPC}}{\text{=Ge}\!:} + \underset{[\text{GeO}_4]^0}{\text{=Ge=}} \longrightarrow \underset{\text{Ge(2)}}{[\text{=Ge}^\bullet]^+} + \underset{\text{Ge(1)}}{[\text{=Ge}^\bullet\text{=}]^-}. \tag{2.11}$$

The nature of Ge(2) is very controversial and the twofold-coordinated structure given above is only one of the many models invoked to explain its EPR and optical properties [193, 194]. On the contrary, the structure of the Ge(1) centre is universally attributed to an electron localised at a fourfold Ge atom and its absorption band is known to have a peak at 4.41 eV and a FWHM of 1.1 eV which spans a large portion of the UV–Vis domain. The stability of the $[\text{=Ge}^\bullet\text{=}]^-$ moiety is ensured by the structural relaxation taking place after the electron capture process described in reaction (2.11). In fact, when the unpaired spin moves from the GLPC to the neutral Ge atom, the latter structure undergoes an orthorhombic distortion in which two Ge–O bonds lengthen and the other two shorten. This asymmetry stabilises the system and brings the energy of Ge(1) to a value even lower than that of the neutral =Ge= site [195].

## Aluminium- and phosphorus-related point defects

When aluminium is used as a doping species, the silica network rearranges to form an $[AlO_4]^-$ tetrahedral structure paired with an alkaline or hydrogen cation (in general a $M^+$ ion) acting as charge compensator [197]. When the $[AlO_4^-/M^+]^0$ group is irradiated with high-energy photons, an electron is extracted from the group, the compensator ion moves away, and a stable aluminium-oxygen hole centre (AlOHC)

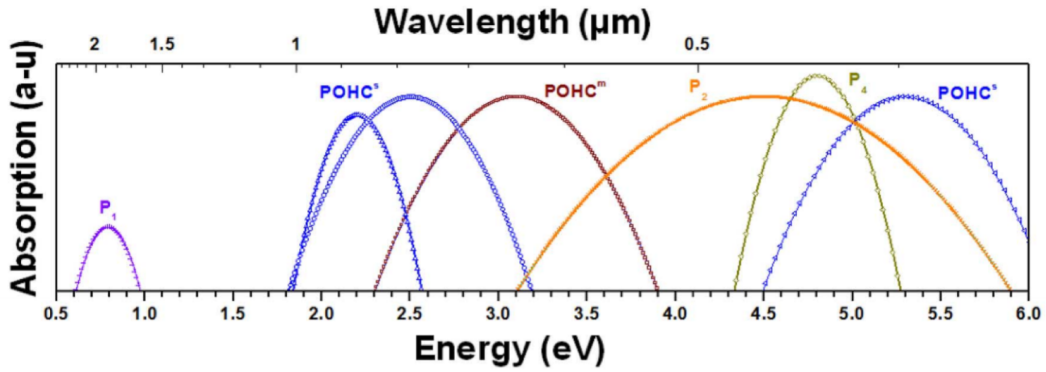


**Figure 2.6.** Absorption bands associated with different P-related point defects. Reproduced from Girard *et al.* [196].

forms:

$$[\equiv \mathrm{Al}-\underset{\substack{\cdot\cdot\\ \cdot\cdot}}{\mathrm{O}}-\mathrm{Si}\equiv]^- \; \mathrm{M}^+ \longrightarrow \underset{\mathrm{AlOHC}}{\equiv \mathrm{Al}-\dot{\underset{\substack{\cdot\cdot\\ \cdot\cdot}}{\mathrm{O}}}-\mathrm{Si}\equiv} + \mathrm{M}^+ + e^-. \qquad (2.12)$$
$$[\mathrm{AlO_4^-/M^+}]^0$$

The first structural model of this defect was proposed in 1955 by O'Brien [198] based on early EPR measurements and was later confirmed by Hartree–Fock and DFT calculations [199, 200]. Its electronic structure consists of a singly occupied molecular orbital (SOMO) deriving mainly from the non-bonding $2p$ orbitals of the non-bridging oxygen and of seven nearly-degenerate HOMO orbitals given by different combinations of the lone pair orbitals of all the four oxygens bonded to the aluminium atom [201]. The HOMO $\longrightarrow$ SOMO transitions have absorption energies in the 1.7–2.5-eV range and are experimentally as a wide OA band with maximum at 2.3 eV and FWHM = 0.9 eV [202, 203]. A second absorption band peaked at 3.2 eV has been theoretically simulated but no experimental confirmation has been provided until now [182].

The radiation-induced generation of AlOHC is often accompanied by the trapping of the electron released during reaction (2.12) at a nearby Al site [202]. This results in the formation of an Al-$E'$ centre which consists in a threefold-coordinated Al atom with an unpaired electron ($\equiv \mathrm{Al}^\bullet$). The literature regarding the optical activity of this defect is very scarse but Hosono and Kawazoe successfully managed to deconvolute the absorption band of irradiated $SiO_2$:$Al_2O_3$ glasses and assigned the band peaking at 4.1 eV to the Al-$E'$ defect [202].

The basic structure of stoichiometric phosphosilicate glasses is the $[PO_4]^0$ tetrahedron formed by a phosphorus atom single-bonded to three bridging oxygen atoms and double-bonded to a fourth non-bridging oxygen atom ($\equiv$P=O) [204–206]. The central P atom features four $sp^3$ hybrid orbitals forming the $\sigma$ bond framework of the $[PO_4]^0$ site and a $3d^1$ orbital (resulting from the promotion of the $3s$ electron not involved in the hybridisation) which is used to form a $\pi$ orbital with an O$(2p)$ electron [207, 208]. As for pure $P_2O_5$ glasses, P-doped silica can also contain phosphate

ions such as the orthophospate group $=P(=O)_2^-$ and the Si-substitutional P centre $[PO_4]^+$ [204, 209]. These charged structures have generally a low concentration but give an important contribution to the radiation sensitivity of phosphosilicate glasses [210]. In fact, when exposed to X-ray [211, 212] or excimer lasers [213, 214], they can react with the $[PO_4]^0$ unit or with a hole generated by the incoming photon to form different point defects:

$$\underset{[PO_4]^0}{\equiv P{=}O} + \underset{[PO_4]^+}{=P^+=} \longrightarrow \underset{\text{m-POHC}}{\equiv P{-}O^\bullet} + \underset{P_2}{=P^\bullet=} \tag{2.13}$$

$$=P(=O)_2^- + h^+ \longrightarrow \underset{\text{s-POHC}}{=P(=O)_2^\bullet} \tag{2.14}$$

The structures called m- and s-POHC belong to the same class of defects called phosphorus-oxygen hole centres [209]. The metastable (m) form has a P atom bonded to three bridging O atoms and to a fourth non-bridging oxygen carrying an unpaired electron. It is responsible of two OA bands centred at 3.1 eV (FWHM = 0.73 eV) and 5.3 eV (FWHM = 0.74 eV). By contrast, the stable (s) variant consists of a P atom bonded to two non-bridging oxygens sharing an unpaired electron and accounts for two absorption bands at 2.2 eV (FWHM = 0.35 eV) and 2.5 eV (FWHM = 0.63 eV). The m-POHC was thought to be observable only at low temperature whereas s-POHC was considered the stable form at room-temperature [211]. More recent results, however, demonstrated that both m- and s-POHC can be detected at room temperature in irradiated P-doped glass samples [212, 215].

The $P_2$ defect corresponds to a P atom hosting an unpaired electron in its $3d$ orbital and bonding four oxygen atoms with single $\sigma$ bonds. It can originate either by electron-trapping at the positively charged diamagnetic precursor $[=P^+=]$ (as shown inj reaction (2.13)) or by hole-trapping at a negatively charged structure $[=P^-=]$. The latter reaction, however, is not favoured since the calculated energy of the moiety $[=P^-=]$ is 2.4 eV more stable than the neutral one [216]. The optical absorption band associated with the $P_2$ defect is peaked at 4.5 eV and has a FWHM of 1.27 eV [182, 215].

# Chapter 3

# Materials and experimental set-ups

The first section of this chapter is dedicated to the description of the HCPV FAE ("Fotovoltaico ad alta efficienza") system used as a starting point to realise the hybrid DL/HCPV module. The rest of the chapter covers the materials, the experimental set-ups, and the techniques used to carry out the experiments described in this thesis.

## 3.1 The HCPV FAE system

The FAE system was developed by IDEA Srl and is currently installed in the solar field of the University of Palermo, Italy [217]. It is composed of four assemblies called semi-trackers interconnected via a reverse return hydraulic layout of a water-based active cooling system. Each semi-tracker consists of ten modules mounted on a super alloy A-286 stainless-steel frame support (Fig. 3.1). The alignment of the modules with the Sun is guaranteed by a 2-axis alt-azimuth tracking system which allows the rotation along the N–S horizontal axis for altitude tracking and the tilt of the E–W transverse axis for azimuth alignment. The two motions are regulated by an AN8 magnetic encoder position sensor and are provided, respectively, by an MR 615 30Q 1/1024 coaxial gear rotational motor and an actuator LA25 linear motor. The tracking accuracy is further increased by using a complementary metal-oxide semiconductor camera installed in the N-side semi-tracker.

Figure 3.2 shows a three-dimensional representation of a FAE system module. The primary concentrator is an ultraclean off-axis parabolic mirror whose surface is

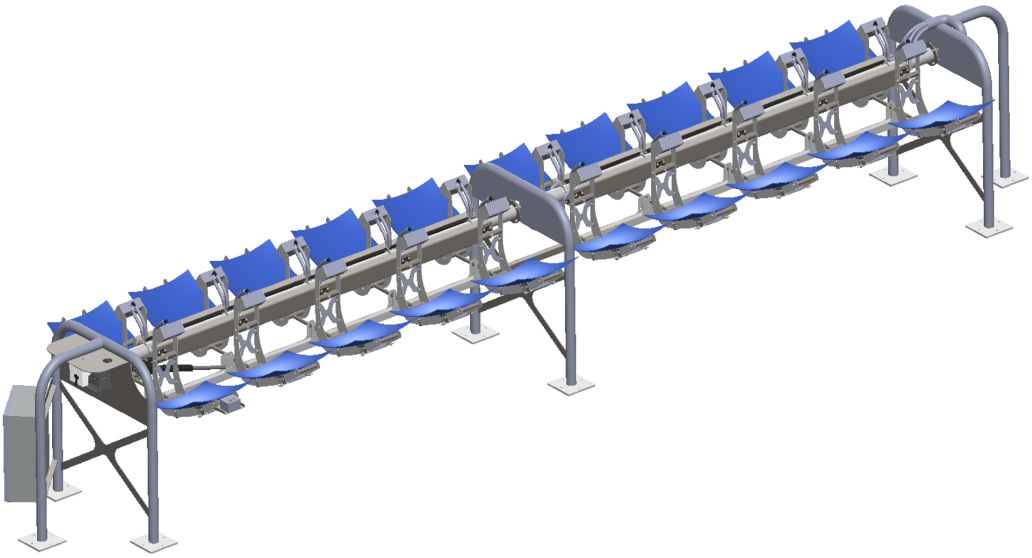

**Figure 3.1.** Three-dimensional representation of two HCPV FAE semi-trakers.

a section of a rotationally symmetric paraboloid of focal length 350 mm. The mirror mechanical centre is 245 mm apart from the paraboloid optical axis and its effective focal length is 363 mm. The plane projection of the mirror is a square of side 450 mm, its curved surface area is approximately equal to 2025 $cm^2$, and its reflectance is 95%, as specified by the manufacturer. The receiver is composed of a BK7 inverted truncated pyramid (ITP) secondary optics placed at the mirror focal point and a TaiCrystal InGaP/InGaAs/Ge triple-junction (TJ) solar cell integrated with an active heat sink. The entry surface area of the ITP is $16\,mm \times 16\,mm = 256\,mm^2$ while the surface area of the TJ cell (corresponding to the ITP exit surface area) is 107.90 mm. This means that the geometric concentration factor is $C_g = 1875\times$ which, for simplicity, will be considered $2000\times$ throughout the text. The multilayer structure of the TJ cell allows a highly efficient absorption of the sunlight due to the different band gaps characterising each sub-cell. In fact, the superficial InGaP layer has a band gap of approximately 1.88 eV and absorbs light in the UV–Vis spectral range. The non-absorbed IR photons pass via tunnel junction to the underlying InGaAs sub-cell where they are captured up to approximately 885 nm (given a band gap of 1.39 eV). The remaining light finally reaches the Ge layer where it is absorbed in the 885–1900-nm range (0.67-eV band gap). The principal features of InGaP/InGaAs/Ge TJ cellS are reported in Fig. 3.3. They are capable of reaching an average daily efficiency of 25% and a maximum efficiency of 30% under $2000\times$ sunlight. After considering parasite consumption and inverter efficiency conversion, each FAE semi-tracker has the capacity to produce up to 0.5 kW of electric power and 1.0 kW of thermal power. The average daily electric and thermal efficiencies of the system are, respectively, 14% and 60% [218–221].

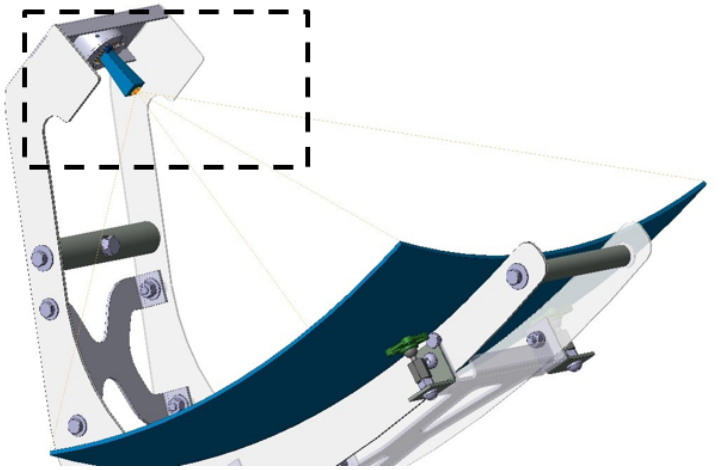

**(a)**

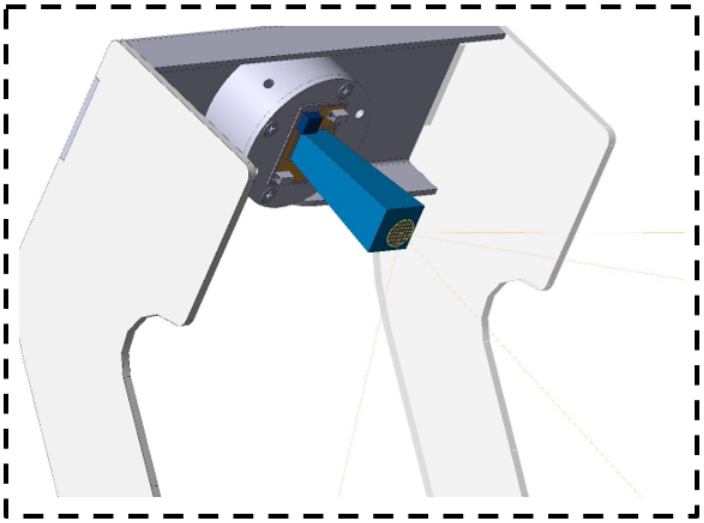

**(b)**

**Figure 3.2.** Detailed view of (a) the HCPV FAE module and (b) its receiver.

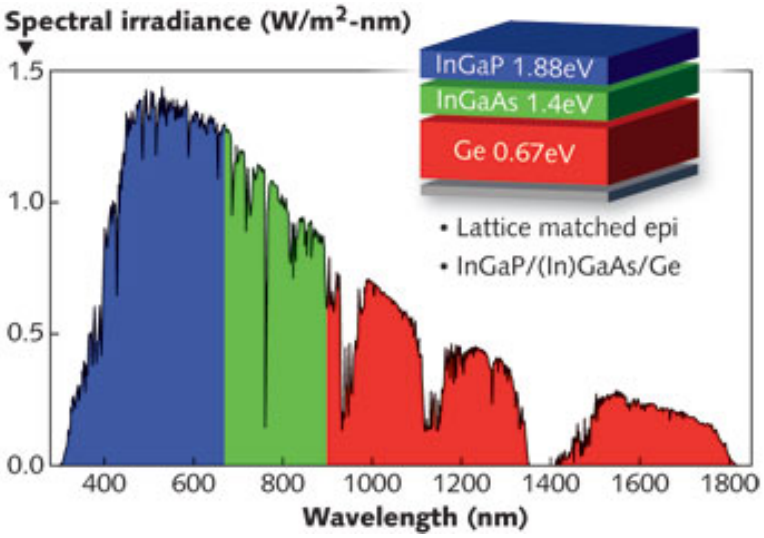


**Figure 3.3.** Structure and absorption spectrum of an InGaP/InGaAs/Ge triple-junction solar cell.

## 3.2 Tested optical fibres

In order to realise the hybrid DL/HCPV module, we selected and tested eight commercial or pre-commercial OFs as representative of different optical properties and chemical composition. All the multimode (MM) fibre used are step-index ones. The first three samples are doped-silica core, pure-silica cladding fibres doped with either aluminium (Fib1), phosphorus (Fib2), or germanium (Fib3). Fib4 is a multimode pure-silica core fibre with a fluorine-doped silica cladding. Fib5, Fib6, and Fib7 are multimode pure-silica core fibres with a hard-polymer cladding and either high- or low-OH content. Fib8 is a multimode fibre with a Ge-doped silica core and a pure-silica cladding. The most relevant specifications for the selected fibres are reported in Table 3.1

**Table 3.1.** Technical details of the fibres tested in this study.

| Label | Fibre ID | Manufacturer | Core/Cladding material | Core diameter (μm) | Transmission mode | Transmission range (nm) | NA |
|---|---|---|---|---|---|---|---|
| Fib1 | IXF-CUST-OPP-12380 | iXBlue Photonics | $SiO_2$:$Al_2O_3$/$SiO_2$ | 62.5 | MM | 400–2200 | 0.13 |
| Fib2 | IXF-CUST-OPP613 | iXBlue Photonics | $SiO_2$:$P_2O_5$/$SiO_2$ | 62.5 | MM | 300–2200 | 0.14 |
| Fib3 | DLPC9 | Corning | $SiO_2$:$GeO_2$/$SiO_2$ | 8.2 | SM | 300–2200 | 0.14 |
| Fib4 | IXF-CUST-SiO2/F | iXBlue Photonics | $SiO_2$/$SiO_2$:SiF | 62.5 | MM | 400–2200 | 0.12 |
| Fib5 | FP200ERT (Low-OH) | Thorlabs | $SiO_2$/Hard polymer | 200 | MM | 400–2200 | 0.50 |
| Fib6 | FP200ERT (High-OH) | Thorlabs | $SiO_2$/Hard polymer | 200 | MM | 300–1200 | 0.50 |
| Fib7 | FP400ERT (Low-OH) | Thorlabs | $SiO_2$/Hard polymer | 400 | MM | 400–1700 | 0.50 |
| Fib8 | GeMM | iXBlue Photonics | $SiO_2$:$GeO_2$/$SiO_2$ | 125 | MM | 400–2200 | n.d. |

## 3.3 Experimental set-ups

### Exposure to the LDLS

The experimental set-up used to investigate the effect of full-spectrum radiation on the selected optical fibres is shown in Fig. 3.4. The light source used to irradiate the fibre samples is an Energetiq EQ-99XFC Laser-Driven Light Source (LDLS) while the detector used to record the transmission spectra is a Hamamatsu C10083MD mini-spectrometer. As shown in Fig. 3.5, the light produced by the LDLS has a flat spectrum across the UV-to-NIR domain and a spectral irradiance $\sim$100 times greater than that of the standard solar spectrum AM1.5D. This means that a very high photon flux is injected into the fibres and that the effect of the exposure is comparable to that of concentrated sunlight. Contrarily to sunlight which has a negligible irradiance below 280 nm, the LDLS features a strong UV component that may represent an important channel for the formation of point defects. However, since all the studied fibres have a low transmission efficiency below 300 nm, the injected UV light cannot propagate through the waveguide body and the signal loss observed in some samples is caused by the visible part of the spectrum.

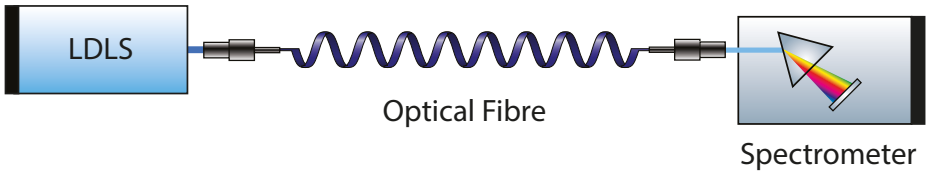


**Figure 3.4.** Experimental set-up for the exposure tests with the LDLS.

### Exposure to pigtailed lasers

The resistance OFs to monochromatic continuous-wave light was tested using the Thorlabs pigtailed (fibre-coupled) diode lasers listed in Table 3.2. Since the coupling of the optical fibre with both the pigtailed laser and the spectrometer must be kept fixed (so as not to affect the measurement results), we designed the set-up shown in Fig. 3.6 to allow the switching between the source beam (the pigtailed laser) and the probe beam (a non-degrading Thorlabs High-Intensity Halogen Lamp Light Source OSL1 with $E = 175\,\mathrm{W}\cdot\mathrm{mm}^{-2}$).

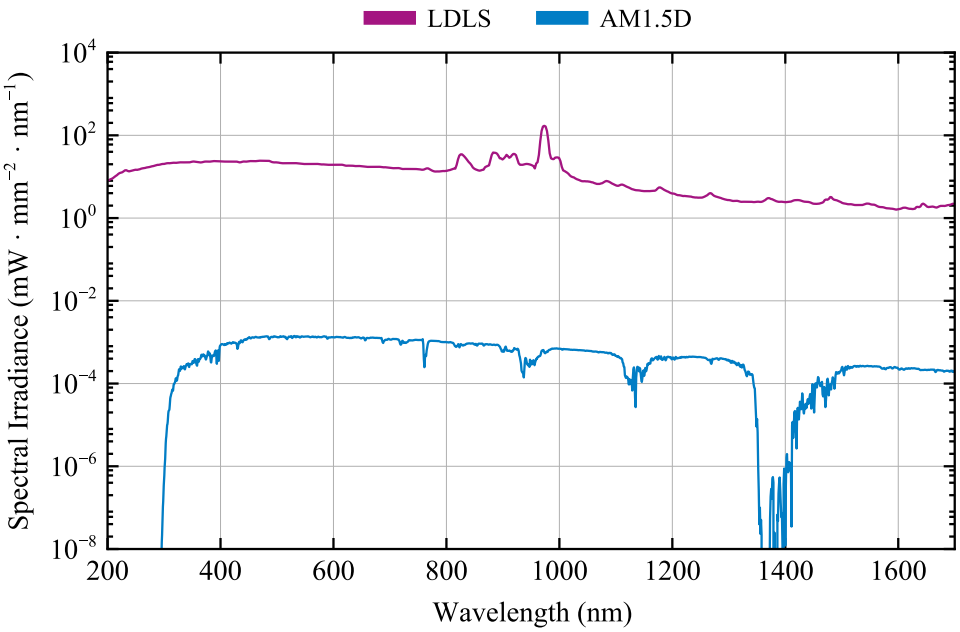


**Figure 3.5.** Spectral radiance of the Energetiq EQ-99XFC LDLS source (red line) and standard direct solar spectrum AM1.5D (blue line).

**Table 3.2.** Technical details of the Thorlabs pigtailed diode lasers.

| Laser ID | Peak energy (eV) | Output power (W) | Laser irradiance ( $W \cdot mm^{-2}$) |
|---|---|---|---|
| LP405-MF300 | 3.06 | 300.0 | 120 |
| LP520-SF15 | 2.38 | 15.0 | 1667 |
| LP660-SF60 | 1.88 | 60.0 | 3750 |
| LP785-SF100 | 1.58 | 100.0 | 4000 |
| LPS1060-FC | 1.17 | 50.0 | 1389 |

## Exposure to the Nd:YAG laser

A Q-switched Nd:YAG laser (Quanta System SYL-201) was used to test the resistance of OFs to high-energy monochromatic pulsed light in the UV–Vis spectral range. The active medium is an $Nd^{3+}$-doped yttrium-aluminium-garnet (YAG) crystal pumped by a pulsed Xe discharge lamp via the ∼800-nm absorption transition of the $Nd^{3+}$ ions. The Q-switching is triggered by an electro-optic crystal placed within the laser cavity. When this crystal is not polarised, the cavity Q factor is low and the population inversion is high without any laser oscillations. When it is polarised, the Q factor increases and the laser action starts with a strong initial inversion which builds up an intense pulse of 200 mJ and 5 ns.

Since the transmission efficiency of optical fibres is extremely sensible to any vari-

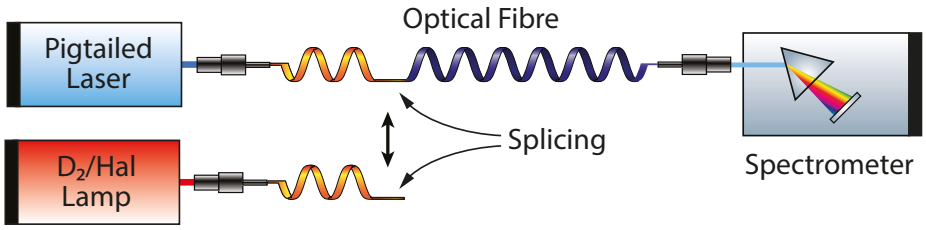


**Figure 3.6.** Experimental set-up for the irradiation tests with pigtailed lasers.

ations in the light injection conditions, the *online* RIA measurements were carried out using an *ad hoc* experimental set-up shown in Fig. 3.7. The fibre, the lenses, and all the instruments were kept fixed during the exposure, and only the redirecting mirror $M_2$ and the two laser beam traps ($BT_1$ and $BT_2$) were moved. The optical path followed by the light can be summarised as follows: The laser beam is reflected by the two mirrors $M_1$ and $M_2$, passes through through two neutral-density filters (NDFs) to reduce the radiative flux and then through the relay lens (RL) to reduce its diameter. The light is then injected into the fibre and blocked by the beam trap in $BT_2$ at the exit of the optical fibre. After 15 min of irradiation, the optical path of the laser beam is interrupted by using the $BT_1$ trap and the optics $M_2$ and $BT_2$ are moved away. In this the light produced by a combined deuterium and halogen light source (Avantes AvaLight-DH-S-BAL) can arrive to an Avantes S2000 spectrometer after passing though the tested OF.

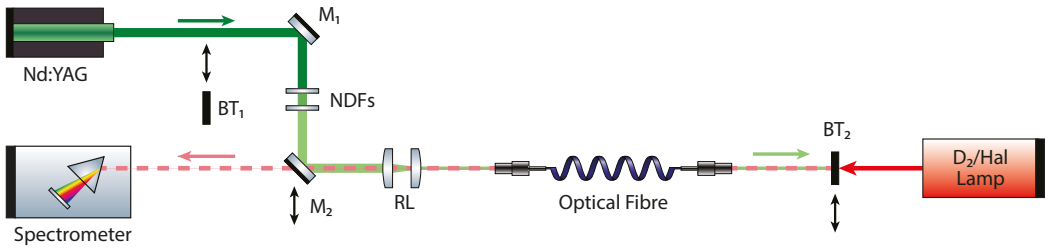


**Figure 3.7.** Experimental set-up for the Nd:YAG irradiation tests.

# Chapter 3

# Design and ray tracing analysis of the DL/HCPV system

A key factor in the development of a hybrid DL/HCPV system is the coupling between the concentrator and the optical fibres. While the former dictates the maximum flux density reaching the absorber, the latter determines the net irradiance absorbed by the solar cell(s) and thus the operative concentration ratio of the system. In order to ensure the best performance, the light beam reflected by the mirror needs to be adapted to match the aperture size and acceptance angle of the optical fibre into which it is injected. In this chapter we describe the strategy adopted to simulate different optical receivers and evaluate their theoretical efficiency. To this aim, we used the simulation software Zemax OpticStudio18 to recreate a model of the HCPV "Fotovoltaico ad alta concentrazione" (FAE) module in its original design and reproduce its known properties. This preliminary task has never been addressed, not even in the the R&D phase of the FAE, and was needed to guarantee the reliability of the proposed customised optics. Once we obtained a model correctly reproducing the system properties as measured on the field, we removed the secondary optical element of the module and substituted it with different optical receivers. The shape and positioning of each element was optimised and its properties were evaluated using the ray-tracing method. The last section of the chapter deals with the comparative analysis of all the simulated optics. Since our aim was to identify the best performing receiver for the industrial development of the hybrid system, the evaluation was based on optical performance indicators as well as on mechanical and engineering criteria.

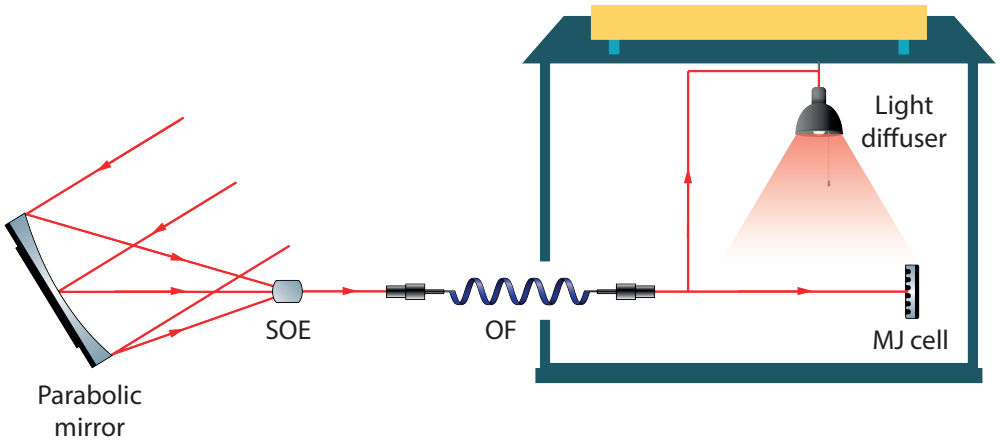


**Figure 3.1.** Schematic representation of a building-integrated DL/HCPV system.

## 3.1 Calibration of the model

The Zemax non-sequential model of the original FAE module consists of a light source approximating the Sun, a primary parabolic mirror, and a secondary optical element (SOE). All these elements were simulated using the information shared by IDEA Srl and their optical properties were analysed by placing a flat detector along the optical path, in correspondence of the mirror aperture, the mirror focus, and the SOE back face. The aim of this first part of the study was to calibrate the model by achieving the best agreement between experimental and simulated properties.

### The light source

The geometric and radiometric features of solar radiation have been discussed in detail in 1.2. For the purpose of creating a realistic Zemax model, it suffices to remember that the sunlight reaching the Earth has a divergence half-angle $\xi_s = 4.653\,\text{mrad}$ and a direct normal irradiance of $1000\,\text{W}\cdot\text{m}^{-2}$. The source used to reproduce a light beam with such characteristics is the "Source Radial" object, that is a radially symmetric source emitting rays into a hemisphere. This was selected among other options because of its flexibility and suitability for modelling complex illumination systems. The centre of the source was taken as the origin of the global Cartesian coordinates system *GXYZ* describing the position of the entire HCPV module. The source was positioned as shown in Fig. 3.2 with its surface parallel to the *XY*-plane and the emitted rays travelling in the positive direction of the *Z*-axis. The power was adjusted to obtain a flux density of $1000\,\text{W}\cdot\text{m}^{-2}$ on a $450\times 450\,\text{mm}^2$ "Detector Surf" ($D_1$) placed parallel to the source plane. As shown in Fig. 3.3a, the irradiance ($E$) absorbed by the detector is spatially uniform and has a value of $1000\pm 5\,\text{W}\cdot\text{m}^{-2}$. The angle distribution of the rays is given in Fig. 3.3b in

the form of a normalised sunshape $\bar{L}(\xi)$. In the range $0 \leq \xi \leq 3.2$ mrad, the outcome of our simulation almost perfectly overlaps with the reference sunshape calculated using Eq. (1.4). At higher angles, the normalised radiance differs by approximately 1% from the theoretical value, which is negligible for our purposes. By integrating $\bar{L}(\xi)$, we find that 30% of the radiation is emitted as a nearly-collimated beam of light whereas the remaining part forms bundles of rays with divergence angles of 1 to 5 mrad.

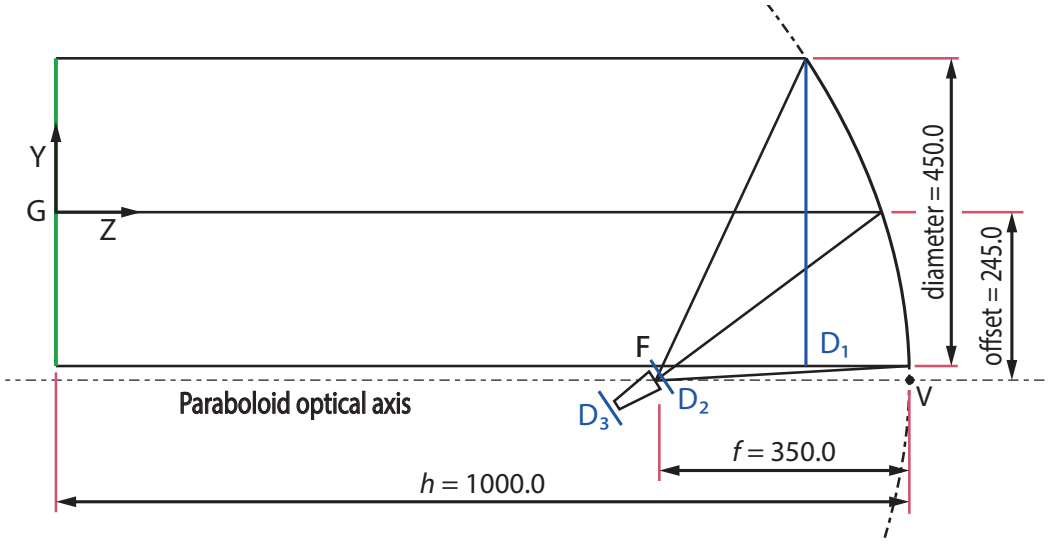


**Figure 3.2.** Schematic of the FAE module as designed in Zemax (not in scale).

## The primary optics

The primary concentrator of the module is an off-axis parabolic (OAP) mirror whose reflective surface is a segment of the quadric

$$z = -\frac{x^2 + y^2}{4f} + h.$$

The parameters $f$ and $h$ completely define the so-called parent paraboloid and correspond to the mirror focal length and vertex $z$-coordinate, respectively. To obtain a square parabolic shell corresponding to the OAP mirror, the paraboloid is intersected with a prism of major axis parallel to the $Z$-axis. In Zemax this was realised by using the "Standard Surface" object and setting the following parameters: $f = 350.000$ mm, $h = 1000.000$ mm, diameter $= 450.0$ mm, offset $= 245.000$ mm, aperture $= 450.000$ mm, and reflectivity $= 0.95$. Since the light emitted by the Source Radial is not collimated, the flux density received by the mirror depends on its position in the global coordinate system. Since the source was modelled to produce a flux density of $1000\,\mathrm{W}\cdot\mathrm{m}^{-2}$ on the $D_1$ surface, the parabolic concentrator was placed with its upper edge at the detector position in order to receive the same

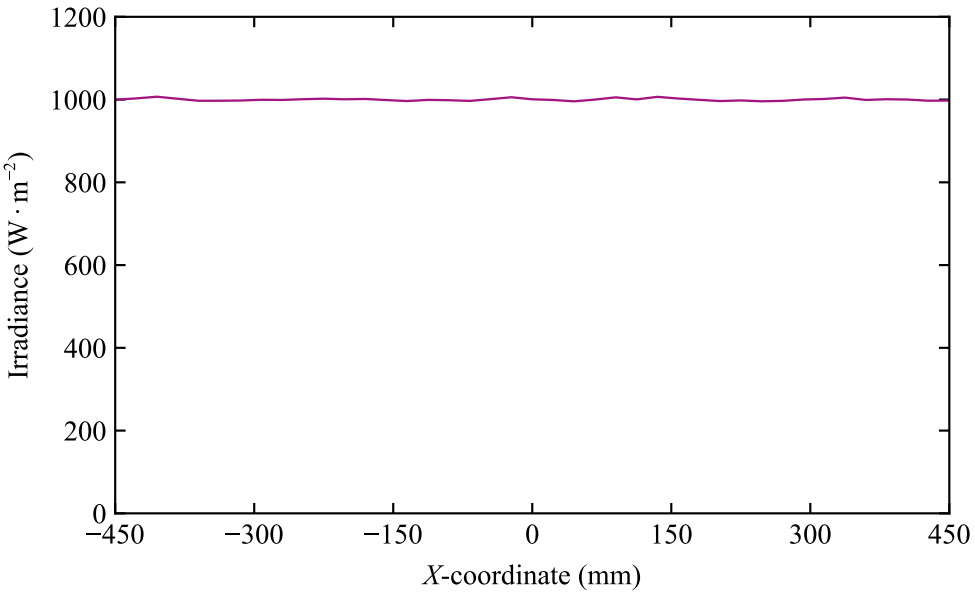


**(a)**

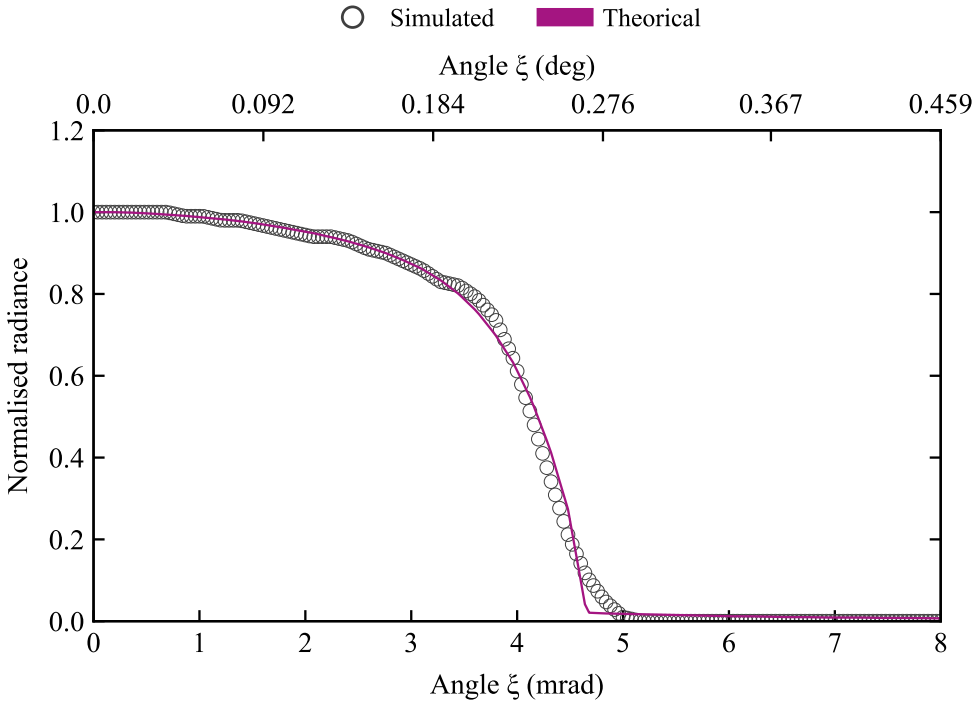


**(b)**

**Figure 3.3.** (a) Irradiance received by the detector placed before the parabolic mirror. (b) Angular distribution of the normalised radiance for the simulated model and the limb-darkened sunshape proposed by Buie *et al.* [222]. A CSR = 0.04 was used to calculate the theoretical curve.

amount of radiation (see Fig. 3.2). A realistic view of the modelled mirror is given in Fig. 3.4.

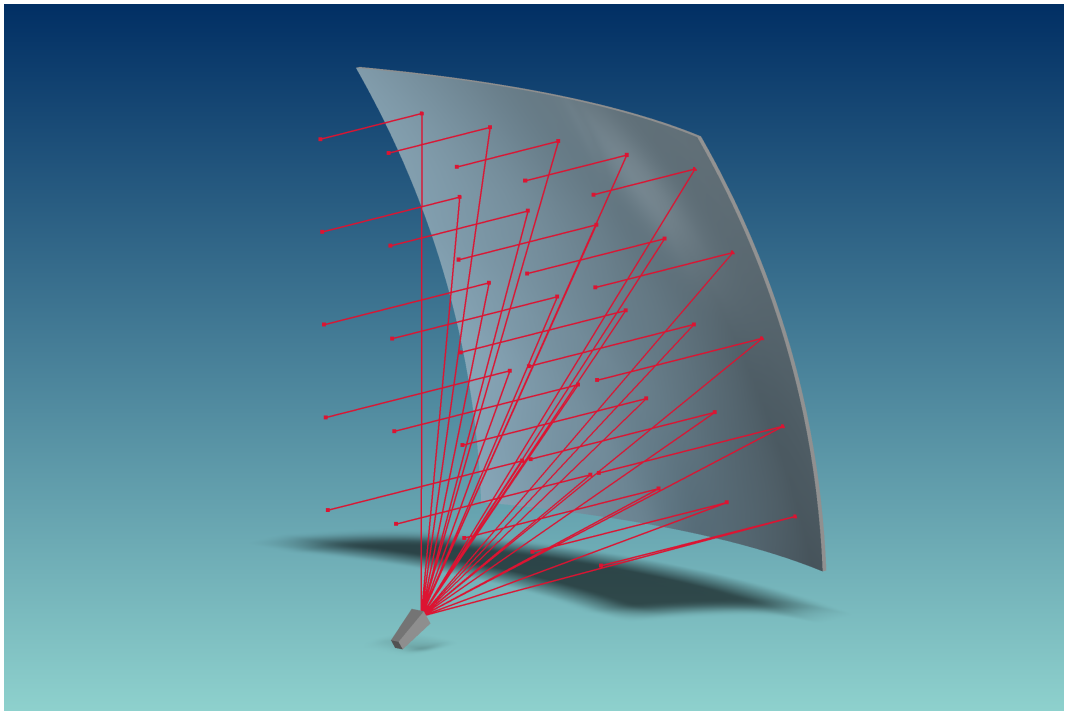

**Figure 3.4.** Realistic view of the simulated FAE module showing the light rays (in red), the parabolic concentrator, and the ITP optics.

To assess the accuracy of the simulation, a Detector Rectangle $D_2$ was centred at the mirror focal point $F$ and tilted normal to the central ray axis. The image formed by the reflected rays (Fig. 3.5a) is an ellipse centred at $F$ with axes $\sigma_x = 2.400\,\text{mm}$ and $\sigma_y = 2.580\,\text{mm}$. However, since the eccentricity is

$$e = \sqrt{1 - \left(\frac{\sigma_x}{\sigma_y}\right)^2} = 0.367,$$

the image shape can be approximated by a circle of radius

$$r = \left(\frac{\sigma_x + \sigma_y}{2}\right) \pm \left|\frac{\sigma_x - \sigma_y}{2}\right| = 2.49 \pm 0.09\,\text{mm}.$$

This value is almost half the image diameter experimentally measured for the real FAE concentrator (10 mm), indicating that the latter is probably affected by surface irregularities or misalignment issues which cannot be easily modelled. From the projection plots in Fig. 3.5a, we can also verify that the irradiance absorbed by the detector has a constant value of $23 \pm 1\,\text{W}\cdot\text{m}^{-2}$ in the interval $0 \leq r \leq 0.6\,\text{mm}$ and smoothly decreases to zero as $r$ gets closer to the image rim. This behaviour is mainly due to the non-centrosymmetric nature of the mirror and the astigmatism and coma caused by the divergent light beam. In fact, when the propagation axis of

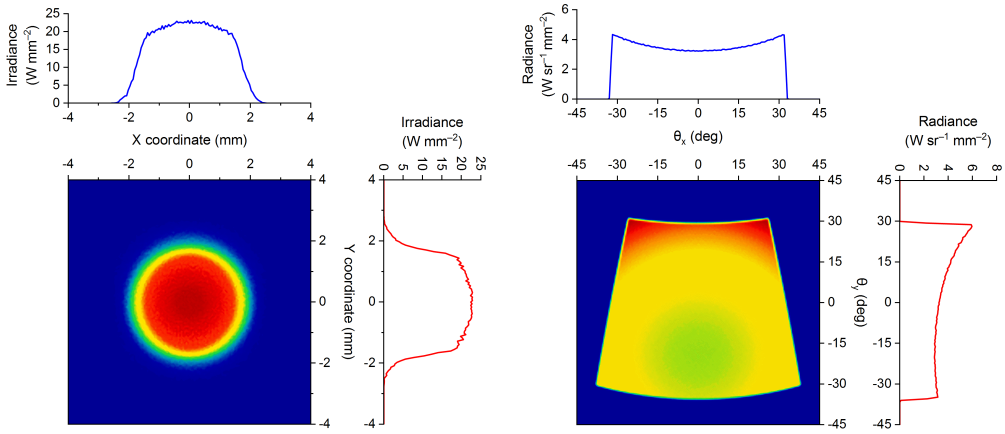


**(a)** **(b)**

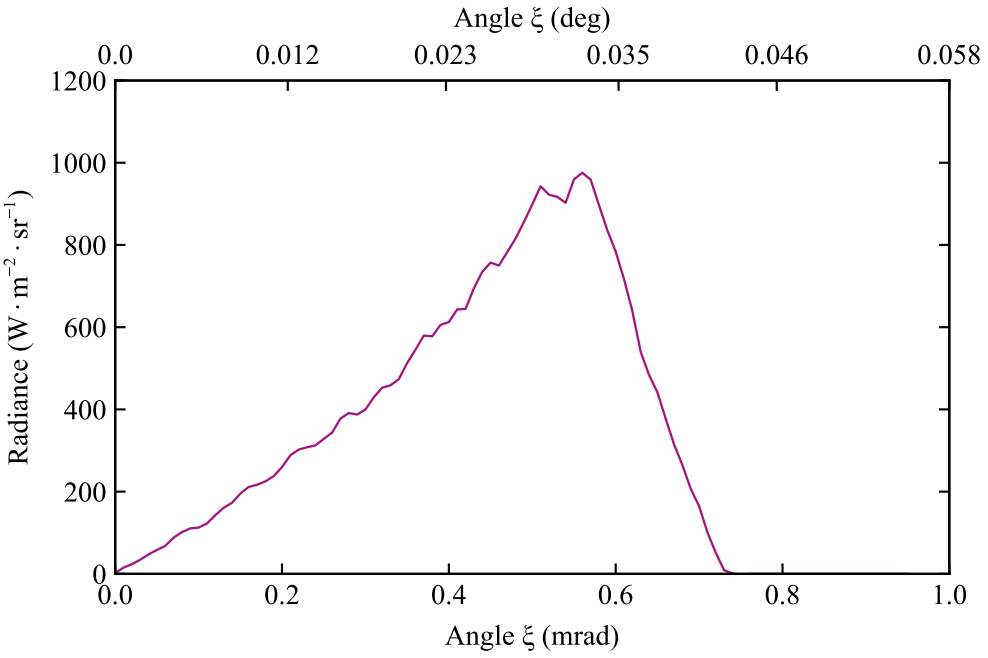


**(c)**

**Figure 3.5.** Radiance and irradiance received by the detector placed at the mirror focal point. (a) Irradiance in position space, (b) radiance in angle space, and (c) radiance as a function of the azimuthal angle with respect to the local *z*-axis.

the incident rays is slightly tilted with respect to the mirror optical axis, the reflected rays are no longer focused at a single point but rather form an envelope of rays called a catacaustic (Fig. 3.6). In addition, the lack of radial symmetry determined by the off-axis geometry causes the image formed in the tangential ($YZ$-) plane to fall short of the image formed in the sagittal ($XZ$-) plane. This causes the displacement of the maximum flux density from the geometrical focal plane and a partial defocus (astigmatism) of the image.

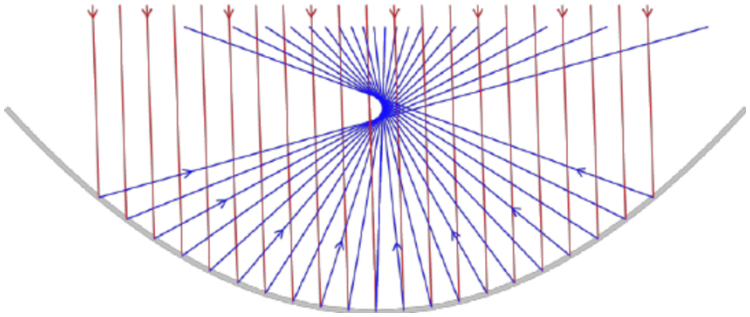

**Figure 3.6.** Ray diagram for a collimated beam of light hitting a parabolic mirror with a non-zero angle with respect to the optical axis. The image formed on the focal plane is catacaustic even for on-axis parabolic mirrors. Reproduced from April *et al.* [223].

To have a better insight of the beam geometry at the focal point, we calculated the radiance as a function of the the angles $\theta_x$ and $\theta_y$ formed by each light ray with the coordinate axes $x$ and $y$. As shown in Fig. 3.5, the radiation travelling parallel to the $xz$-plane (blue line) hits the detector surface with an angle distribution symmetric about 0° and a maximum angle of 32.40°. The rays travelling parallel to the $yz$-plane (red line), on the other hand, has an asymmetric profile which ranges between $-28.8°$ and 32.1°. As for astigmatism-like aberrations, the cause of the asymmetry is the off-axis geometry of the concentrator. In fact, if we ideally subdivide the mirror into infinitesimal square surfaces, we see that each surface receives a different amount of light depending on its orientation with respect to the light source. Since the geometry of system is such that the bottom part of the mirror receives a higher flux density than the upper part, the radiance on the detector is higher for rays coming from the bottom of the mirror (*i.e.* arriving at higher angles with respect to the surface normal) than from its top. If we transform $\theta_x$ and $\theta_y$ into the azimuthal angle $\xi$ (by projecting each light ray onto the $z$-axis) we can evaluate the angular aperture of the beam hitting the detector by simply analysing the radiance as a function of $\xi$. As reported in Fig. 3.5b, most of the light (almost 80% of the total radiation) arrives at $D_2$ with an angle $\xi \leq 32°$. The integral of $L$ over the image area and detector solid angle is equal to 191.53 W, which is close to the theoretical value of 192.38 W calculated on the basis of the geometry and reflectivity of the concentrator.

## The inverted truncated pyramid

The secondary optical element of the FAE module is a dielectric inverted truncated pyramid (ITP) made of BK7 glass and placed at the mirror focal point. In our simulation it was modelled using a "Rectangular Volume" with a front and a back face of, respectively, $16.000 \times 16.000$ and $10.000 \times 10.000\,\mathrm{mm}^2$. Its longitudinal length was set to 40.000 mm and the built-in N-BK7 glass was chosen as a material. The object was placed with the front face centred at the mirror focus and its body was rotated $-33°$ about $X$-axis as illustrated in Fig. 3.4.

The light entering the ITP is totally internally reflected multiple times before reaching the back face and being refracted outwards. To measure the properties of the output beam, we put a Detector Rectangle $D_3$ at the exit of the ITP and aligned it with its optical axis. Due to the homogenisation brought about by the optics, the image formed on $D_3$ has different properties from that on the focal plane. Figure 3.7 shows that the pattern of the transmitted rays form a sharp square of side $10.027 \pm 0.001$ mm with a fairly constant flux density of $2.25 \pm 0.05\,\mathrm{W \cdot m^{-2}}$. A small asymmetry is visible along the local $y$-axis due to the aberrations introduced by the OAP mirror. The flux received by the detector surface is 154.54 W, indicating that nearly 19% of the light redirected by the mirror is lost by both reflection and outward refraction at the ITP glass/air interfaces. These results are consistent with the data shared by the designers of the real FAE system.

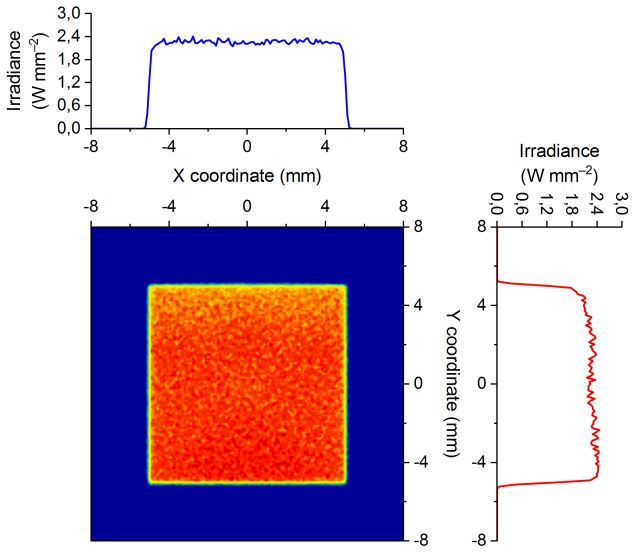


**Figure 3.7.** Irradiance in position space received by the detector placed at the ITP back face.

## 3.2 Bare fibres

Considering that the aim of our simulation was to find the best design for a fibre optics receiver, the first configuration to be evaluated was that of a bare optical fibre placed at the mirror focus without any intervening coupling optics. To have a wider comparison, we simulated three step-index multimode optical fibres of core/cladding diameter 50/125, 200/225, and 400/425 µm, respectively. Since Zemax does not have a default object for optical fibres, we used two coaxial "Cylinder Volumes" ($CV_1$ and $CV_2$) to recreate the core and cladding of each OF. The numerical apertures (NA) was defined by fixing the core refractive index to 1.4613 (as given in the Filmetrics' online database [224]) and adjusting the cladding index to the desired value. Specifically, the core/cladding indices were set to 1.4613/1.4440 for the first fibre (NA = 0.22), 1.4613/1.4079 for the second fibre (NA = 0.39), and 1.4613/1.3730 for the third one (NA = 0.50).

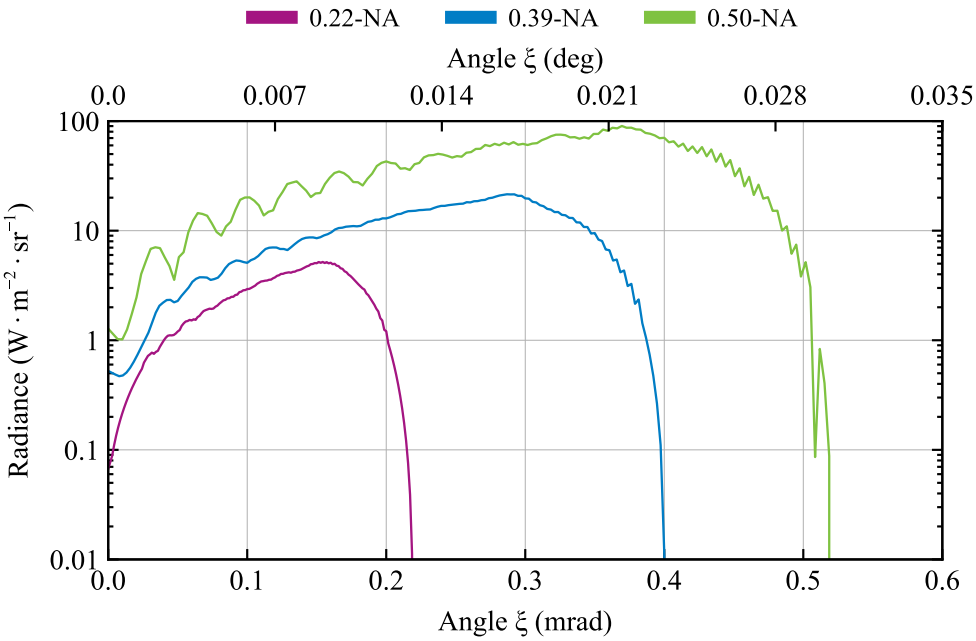


**Figure 3.8.** Radiance in angle space received by the detector placed at the fibre far end.

Figure 3.8 shows the radiance in angle space received by a detector ($D_4$) placed at the far-end face of the three simulated OFs. Since the radiance is very different from the three models, a base-10 log scale is used for the *y*-axis. As dictated by their NA's, the beam transmitted by each OF is projected onto the detector as a cone of light of different angular aperture. For the 0.22-NA fibre, the maximum angle is 0.22 rad (13°), for the 0.39-NA fibre it is 0.40 rad (23°), and for the 0.50-NA fibre it is 0.52 rad (30°). The perfect accordance between these values and the

theoretical angular aperture calculated as $\xi = \arcsin(\mathrm{NA})$ supports the reliability of our simulations. By integrating the radiance $L(\xi)$ we obtain the following values for the transmitted radiant flux: 0.04 W for the 0.22-NA OF, 0.22 W for the 0.39-NA OF, and 0.90 W for the 0.50-NA OF. The difference between the three values is mainly determined by the size of the fibres and varies as the square of their diameter.

To maximise the flux collected by the fibres, we explored the possibility of using a large number of mechanically fixed OFs to form a fibre bundle. The simulation of this collection of OFs is not an easy task in Zemax and for this reason we proceeded with a first-principle calculation. Given that the bundle entrance face must have an area as close as possible to that of the mirror image, an optimised bundle should consists of 151 cladding-less, 400-µm core diameter fibres as shown in Fig. 3.9. Since the flux transmitted by a single fibre is 0.90 W (as determined above), a so-formed bundle can collect a light power of roughly 135 W. This value is in agreement with the geometry-based calculations which tells us that $\sim$10% of the incoming flux is lost by interstitial leakage and approximately 13% of the injected light is refracted out of the fibre due to the high angle of incidence. The net transmitted flux is thus equal to 165 W.

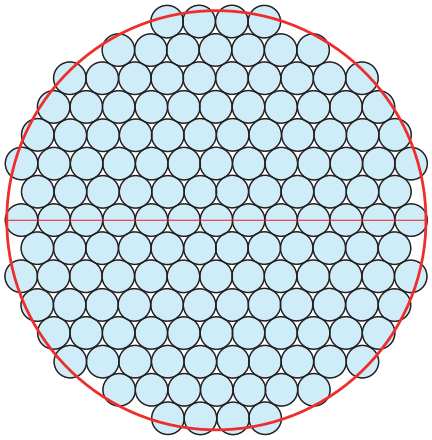

**Figure 3.9.** Bundle formed by 151 mechanically fixed optical fibres of core diameter 400 µm. The red circle represent the mirror image outer rim (diameter = 5.16 mm).

## 3.3 End-capped fibre

As a different fibre-based optics, we simulated the splicing of a 0.50-NA fibre with an additional Cylinder Volume ($CV_3$) serving as an end cap. This allowed the incoming light to expand evenly in the dielectric material of the OF and achieve a higher

injected flux. The geometry of $CV_3$ was defined by setting a length $L = 30.0$ mm, a front-face diameter $d_1 = 1.000$ mm, and a back-face diameter $d_2 = 0.425$ mm. Since real end caps are made of the same material as the cladding of the fibres they are spliced with, the refractive index of the glass was set equal to that of $CV_2$.

Unlike the preceding cases, the geometry and position of the end cap were optimised using a damped least square algorithm to achieve the best OF-coupling efficiency. To this end, the diameter $d_2$ and all the fibre parameters were set as fixed while $L$ and $d_1$ were treated as variables. To avoid unpredictable deformations of the optics, we also imposed $L_{max} = 80.0$ mm and $d_{1,max} = 60.0$ mm as constraints on the system. These choices are justified by considering that the end cap needs to adapted to the 0.5-NA fibre and that we do not want it to be too long or massive, as this would determine a higher production cost and a lower mechanical resistance.

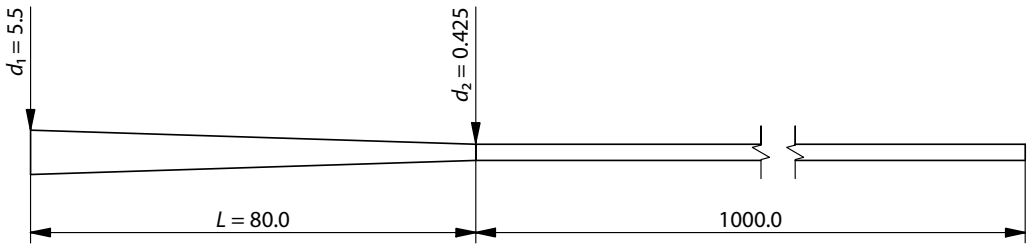


**Figure 3.10.** Schematic of the optimised end-capped optical fibre (not in scale). All dimensions are expressed in mm.

At the end of the optimisation process, the end cap was positioned 0.3 mm after the mirror focus and at an angle of $-43.2°$ with respect to the $XZ$-plane. The diameter $d_1$ was enlarged to 5.5 mm and $L$ reached the limiting value of 80.0 mm, as shown in Fig. 3.10. From the irradiance distribution shown in Fig. 3.11a, we see that the image collected by the detector $D_4$ has a smaller diameter ($3.0 \pm 0.1$ mm) and a lower integrated flux (62.5 W) than that produced by the mirror. This indicates that almost 70% of the light is lost when passing through the optics. Also, the radiance angular distribution in Fig. 3.11b reveals that the multiple total internal reflections inside the end cap increase the beam aperture and result in a very wide angular distribution of the rays leaving the fibre. By comparing this result with that of a single fibre, it is clear that the use of an end cap greatly improves the light collection efficiency of the waveguide but takes the angular properties of the emitted beam to the extreme. Since fibre bundles guarantee a higher transmitted flux and a lower sensibility to mechanical stress, their use should be preferred over end-capped fibres.

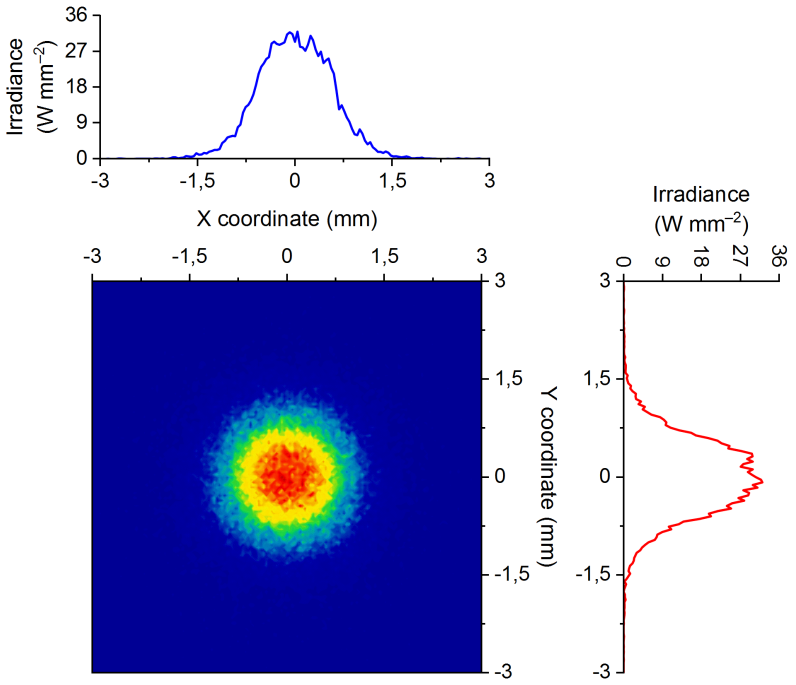


**(a)**

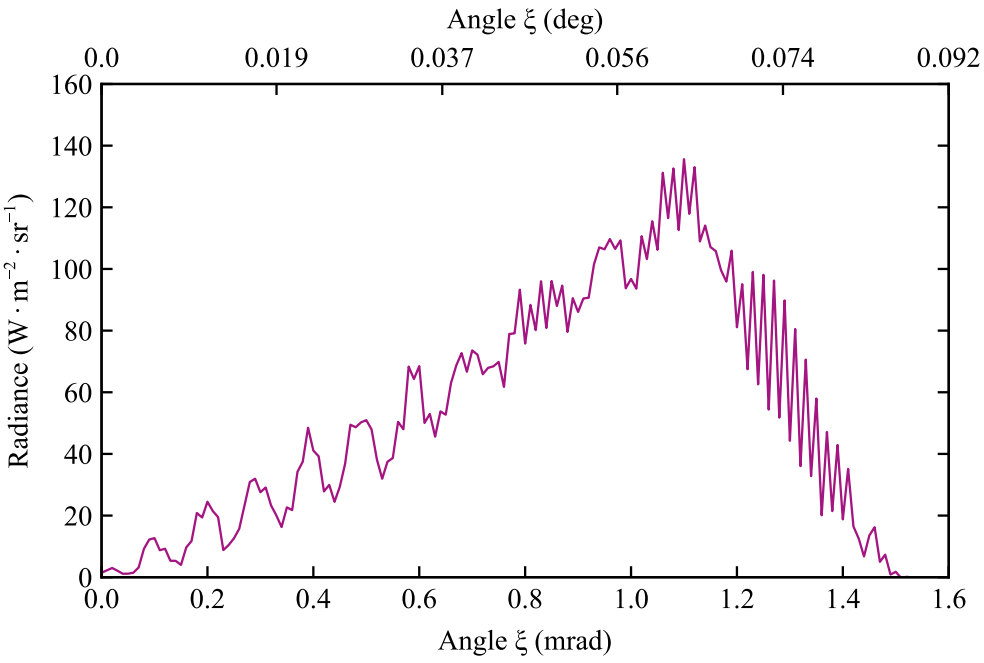


**(b)**

**Figure 3.11.** Radiance and irradiance received by the detector placed at the end-capped fibre far end. (a) Irradiance in position space, and (b) radiance as a function of the azimuthal angle with respect to the local $z$-axis.

## 3.4 Aspheric lens

A different way of designing an OF-based solar device is to place a secondary optical element between the mirror and the fibre(s) in order to improve sunlight collection and injection. The first optics to be simulated was an aspheric lens, that is a lens designed to compensate for the geometrical and chromatic aberrations of a specific optical system. Its surface profile is defined by the quadric function

$$z(r) = \frac{r^2}{R\left(1+\sqrt{1-(1+K)\frac{r^2}{R^2}}\right)} + \alpha_4 r^4 + \alpha_6 r^6 + \cdots,$$

where $z$ is the displacement of the lens surface from the vertex in the direction of the optical axis, $r$ is the distance from the centre of the lens, and the coefficients $\alpha_i$ describe the deviation of the surface from the axially symmetric quadric specified by the radius of curvature $R$ and the conic constant $K$ [225]. For the sake of clarity, the terminology and geometrical parameters used to describe the optical features of an aspheric lens are reported in Fig. 3.12.

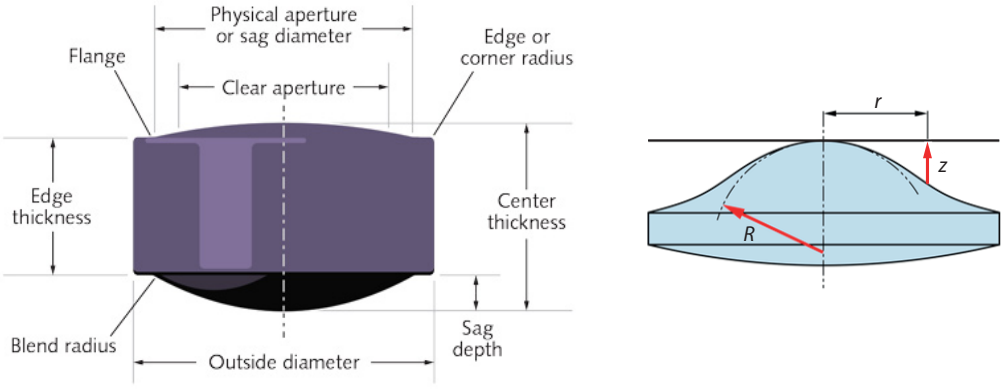


**(a)** **(b)**

**Figure 3.12.** Schematic of a generic aspheric lens. (a) Terminology and (b) geometrical parameters.

Due to the complexity of the lens — and the high number of parameters — the optimisation process was carried out in two phases. In the first phase an N-BK7 aspheric lens was designed using a "Standard Lens" object and a simplified source emitting only collimated light. After the first optimisation round, the Source Radial was set back to the sunshape-like distribution and a second optimisation was run on the lens. This allowed us to partially correct the aberrations introduced by the non-collimated sunlight beam and achieve the highest irradiance at the lens rear focal point.

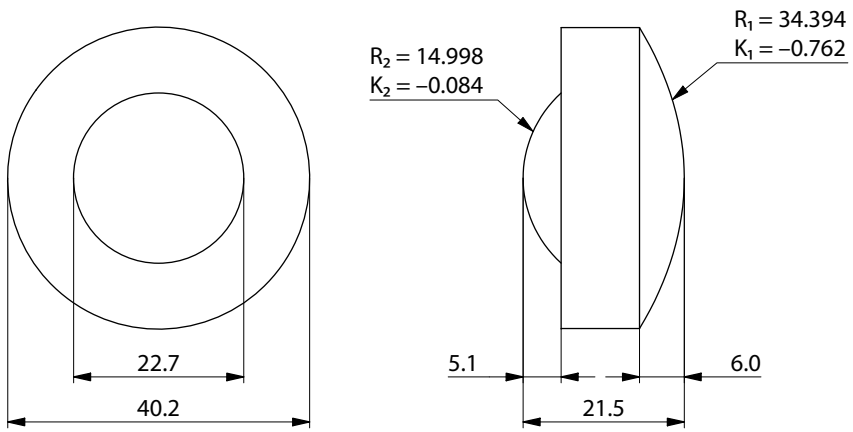


**Figure 3.13.** Schematic of the optimised aspheric lens. All dimensions are expressed in mm.

The schematic in Fig. 3.13 shows that the final aspheric lens has an outside diameter of 40.2 mm and a centre thickness of 21.5 mm. The front face sag diameter is the same as the outside diameter whereas the back face sag diameter is equal to 22.7 mm. The two aspheric surfaces are prolate ellipses defined by the parameters: $R_1 = 34.394$ mm, $K_1 = -0.762$, $R_2 = 14.998$ mm, and $K_2 = -0.084$. The sag depth is equal to 6.0 mm for the front face and 5.1 mm for the back face. The distance of the lens from the mirror focus defines the front focal length (12.9 mm) while the distance of the image from the apex of the back surface defines the back focal length (70.6 mm). The angle formed between the lens optical axis and the global $Z$-axis is $-47.52°$.

The focusing properties of the lens after the first and the second optimisation stage were evaluated using a Detector Rectangle ($D_5$) placed at the lens rear focus. The radiance and irradiance distributions resulting from the first simulation are shown in Fig. 3.14. In the first plot, the image formed by the intersection of the light rays has a point-like shape with a very small diameter ($0.520 \pm 0.005$ mm) and a thin circular fringe located far away from the centre. The maximum angle of the rays hitting the detector surface (as measured from the local $z$-axis) is $\sim 16°$. Moving from the parallel- to the divergent-ray simulation, the quality of the image decreases significantly due to the mirror inability to correctly focus the tilted rays. As shown in the distributions in Fig. 3.15, the image obtained in the second simulation suffers serious aberration problems which result in an increased image diameter ($13.2 \pm 0.2$ mm) and maximum incidence angle ($\sim 18°$) of the refracted rays. In both calculations the flux transmitted by the lens is 122.4 W, which means that 36% of the incoming radiation is reflected away at the lens front face.

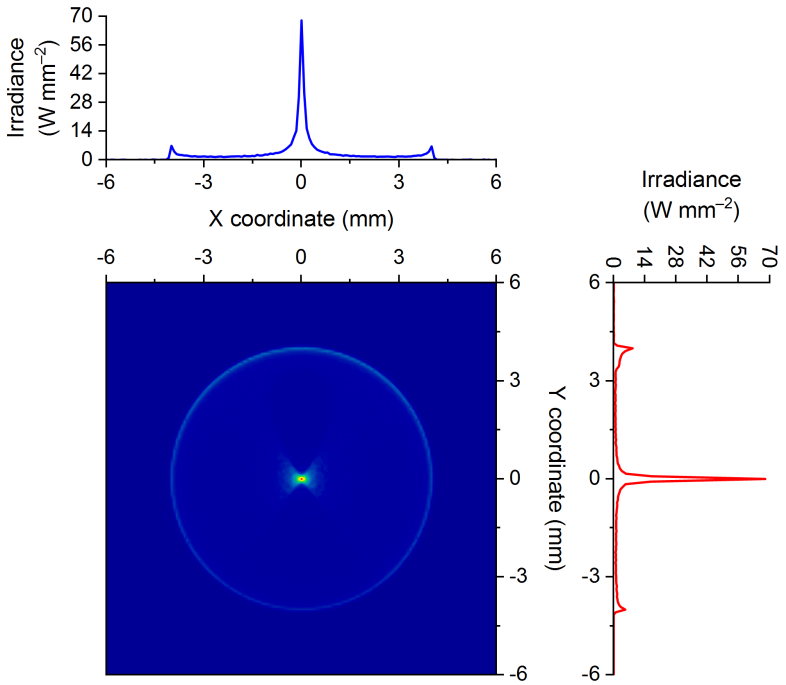


**(a)**

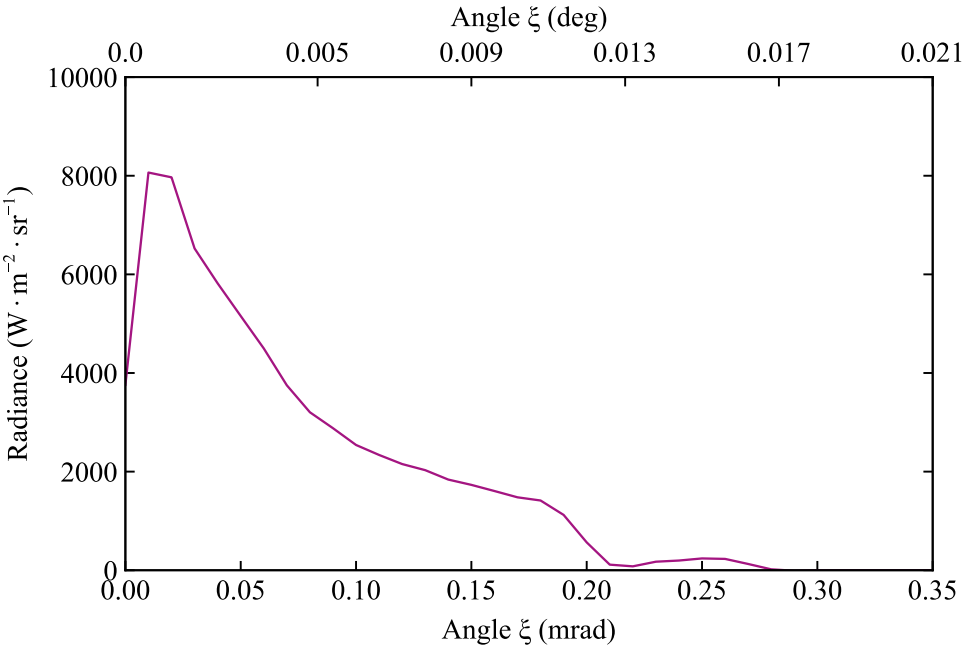


**(b)**

**Figure 3.14.** Radiance and irradiance received by the detector placed at the lens back focus in the collimated-beam simulation. (a) Irradiance in position space, and (b) radiance as a function of the azimuthal angle with respect to the local $z$-axis.

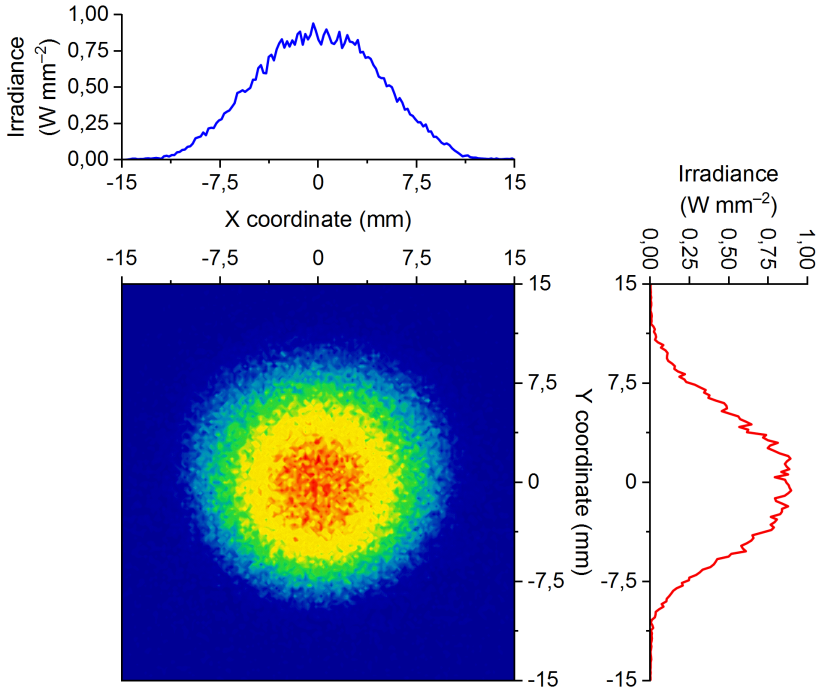


**(a)**

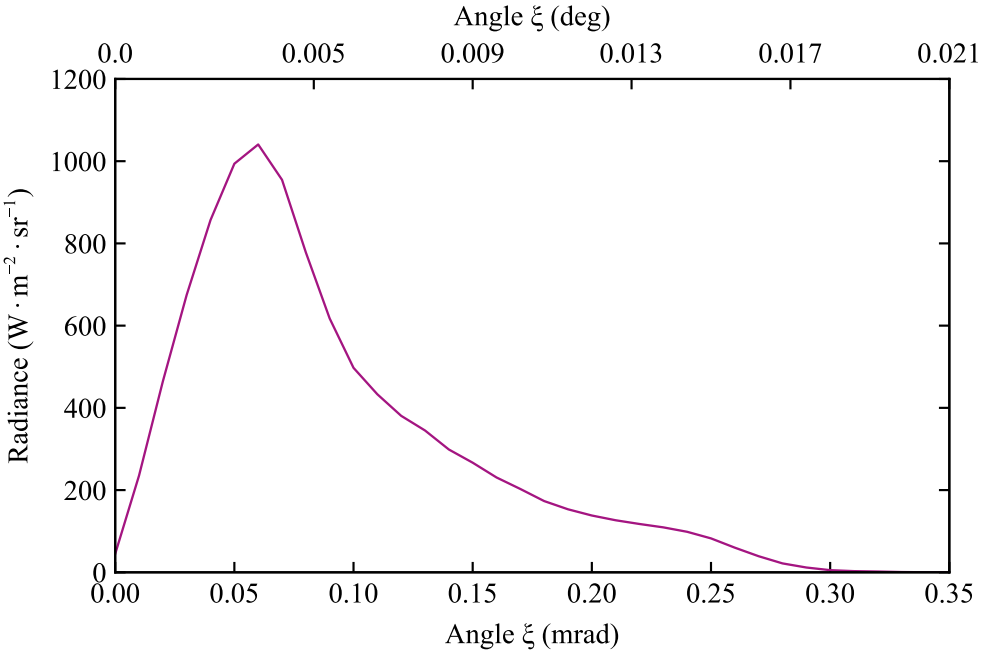


**(b)**

**Figure 3.15.** Radiance and irradiance received by the detector placed at the lens back focus in the divergent-beam simulation. (a) Irradiance in position space, and (b) radiance as a function of the azimuthal angle with respect to the local $z$-axis.

## 3.5 Aspheric telephoto lens

In order to further reduce the image diameter, a second optics was added to the preceding model to form a telephoto lens. This construction has the advantage of having a long focal length, a short overall design, and a lower wavefront aberration. The optimisation of the model resulted in a system (Fig. 3.16) consisting of two aspheric lenses placed, respectively, 11.8 and 88.6 mm after the mirror focus. The sag of the fist lens is defined by the parameters: $R_1 = 10.207$ mm, $K_1 = -8.392$, $R_2 = 30.315$ mm, and $K_2 = -0.450$. Its edge thickness is 5.0 mm, the outside diameter is 13.4 mm, and the front and rear clear apertures are, respectively, 12.8 and 13.4 mm. The second lens has an edge thickness of 50.1 mm, an outside diameter of 70.0 mm, a front clear aperture of 70.0 mm, and a rear clear aperture of 55.0 mm. The parameters of the quadric surfaces are: $R_1 = 2476.748$ mm, $K_1 = 324.836$, $R_2 = -43.135$ mm, and $K_2 = -0.747$.

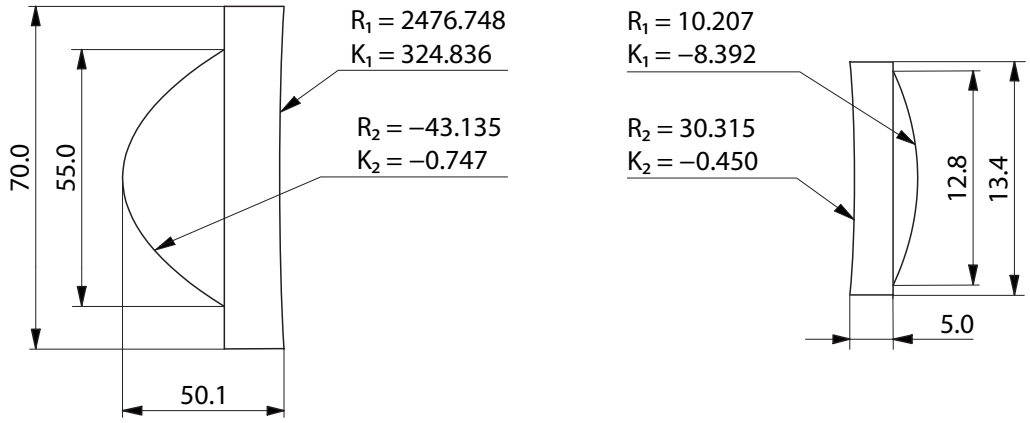


**Figure 3.16.** Schematic of the optimised aspheric telephoto lens (not in scale). All dimensions are expressed in mm.

The image formed by the rays focused by the lens (Fig. 3.17a) is approximately a circle of diameter $6.4 \pm 0.4$ mm showing a slight blur at the edges. The maximum angle of the rays hitting the detector surface is $\sim 6°$, meaning that the lens is able to significantly reduce the aperture angle of the light beam. By comparing these results with those reported for the single-lens design, we find that the lens ensures a better focusing in terms of both image size and incidence angle. The transmitted radiant flux is comparable with that of this latter optics, and is also similar to that calculated for the 0.50-NA fibre bundle.

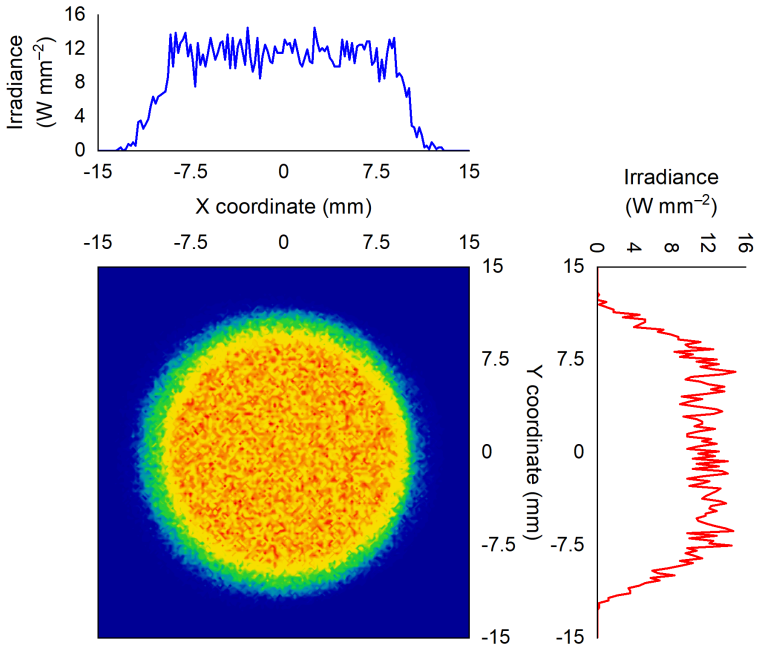


**(a)**

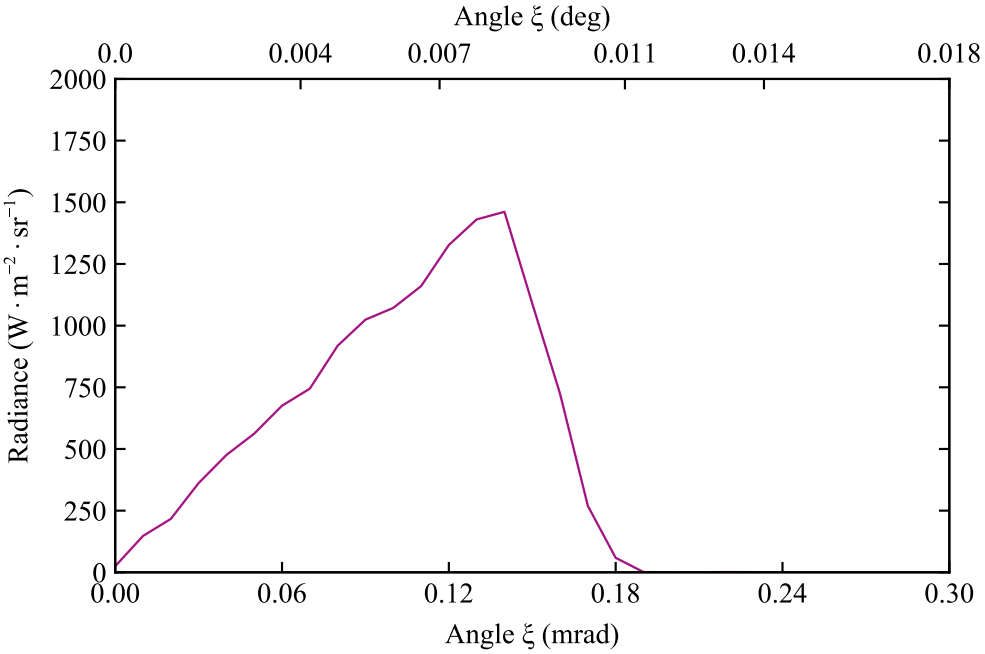


**(b)**

**Figure 3.17.** Radiance and irradiance received by the detector placed at the telephoto lens back focus. (a) Irradiance in position space, and (b) radiance as a function of the azimuthal angle with respect to the local $z$-axis.

## 3.6 Technical analysis of the models

**Table 3.1.** Overview of the optical performance for the simulated models.

| Optical element | Input flux (W) | Output flux (W) | Image diameter (mm) | Maximum angle |
|---|---|---|---|---|
| Light source | – | 1000.0 | – | 0.29° |
| Parabolic concentrator | 200.0 | 191.6 | 5.0 | 32° |
| ITP | 191.6 | 154.5 | 10.0 | – |
| Bare fibre (0.22 NA) | 191.6 | 0.04 | – | 13° |
| Bare fibre (0.39 NA) | 191.6 | 0.33 | – | 23° |
| Bare fibre (0.50 NA) | 191.6 | 0.90 | – | 30° |
| Fibre bundle | 191.6 | 135.0 | – | 30° |
| End-capped fibre | 191.6 | 62.5 | 3.0 | 90° |
| Aspheric lens | 191.6 | 122.4 | 13.2 | 18° |
| Telephoto lens | 191.6 | 143.4 | 6.4 | 6° |

The results obtained from the simulations clearly show that the concentrator–fibre coupling is not an easy task and its efficiency depends on the secondary optics used to inject the beam into the OF. From the parameter overview reported in Table 3.1 it results that the least-performing optics is the end-capped fibre with a transmitted flux of only 62.5 W. This value is clearly not sufficient to guarantee the functionality of MJ cells and for this reason it is not suitable for hybrid systems. The other three optics, *i.e.* the fibre bundle, the aspheric lens, and the aspheric telephoto lens, show similar output fluxes but feature different spatial and angular distributions of the transmitted rays. The image produced by the aspheric lens has a diameter of 13.2 mm which should be collect by a very thick OF bundle placed at its focus. This would imply a high manufacturing cost and, very likely, a high light loss at the air–glass interface. The telephoto lens has a good demagnification power which allows to obtain an image of 6.4 mm that can be collected by a relatively thin fibre bundle. The use of a complex optics, however, may represent a drawback since aspheric lenses should be specifically designed and manufactured to meet the requirements of the DL/HCPV modules at non-competitive costs.

The most straightforward solution to our problem is the use of a fibre bundle. From the simulations, it is proven that the energetic flux is high enough to guarantee a high-efficient system and, in addiction, it is relatively easy to realise from common, commercially available OFs. Moreover, its use would not require any ad-

ditional optics to transport sunlight indoors and the costs would remain limited to that of the fibres used.

# Chapter 4

# The effect of concentrated light on optical fibres

As discussed in detail in the introduction, the two fundamental requisites for the development of an hybrid DL/HCPV module are (i) the optical coupling between the concentrator and the optical fibres, and (ii) the resistance of these latter to concentrated sunlight. The first issue has been addressed in Chapter 3 with the conclusion that a bundle of bare fibres is the best choice to deliver sunlight inside a building. In this chapter we deal with the second aspect, that is finding the optical fibres showing maximum transparency and stability under 2000$\times$ concentrated sunlight. The tests reported were conducted by exposing various prototypical and commercial OFs to different monochromatic lasers and broadband light sources. In the first set of measurements, the selected OFs were exposed to a high-power broadband light source emitting radiation in the UV-to-IR wavelength region. The spectrum of this source is similar to the AM1.5D solar spectrum but its spectral irradiance is $\sim$1000 times greater than that of the Sun. This means that the results obtained from these experiments are similar to those expected from installing the selected fibres at the focus of the HCPV concentrator. The second and third group of tests were carried out using monochromatic light in the Vis–IR and UV domains, respectively. The importance of these tests is that they allowed us to evaluate the damaging threshold of the OFs and helped us understanding the advantages and drawbacks of using optical fibres in HCPV technologies.

## 4.1 Exposure to full-spectrum radiation

The experiments were carried out injecting a broadband Xenon-plasma laser-driven light source (LDLS) directly into the tested fibre and acquiring the *on-line* transmitted spectrum as explained in Section 3.3. The studied samples were either prototypical or commercial fibres made from different glasses having specific optical properties and chemical composition. The first three samples (Fib1, Fib2, and Fib3) were Al-, P-, and Ge-doped silica core, pure-silica cladding optical fibres, the fourth sample (Fib4) was a pure-silica core fibre with a fluorine-doped cladding whereas the fifth (Fib5) one was a low-OH pure-silica core fibre with a hard-polymer cladding. Due to the different core diameter, the injected irradiance varies from sample to sample as reported in Table 4.1. The length used in all tests were 20 cm for doped-core fibres and 2 m for pure-silica core fibres. Further details can be found in Section 3.2.

**Table 4.1.** Relevant properties of the tested optical fibres and irradiance injected into them.

| Sample | Core/Cladding composition | Core diameter (µm) | Injected irradiance ($W \cdot mm^{-2}$) |
|---|---|---|---|
| Fib1 | $SiO_2$:$Al_2O_3$/$SiO_2$ | 62.5 | 1600 |
| Fib2 | $SiO_2$:$P_2O_5$/$SiO_2$ | 62.5 | 1600 |
| Fib3 | $SiO_2$:$GeO_2$/$SiO_2$ | 8.2 | 400 |
| Fib4 | $SiO_2$/$SiO_2$:SiF | 62.5 | 1600 |
| Fib5 | $SiO_2$/Hard polymer | 200 | 2200 |

### Aluminium-doped fibres

The light exposure of Fib1 was performed at an injected flux density of 1600 $W \cdot mm^{-2}$ for 4 h. The recorded transmission spectra are illustrated in the top panel of Fig. 4.1 using a gradient colour map to visualise how the signal intensity changes with exposure time. Although the transmitted signal clearly decreases as the photoinduced damages accumulate, the nature and extent of modifications in the silica matrix are not appreciable. For this reason each transmission spectrum was transformed into an *on-line* radiation-induced attenuation (RIA) spectrum by applying Eq. (1.17) rewritten as follows:

$$\mathrm{RIA} = -\frac{10}{l}\log\frac{I}{I_0}.$$

Here $l$ is the length of the fibre sample, $I_0$ is the transmission spectrum before ir-

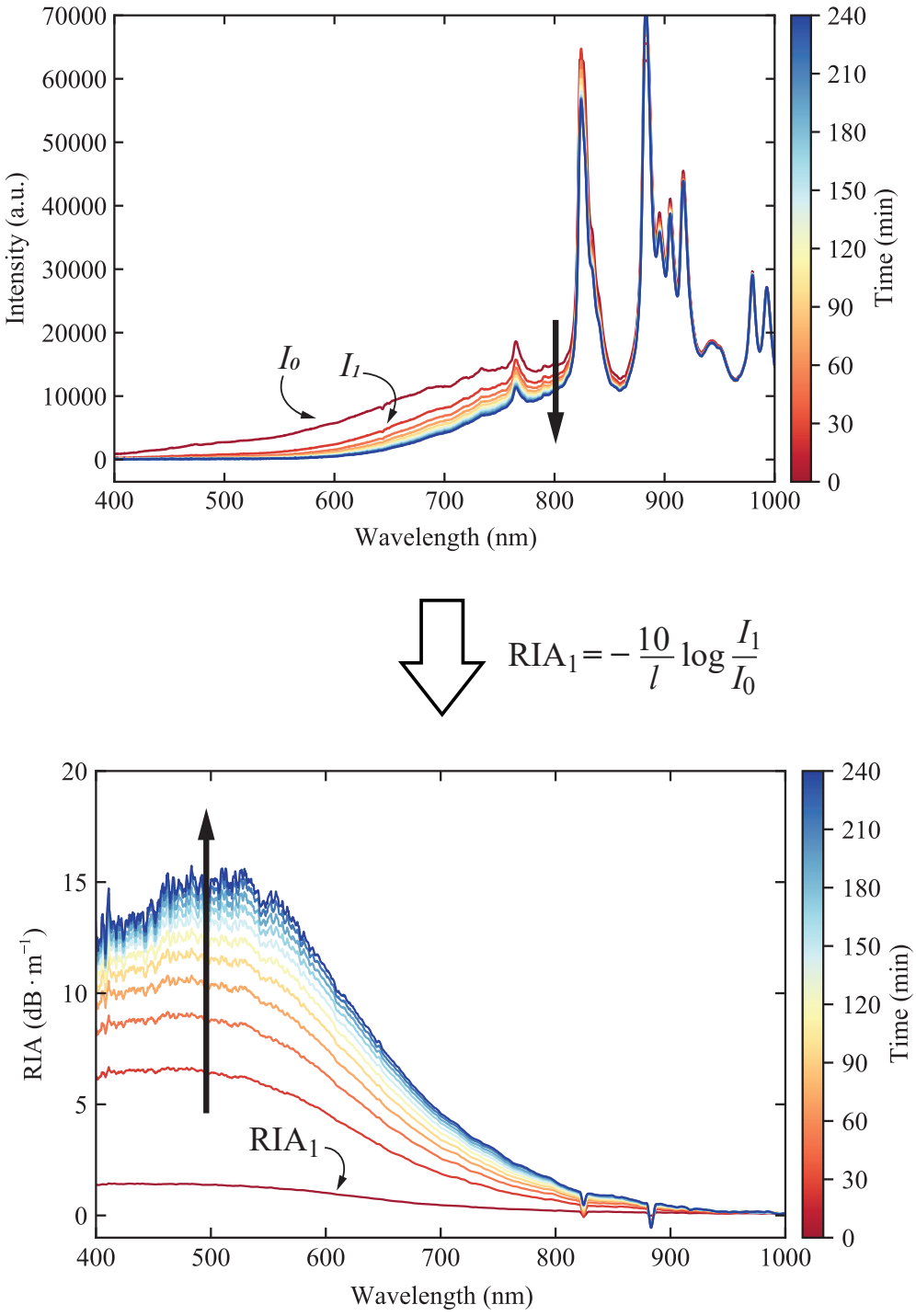


**Figure 4.1.** Transmission spectra (top panel) and induced-attenuation spectra (bottom panel) for the Al-doped silica core, pure-silica cladding optical fibre (Fib1). The colour map indicates the elapsed time and the black arrows indicate the progression of the spectra. By applying the displayed formula, the first and second transmission spectra (respectively, $I_0$ and $I_1$) are transformed into the first RIA spectrum ($\mathrm{RIA}_1$).

radiation, and $I$ is the spectrum measured at a given exposure time. To stick with the "radiometric" notation introduced in Section 1.5, the RIA function corresponds to $\alpha(\lambda)$ while the light intensity measured by the spectrometer corresponds to the (rescaled) radiant flux hitting the detector at the time $t$, that is $I_0 \equiv \Phi(\lambda,0)$ and $I \equiv \Phi(\lambda,t)$. The resulting spectra shown in the bottom panel of Fig. 4.1 indicate that most of the absorption occurs in the visible spectral range while the IR domain is virtually unaffected with a RIA $< 1\,\mathrm{dB}\cdot\mathrm{m}^{-1}$. No information are provided for wavelengths lower than 400 nm since alluminosilicate fibres are not able to guide light in this spectral range.

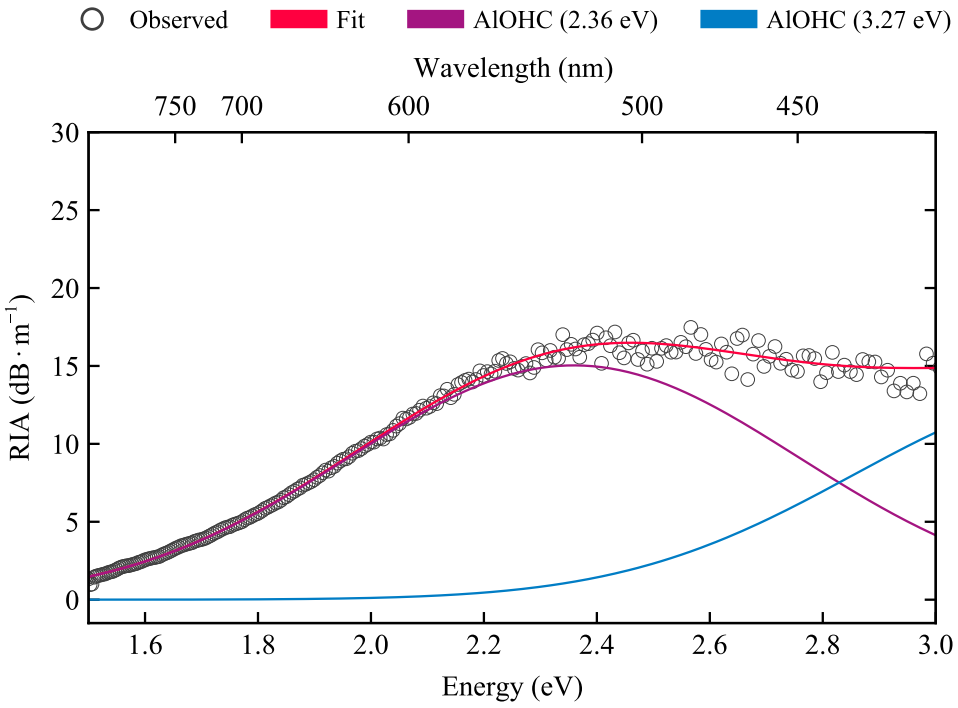


**Figure 4.2.** Gaussian decomposition of the RIA spectrum of the Al-doped silica core, pure-silica cladding optical fibre (Fib1).

To shed light into the microscopical phenomena behind the observed light loss we transformed the $x$-axis units from wavelength to energy and performed a Gaussian decomposition on the last RIA spectrum (*i.e.* the one recorded after 4 h of irradiation). Figure 4.2 shows that the attenuation profile can be fitted by the convolution of a band peaked at 2.36 eV (FWHM = 0.9 eV) and the tail of a second band peaked outside the reported spectral range (3.27 eV, FWHM = 1.0 eV). Both curves are associated with the creation of aluminium-oxygen hole centres (AlOHCs) [226] that are point defects consisting of Al atoms bonded to four bridging oxygen atoms, one of which hosting an unpaired electron ($\equiv$Al$-$O$^{\bullet}-$Si$\equiv$). The origin of the two absorption bands has been discussed in Section 2.3 and is related to two different HOMO $\longrightarrow$ SOMO transitions. Since their effect spans from 1.5 to 4.3 eV (that is,

from approximately 290 to 830 nm), most of the injected visible light is absorbed by the defects and the transmission properties of the OF are largely compromised.

## Phosphorus-doped fibres

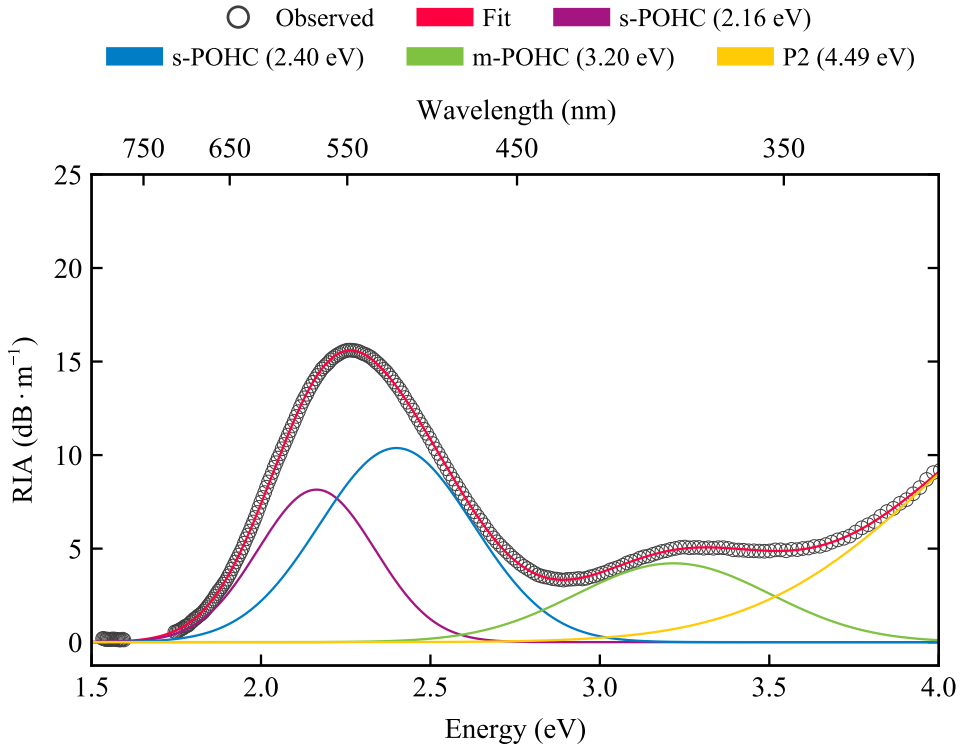


**Figure 4.3.** Gaussian decomposition of the RIA spectrum of the P-doped silica core, pure-silica cladding optical fibre (Fib2).

By exposing Fib2 to the LDLS for 4 h we obtained the RIA spectrum reported in Fig. 4.3. Its Gaussian decomposition allowed us to identify three absorption bands associated to phosphorus-oxygen hole centres (POHCs) peaked at 2.16 eV (FWHM = 0.4 eV), 2.40 eV (FWHM = 0.5 eV), and 3.20 eV (FWHM = 0.7 eV). The first two bands are related to the stable (s) form of the defect whereas the other is attributed to the metastable (m) variant. Although m-POHCs are generally thought to exist only at low temperature, our results suggest that they can be detected at room temperature, in accordance with the findings of Origlio *et al.* [227] and Di Francesca *et al.* [228]. The increasing trend characterising the right-hand side of the spectrum is due to the formation of the defect called P2 centre whose structure can be written as $=P^{\bullet}=$. Its absorption band is centred outside the spectral range (4.49 eV, FWHM = 1.2 eV) but the tail extends up to $\sim$3 eV and strongly contributes to the measured attenuation spectrum. The highest RIA observed for this fibre is equal to $\sim 16\,\mathrm{dB \cdot m^{-1}}$ and is given by the convolution of the two s-POHC bands.

At higher energies, the attenuation is 4 to 9 $\mathrm{dB \cdot m^{-1}}$, which is still too high for the purpose of guiding sunlight.

## Germanium-doped fibres

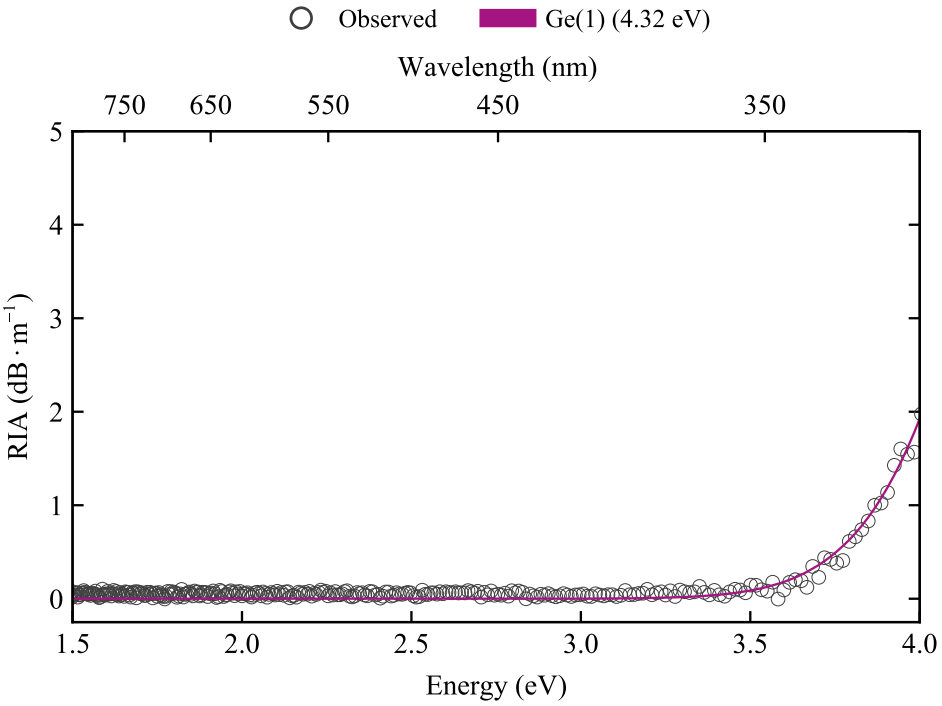


**Figure 4.4.** Gaussian decomposition of the RIA spectrum measured at the end of the 4-h light exposure of the Ge-doped silica core, pure-silica cladding optical fibre (Fib3).

Figure 4.4 shows the RIA spectrum obtained at the end of the 4-h irradiation of Fib3. Contrarily to what observed for other doped samples, the transmission of this fibre remains unaltered in the visible domain and features only a small decrease (about 2 $\mathrm{dB \cdot m^{-1}}$) at the high-energy extreme of the spectrum. This behaviour is caused by the presence of an absorption band peaked at 4.32 eV (FWHM = 1.0 eV) attributed to Ge(1) defects as explained in Section 2.3. Since this band is located in the UV domain, it has no contribution at energies lower than 3.5 eV. This means that light with wavelengths longer than 350 nm is transmitted by the fibre without any significant loss.

From the above results, it is clear that only one of the three doped fibres is suitable for applications requiring resistance and transparency to concentrated light. In fact, the LDLS light caused the degradation of Fib1 and Fib2 in the UV–Vis domain but did not cause any solarisation effects in Fib3. Since sunlight has a strong visible component, the use of Al- and P-doped fibres should be avoided to guide it for

daylighting and photovoltaic applications. The only photo-induced effect measured in Fib1 is the creation of Ge(1) centres. This defect, however, does not affect the transmission of light in the Vis domain for its band is centred at 4.32 eV (287 nm). The high resistance to concentrated light, together with the wide availability on the market at a low price, makes of Ge-doped fibres a suitable choice for solar energy applications.

## Pure-silica core fibres

The pure-silica core samples Fib4 and Fib5 were irradiated with the LDLS for 4 h with the resultsa shown in Fig. 4.5. As indicated by the RIA spectrum, Fib4 resisted to concentrated light maintaining its transmission properties unaltered. This was somewhat expected since Fib4 is a solarisation-resistant fibre and its glass matrix is sensible only to radiation more energetic than UV light. The attenuation at energies greater than 3 eV is an artefact related to the lower signal-to-noise ratio characterising this spectral region. To validate this finding, we performed a second test by using a 20-m sample of Fib4 and exposing it to the LDLS for a total of 24 h. The experiment was split in three phases which can be summarised as: 12 h of irradiation, 12 h of recovery, and 12 more hours of irradiation. The recovery of the signal was monitored using a non-degrading light source injected into the fibre instead of the LDLS. This test was designed to see the OF's behaviour in the harshest conditions achievable in our laboratory. Since the fibres installed in the hybrid HCPV system will be subject to 12 h of light and 12 h of darkness, it was of paramount importance to test the fibre alternating periods of irradiation and periods of recovery. Even in this case, the fibre proved to resist to the radiation and no absorption signal was detected (Fig. 4.6).

Contrarily to the outcome obtained for Fib4, the standard 4-hour light exposure of Fib5 (Fig. 4.5) resulted in an increasing RIA profile with a very small hump around 3 eV. The observed attenuation is not related to any known defects of *a*-$SiO_2$ and is difficult to fit with simple Gaussian functions. We tentatively assigned this behaviour to the presence of chlorine impurities trapped in the silica matrix during the manufacturing process. In fact, $Cl_2$ is commonly used to remove Si–OH groups in low-OH "dry" silica glasses [229–231]. If the resulting glass is not properly treated, chlorine can get stuck as interstitial $Cl_2$ or $Cl^0$ in the *a*-$SiO_2$ matrix and its presence is detected even in "pure silica" OFs. In particular, monatomic $Cl^0$ has an OA band peaked near the observed hump (3.26 eV, FWHM = 1.2 eV) and may be at the origin of the observed RIA profile [231, 232]. As an alternative, the signal loss could be interpreted as determined by the light-induced degradation of the polymeric cladding of Fib5, as often observed in $\gamma$- and X-ray-treated polymeric OFs. In this case, the absorption of high-energy photons determines a change in the cladding chemical structure which, in turns, leads to an increase in its refractive

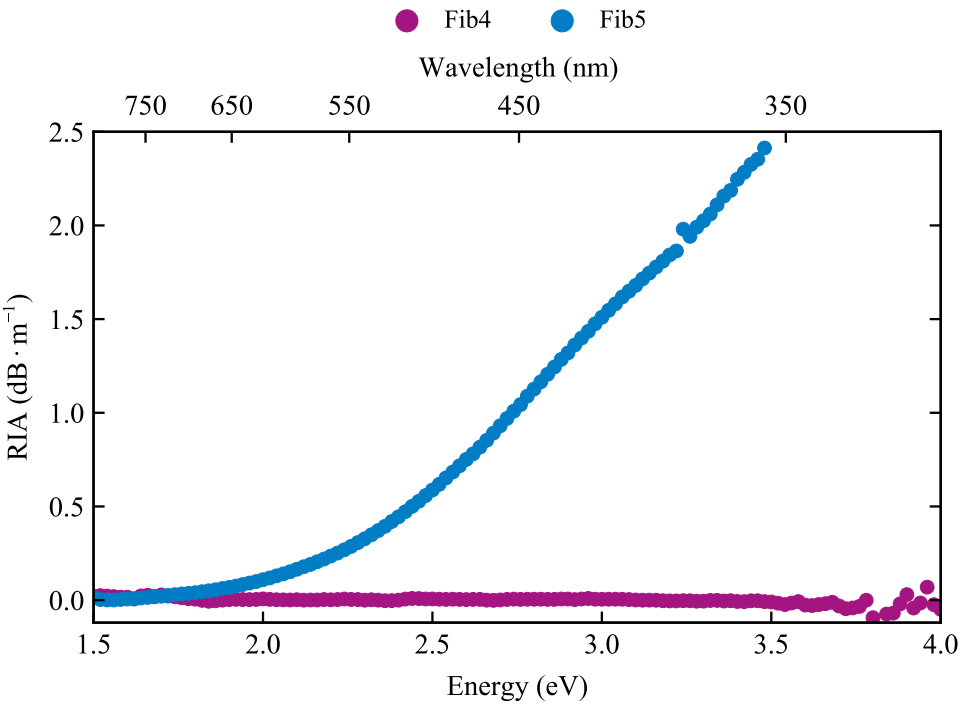


**Figure 4.5.** RIA spectrum measured at the end of the 4-h light exposure for the pure-silica core, F-doped silica cladding (Fib4) and pure-silica core, hard-polymer cladding (Fib5) optical fibres.

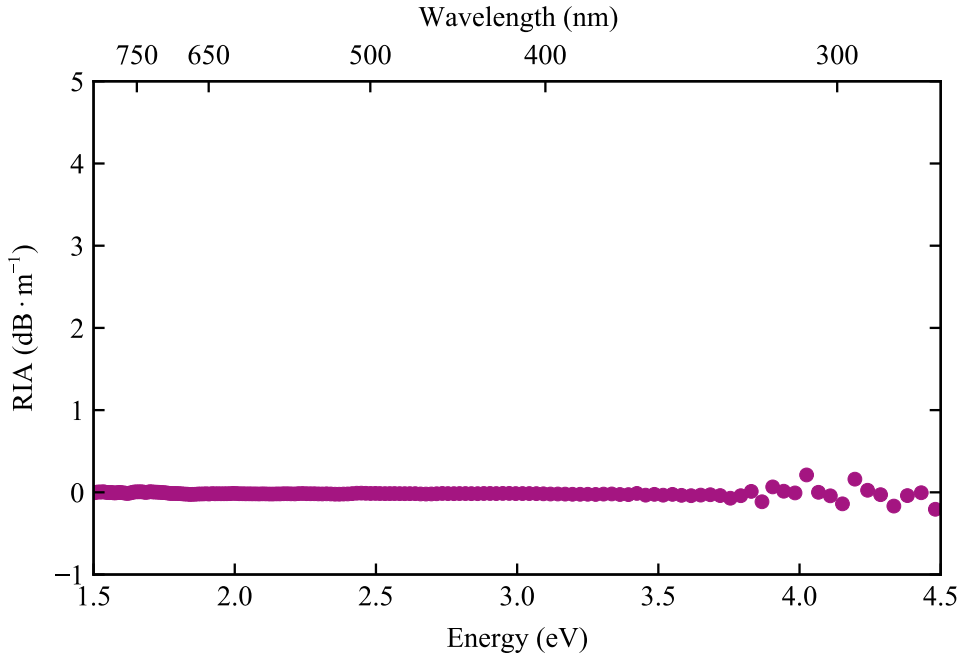


**Figure 4.6.** RIA spectra measured after a 2 days/1 night exposure cycle for the pure-silica core, F-doped silica cladding optical fibre (Fib4).

index. By changing the core–cladding index mismatch, the guiding properties of the OF are decreased and the light is lost before arriving to the detector. In either case, the attenuation ($2.5\,\mathrm{dB}\cdot\mathrm{m}^{-1}$) is small compared to that of Al- and P-doped OFs and for this reason these waveguides could still be employed for solar technologies. This aspect should be deepened to clarify the origin of the observed band and to confirm or exclude the possibility of integrating this fibre in daylighting systems.

## Overall analysis

From the above results, it is clear that the solarisation of optical fibre is a serious issue when working with concentrated light. The exposure of Al- and P-doped fibres resulted in the formation of extensive RIA bands across the spectral domain of interest, demonstrating their high sensibility to radiation. Ge-doped OFs showed some solarisation phenomena but the observed attenuation band is located in the UV domain and has no effect on Vis and IR light. Fib4 proved to resist to extreme irradiation condition without any photodarkening while Fib5 showed an unexpected behaviour, probably related to the polymeric nature of its cladding. To have a clearer picture of the effect of the LDLS on all the tested samples, we can look at the attenuation profiles as a function of the exposure time. The kinetics at 550 nm reported in Fig. 4.7 indicate that Fib1 and Fib2 are affected by a very quick photodarkening which determines the loss of almost 37% of the injected light (*i.e.* $\sim 2\,\mathrm{dB}\cdot\mathrm{m}^{-1}$) within the first 5 min of irradiation. The RIA level of Fib4 can be considered negligible ($\sim 0.1\,\mathrm{dB}\cdot\mathrm{m}^{-1}$), whereas that of Fib3 and Fib5 reaches, respectively, $0.5\,\mathrm{dB}\cdot\mathrm{m}^{-1}$ and $1.0\,\mathrm{dB}\cdot\mathrm{m}^{-1}$ by the end of the experiment. The onset of the absorption in these latter samples occurs at different times, indicating that the underlying solarisation processes are different and that Fib3 has a period of latency of about 1.5 h in which the concentration of Ge(1) centres is so low that it does not affect Vis-light transmission. The above reported results allow to carry out some main conclusion about the use of the investigated fibres in the HCPV

From the above results we can state that aluminium- and phosphorus-doped silica core fibres undergo a rapid solarisation process when exposed to concentrated broadband light. This considerably reduces their transmission efficiency in the Vis–IR spectral domain, accounting for a maximum attenuation of $\sim 17\,\mathrm{dB}\cdot\mathrm{m}^{-1}$. The germanium-doped silica core fibres show the onset of an attenuation band which causes UV-light loss but does not modify their guiding properties in the Vis–IR portion of the spectrum. Pure-silica core/hard-polymer cladding fibres show an unknown absorption band which accounts for a RIA of about $1\,\mathrm{dB}\cdot\mathrm{m}^{-1}$ in the Vis range. Pure-silica core/F-doped silica cladding fibres demonstrated to resist to concentrated light even after 48 h of irradiation. As a first choice, we thus ruled out Fib1 and Fib2 as possible waveguides for our hybrid module and continued testing only Fib3, Fib4, and Fib5.

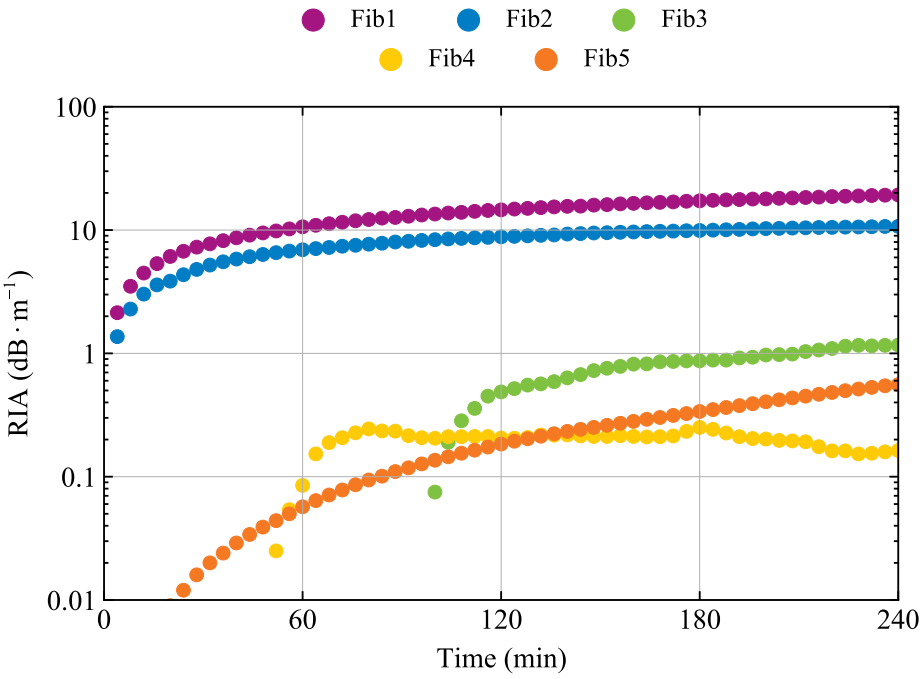


**Figure 4.7.** RIA kinetics at 550 nm for all the tested fibres.

## 4.2 Exposure to Vis–IR radiation

**Table 4.2.** Relevant properties of the pigtailed diode lasers and comparison of their power with that of the Sun at the same wavelength. The power factor is calculated as the ratio of the laser output power to the global solar irradiance.

| Laser ID | Peak energy (eV) | Laser irradiance ($\mathrm{W \cdot mm^{-2}}$) | Global solar irradiance ($\mathrm{W \cdot mm^{-2}}$) | Power factor |
|---|---|---|---|---|
| LP405-MF300 | 3.06 | 120 | $1.15 \times 10^{-6}$ | $1.04 \times 10^{8}$ |
| LP520-SF15 | 2.38 | 1667 | $1.52 \times 10^{-6}$ | $1.09 \times 10^{9}$ |
| LP660-SF60 | 1.88 | 3750 | $1.40 \times 10^{-6}$ | $2.68 \times 10^{9}$ |
| LP785-SF100 | 1.58 | 4000 | $1.16 \times 10^{-6}$ | $3.45 \times 10^{9}$ |
| LPS1060-FC | 1.17 | 1389 | $6.36 \times 10^{-7}$ | $2.18 \times 10^{9}$ |

The effects of visible and infrared light on optical fibres were investigated using a series of multimode pigtailed laser diodes emitting different wavelengths. As the irradiance and spectral distribution of the injected light are extremely sensible to the laser–fibre coupling, the *online* RIA measurement was performed using the splicing method described in Section 3.3. The flux densities emitted by the lasers

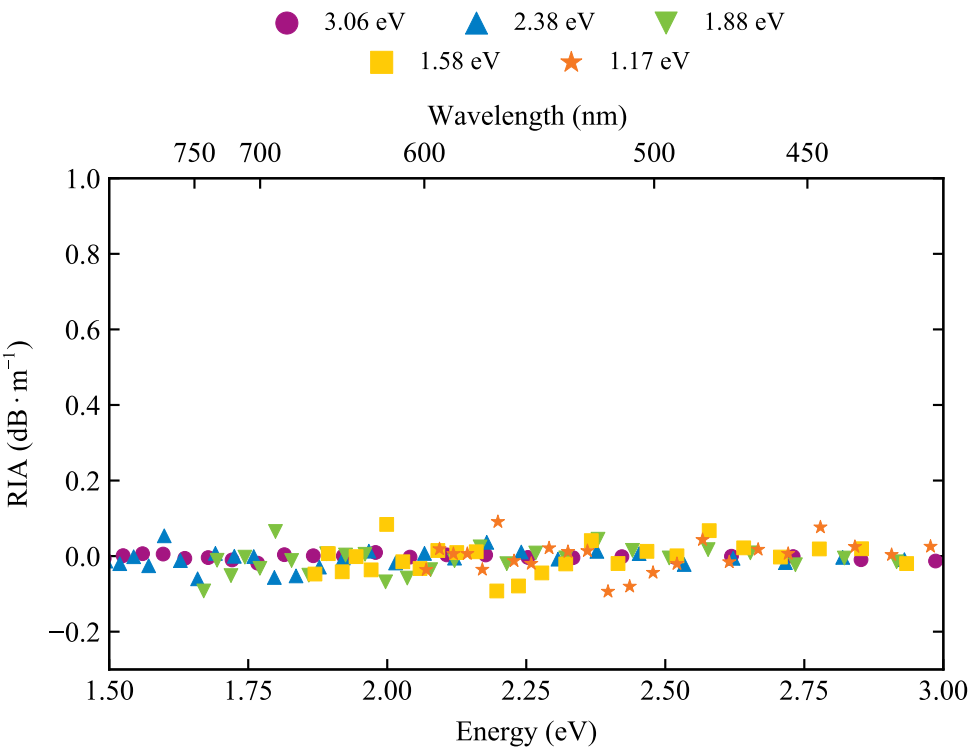


**Figure 4.8.** RIA spectra for the pure-silica core, hard-polymer cladding fibre (Fib5) obtained after a 4-h irradiation with the pigtailed laser diodes.

are reported in Table 4.2 together with the global solar irradiance at the laser peak wavelength and the power factor. The latter is calculated as the ratio of the laser to the solar irradiance and indicates how much powerful the diode is compared to the Sun. The fibres tested at this stage are the Ge-doped and the pure-silica ones as explained in the previous section.

Figure 4.8 shows the RIA spectra for the pure-silica core, hard-polymer cladding fibre (Fib5) after a 4-h irradiation with the available laser diodes. Despite the very high irradiance, all the RIA signals are fairly flat, indicating that the silica matrix did not suffer any photo-induced damages. The small fluctuations characterising the spectra are due to either a slight instability of the light source or the low signal-to-noise ratio typical of low-attenuation measurements. The RIA spectra of Fib3 and Fib4 (not reported) are similar to those shown in Fig. 4.8 and demonstrate that the diode irradiation did not cause any appreciable modifications in the fibre transmission properties.

To study the response of the OFs to higher flux densities, we exposed the OFs to the second harmonics (2.33 eV, 532 nm) of a Nd:YAG laser for 4 h. The pulsed waves were injected into the fibre by means of a relay lens as described in Section 3.3. The power delivered by each pulse is 600 mW and the flux density absorbed by the sample is $6\,\mathrm{W}\cdot\mathrm{mm}^{-2}$. Due to the small core diameter, the light

injection into Fib3 and Fib4 was not efficient. Fib5, on the contrary, showed a degradation effect as demonstrated by RIA spectrum in Fig. 4.9. Clearly, the spectrum does not feature any absorption bands but is constant at a value of $\sim 220\,\mathrm{dB}\cdot\mathrm{m}^{-1}$. This suggests that the underlying damaging effect is not related to the formation of new point defects but rather has a mechanical nature. In fact, by observing the fibre with an optical microscope, we found that its end-face surface showed evident cracks and fractures as shown in Fig. 4.10. The irregular fibre tip determined a sub-optimal injection of the probe light into the OF and this, in turn, led to the observed signal loss. By reducing the pulse energy and repetition rate we managed to inject the laser light into Fib5 without causing its breaking. The resulting RIA spectrum, however, did not show any absorption band. From this observations and the results of the diode-laser tests, we can affirm that visible light does not induce any solarisation effect on Ge-doped and pure silica fibres.

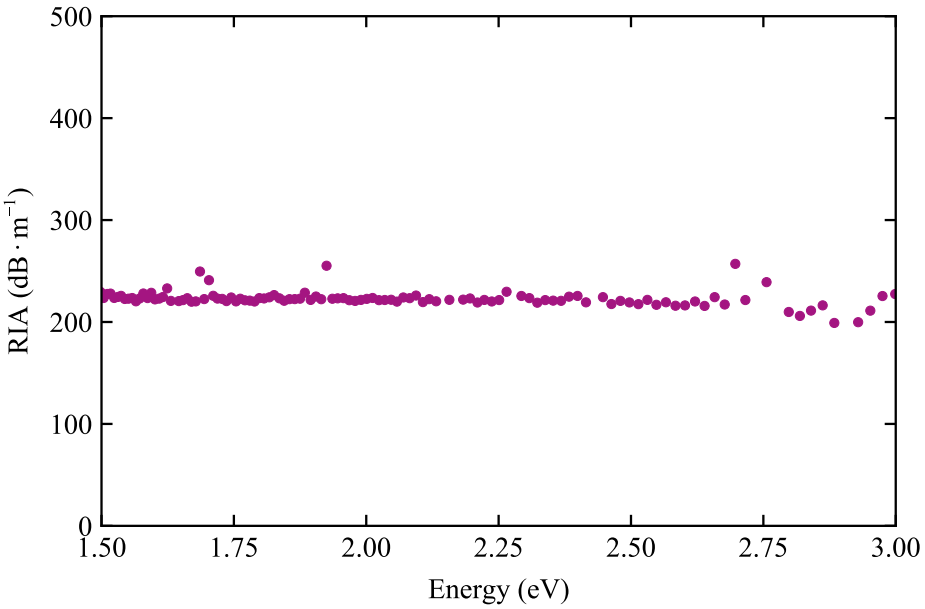


**Figure 4.9.** RIA spectrum for Fib5 obtained after a 4-h irradiation with the second harmonics (2.33 eV, 532 nm) of a Nd:YAG pulsed laser.

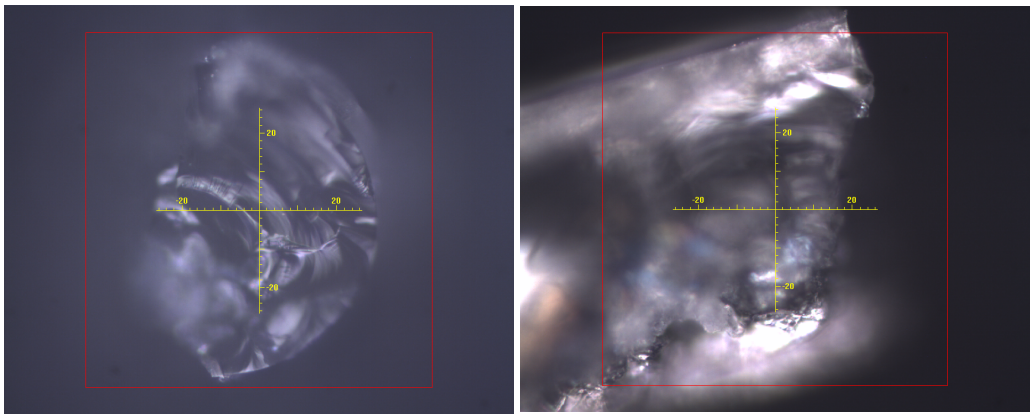

**(a)** **(b)**

**Figure 4.10.** Fracturing induced by the Nd:YAG laser on Fib5. (a) Top view and (b) side view.

## 4.3 Exposure to UV radiation

To study the response of the optical fibres to high-energy light, we irradiated Fib3, Fib4, and Fib5 using the third harmonic (3.49 eV, 355 nm) of a Nd:YAG laser. The pulse power and repetition rate were set to 100 mW and 6 Hz, respectively, in order to avoid any damages of the fibre end face. As in the previous case, Fib3 and Fib4 resulted too thin to guarantee a reproducible injection of light. For this reason no information regarding the UV light-induced damage of these fibres is available. Conversely, the absorption of light by Fib5 ($E = 600\,\mathrm{W \cdot mm^{-2}}$) resulted in the RIA spectrum shown in Fig. 4.11a. The maximum attenuation level in the explored range is $\sim 4\,\mathrm{dB \cdot m^{-1}}$, which means that approximately 40% of the injected light is absorbed before reaching the end face of a 1-m long fibre. The absorption, however, is fully contained in the UV spectral range and does not interfere with the transmission of Vis and IR light. The Gaussian fitting of the attenuation profile allowed us to identify the tail of a band peaked at 5.82 eV (FWHM = 0.88 eV) ascribable to an increase in the concentration of $E'$ centres.

A second test was carried out on Fib5 at a higher pulse energy (350 mW) and pulse rate (7 Hz). The irradiance absorbed in this case is equal to $2450\,\mathrm{W \cdot mm^{-2}}$. As demonstrated by the RIA spectrum in Fig. 4.11b, in this case the formation of $E'$ centres is accompanied by that of non-bridging oxygen hole centres (NBOHCs). The band of the fist defect is again centred at 5.80 eV (FWHM = 0.73 eV) while the second defect is responsible for the band at 4.77 eV (FWHM = 0.90 eV). As explained in Section 2.3, there exist at least two different pathways leading to the photo-induced generation of $E'$ centres. The first is the so-called bond-dissociation

mechanism

$$\equiv\mathrm{Si}-\mathrm{O}-\mathrm{Si}\equiv \xrightarrow{h\nu} \equiv\mathrm{Si}^{\bullet} \quad {}^{\bullet}\mathrm{O}-\mathrm{Si}\equiv$$

which accounts for the formation of a stable $E'$–NBOHC defect pair. The second is the Frenkel-type mechanism represented by

$$\equiv\mathrm{Si}-\mathrm{O}-\mathrm{Si}\equiv \xrightarrow{2h\nu} \equiv\mathrm{Si}^{\bullet} \quad {}^{+}\mathrm{Si}\equiv + e^{-} + \mathrm{O}^{0}.$$

In accordance with the accepted model, our results suggest that the first reaction is favoured at high pulse energies whereas the second prevails at lower energies. Since only NBOHCs absorb in the Vis domain, $2450\,\mathrm{W}\cdot\mathrm{mm}^{-2}$ can be considered the threshold beyond which Fib5 cannot be used to transmit concentrated light for solar devices. This value is equal to a concentration ratio of $2450\times$, which is still above the $2000\times$ achieved by our concentrating photovoltaic module. For this reason we can safely say that Fib5 is suitable for being integrated as a waveguide in our hybrid DL/HCPV module.

The above experiments suggest that the most suitable fibre for high-concentration solar devices is the pure-silica core/F-doped silica cladding one. Its resistance guarantees a lossless transmission of concentrated light and a high durability in terms of performance. Nonetheless, its relatively high cost represents a drawback and may prevent its integration in solar systems. In its place, we could opt for germanium-doped silica core fibres which are less expensive and completely transparent to wavelengths above 350 nm. However, since they are generally used for telecommunication purposes, the core diameter of most commercial fibres is too small to transmit a sufficient amount of light. Pure-silica core/hard-polymer cladding fibres appear to be the best trade-off between performance and costs. The high numerical aperture and bendability are features that may help simplifying the design and reducing the costs of daylighting systems. Furthermore, apart from an unknown effect related to the degradation of the cladding, the transmission properties of these OFs are good enough for a fibre-optics implementation of our HCPV system.

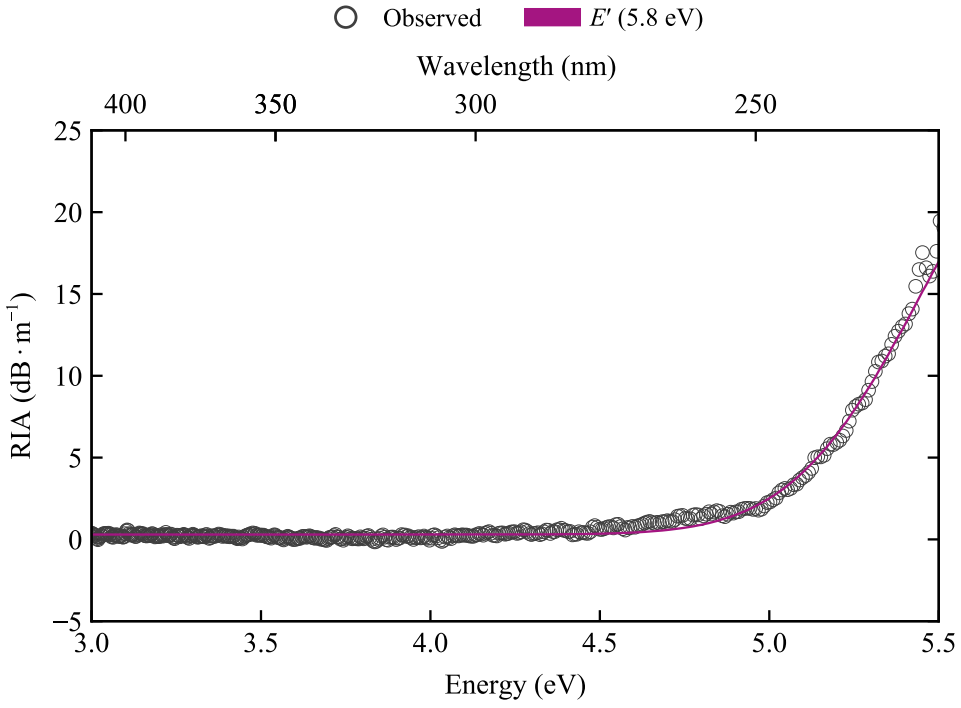


**(a)**

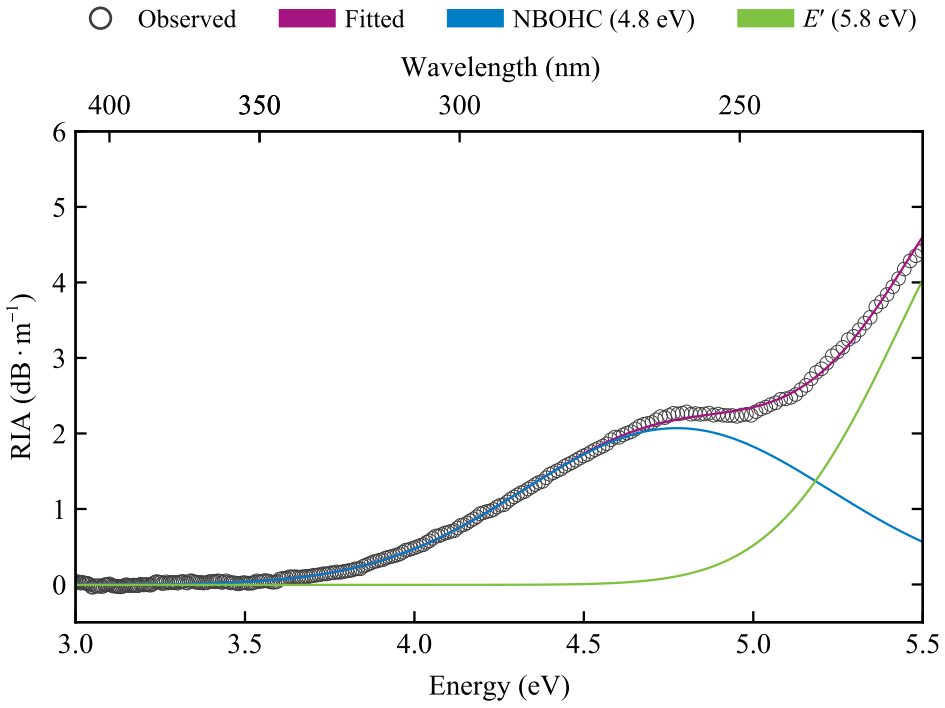


**(b)**

**Figure 4.11.** Gaussian decomposition of the RIA spectra measured after the irradiation of Fib5 with the Nd:YAG laser at a flux density of (a) 600 $W \cdot mm^{-2}$ and (b) 2450 $W \cdot mm^{-2}$.

# Chapter 5

# Proof-of-concept of the hybrid DL/HCPV module

FAE is a very stable HCPV system which is able to produce up to 1 kW of electric power and guarantee a CHP efficiency of more than 80%. During the R&D phase, all the components have been laboratory-tested under harsh conditions to make sure they resisted to 2000× concentrated sunlight. However, field tests proved that both the ITPs and the TJ solar cells are sensible to atmospheric agents and are subject to efficiency loss when exposed to dust, humidity, and non-uniform illumination. In order to prevent the ageing of these components, the receiver may be placed in a controlled environment where parameters like temperature and illumination are more easily controlled.

In this chapter we evaluate the weaknesses of the FAE receiver and present a prototypical DL/HCPV module obtained by implementing one of the FAE modules with optical fibres. The performance of the hybrid module was evaluated by measuring the power generated by the OF-coupled solar cells, as well as by studying the transmission spectra of the mounted fibres.

## 5.1 ITP and solar cell analysis

From the survey of the 50 receivers used in the 6-year activity of the FAE system, both the ITPs and the solar cells showed occasional damage due to the prolonged exposure to adverse weather conditions. Table 5.1 summarises the typology and fre-

quency of occurrence of the observed damages. The mechanical failure of TJ cells is the first cause of receiver malfunctioning (40.5% of the total cases) followed by the ITP bottom face rupture (38.1%). The problem either consists in the detachment of the cells from the circuit board or the formation of microcracks in the absorbing layers. In both cases, the cause is most likely the uncontrolled rise in the heat transfer fluid pressure which determines a bending stress on the back of the cells. Similarly, the fracture of the ITP bottom face can be related to a pressure rise which causes mechanical stress on the contact surface between the ITP and the TJ cell. These issues can be (and actually were) solved by using a control unit to maintain the cooling system pressure constant.

**Table 5.1.** Damage origin and statistics for the FAE receiver components.

| Component | Damage | Percentage |
|---|---|---|
| ITP | Fracturing (upper part) | 14.3% |
| | Fracturing (lower part) | 38.1% |
| TJ cell | Mechanical breaking | 40.5% |
| | Electrical failure | 7.1% |

The other problem affecting the TJ cells, namely the electrical failure, consists in the damaging of one or more subcells which leads to a reduction in the device photoconversion efficiency. This phenomenon is caused by the non-uniform illumination of the cell which occurs when the system moves from a defocused to a focused position and vice versa. In fact, the transition between the two positions causes a temporary asymmetric sunlight flux on the cell which induces the generation of superficial currents that can potentially harm its correct functioning. The effect of the damage can be quantified by measuring the current–voltage (*I*–*V*) curve of a partially damaged cell and comparing it with that obtained for a pristine cell. Figure 5.1 shows the *I*–*V* curves obtained for two cells exposed to a DNI of $900\,\mathrm{W}\cdot\mathrm{m}^{-2}$. The three points labelled on each curve are indicators of the device performance. $I_{sc}$ is the short circuit current and correspond to the highest current that can be generated by a given solar cell in short circuit conditions ($V = 0$). $\mathrm{V}_{oc}$ is the open circuit voltage,that is the voltage across the diode when the photocurrent is zero. The maximum power point $P_{MP}(I_{MP}, V_{MP})$ defines the operating conditions at which the power generated by the cell is at its maximum value. For the pristine cell these parameters are $\mathrm{V}_{oc} = 3.30 \pm 0.01$ V, $I_{sc} = 20.12 \pm 0.05$ A, and $P_{MP} = (2.70, 18.63)$ while for the damaged cell they are $\mathrm{V}_{oc} = 3.20 \pm 0.01$ V, $I_{sc} = 7.20 \pm 0.05$ A, and $P_{MP} = (2.57, 6.90)$. By comparing the two sets of data it results that the short circuit current is heavily affected by the damaging of the cell, registering a drop of 64%. If we take the product of the maximum power current and the maximum power

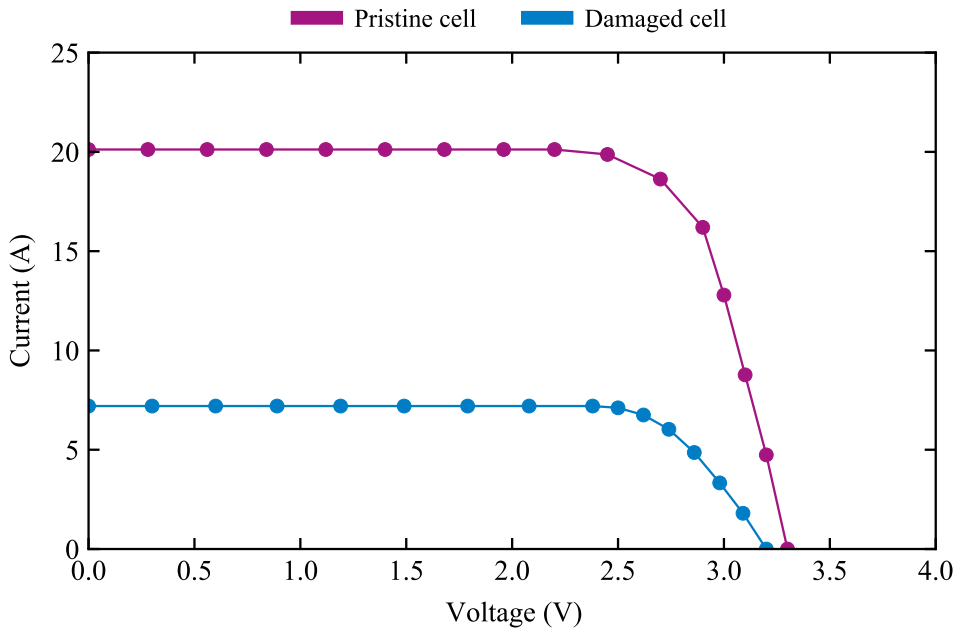


**Figure 5.1.** *I–V* curves for a pristine and a damaged cell measured on the FAE system under 2000× sunlight.

voltage (*i.e.* the coordinates of $P_{MP}$) we find that the power generated by the pristine cell is 50.30 W while that of the damaged cell is 17.73 W. In this case, although the damaged module is still able to produce electricity, its efficiency drops by almost 65% due to the cell malfunctioning.

The problems affecting the ITPs are often observed together with cell breaking, especially the lower-part fracturing. Figures 5.2 and 5.3 show the damages reported for some of the ITPs retired from the FAE system. Two different phenomena are thought to be at the origin of the observed fracturing. The first contribution is the thermal stress generated during the focusing/defocusing cycles of the system. In fact, when the DNI drops abruptly due, for example, to the passage of a cloud, the ITP undergoes a rapid thermal contraction which may lead to the fracturing of the ITP top surface. The second cause is the overheating of the solar cell which results in the generation of additional thermal stress and the fracturing (almost an "explosion") of the ITP bottom face. The implication of the thermal mismatch between the ITP and the cell should be further investigated in order to improve the performance of the FAE system but this aspect is beyond the scopes of this thesis.

During the 6-year activity of the FAE system, a different problem also emerged from a more in-depth analysis of the ITPs, namely their optical degradation. To investigate the consequences of prolonged exposure to concentrated sunlight we compared a pristine and a used ITP by measuring their optical absorption as showed in Fig. 5.9. The spectra indicate that, after years of utilisation, the ITP glass is affected by photodarkening processes which determine an increase in its absorbance.

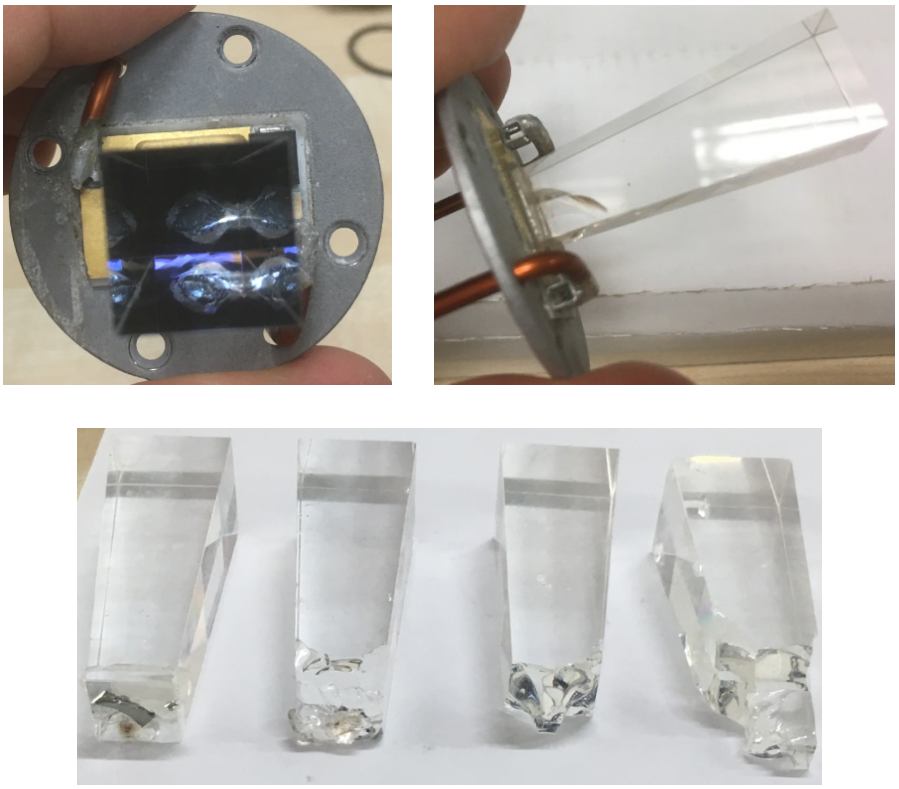

**Figure 5.2.** Mechanically damaged TJ cells and lower-part fractured ITPs removed from the FAE system.

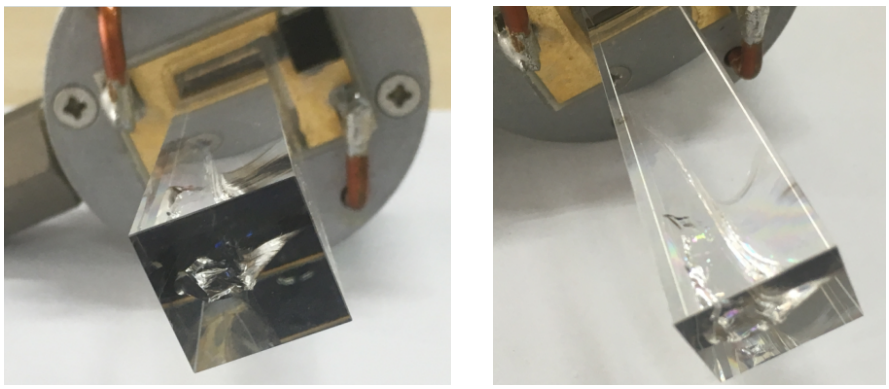

**Figure 5.3.** Upper-part fractured ITPs removed from the FAE system.

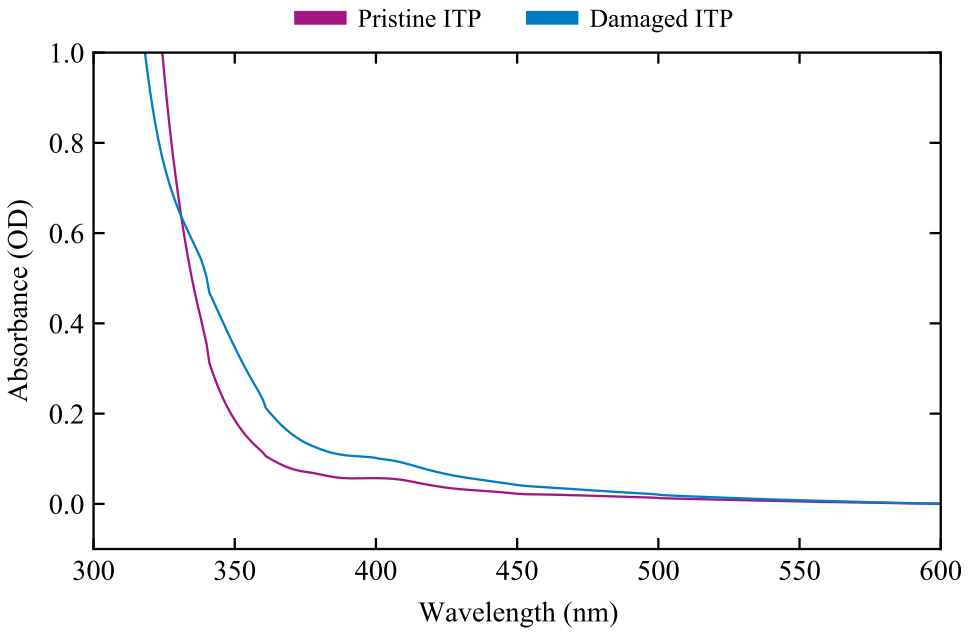


**Figure 5.4.** Absorption spectra for a pristine and a damaged ITP removed from the FAE system.

The effect, however, mainly concerns the UV spectral domain and has minimal implications for the transmission of Vis–IR light. In fact, the absorbance in the 400–600-nm range is less than or equal to 0.1 OD and is mostly determined by light reflection at the ITP entry surface. For this reason the measured absorbance can be considered negligible for all practical applications.

## 5.2 Prototype description

Some of the issues emerged from the above analysis were solved by making minor changes in the FAE system. Others, like the non-uniformity of the transient sunlight beam or the cell overheating, are more difficult to overcome and require a partial redesigning of the collector. As stated before, our aim was to reduce the occurrence of such phenomena by removing the receiver from its position and installing it in a sheltered place. To this end we used fibre optics to guide the light from the concentrator to the receiver and ensure a proper illumination of the cells. The resulting DL/HCPV prototype module is represented in the schematic diagram in Fig. 5.5. Since the diameter of the used fibres is smaller than the mirror focal image, only part of the sunlight reflected by the concentrator was actually injected into the optical fibre. The remaining part was blocked and scattered away by the fibre supporting structure. This is indicated by the dark- and light-blue beams depicted in Fig. 5.5.

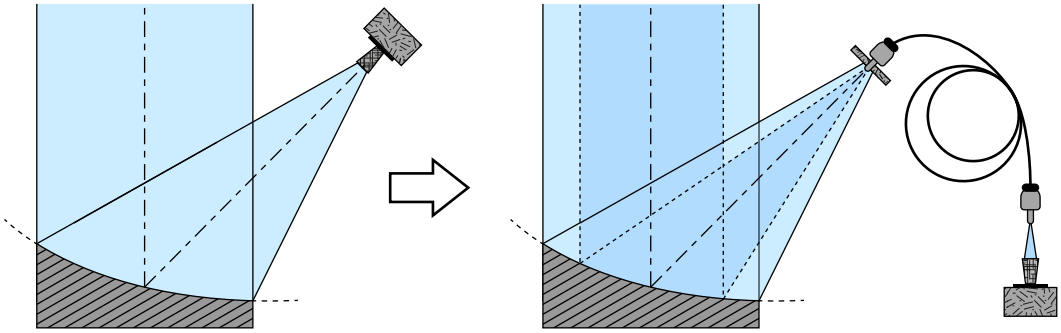

**Figure 5.5.** Schematic of a FAE HCPV module in its original design (left panel) and the hybrid DL/HCPV module after the upgrade with an optical fibre (right panel). The drawings are not in scale.

The optical fibres installed in the hybrid module belong to the three typologies identified as the best candidates in Chapter 4. Three of them (Fib5, Fib6, and Fib7) are pure-silica core, hard-polymer cladding fibres with different diameter and hydroxyl (OH) content. The other two are a Ge-doped silica core fibre (Fib8) and a pure-silica core, F-doped silica cladding fibre (Fib4). More specifications for these fibres can be found in Section 3.2. Each of the selected OFs was installed at the mirror focal point by using a fibre holder and a fibre connector as shown in Fig. 5.6a. The position of the near end was optimised to achieve the best optical coupling with the concentrator and thus the highest light injection. The far end was fixed to an indoor supporting structure and coupled to the underlying solar cell as in Fig. 5.6b.

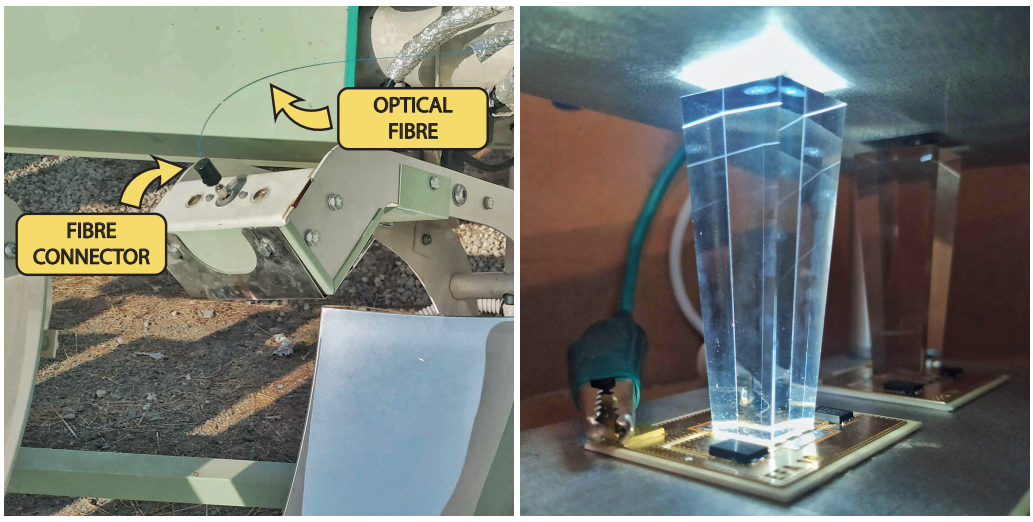


**(a)** **(b)**

**Figure 5.6.** Details of the real hybrid DL/HCPV module showing (a) the fibre coupled to the parabolic concentrator and (b) the indoor module hosting the TJ cells and the attached ITPs.

## 5.3 Transmission properties

**Table 5.2.** Technical details of the fibres mounted on the hybrid system.

| Label | Core/Cladding material | Core diameter (μm) | Transmission range (nm) | NA |
|---|---|---|---|---|
| Fib4 | $SiO_2$/$SiO_2$:SiF | 62.5 | 400–2200 | 0.12 |
| Fib5 | $SiO_2$ (low-OH)/Hard polymer | 200 | 400–2200 | 0.50 |
| Fib6 | $SiO_2$ (high-OH)/Hard polymer | 200 | 300–1200 | 0.50 |
| Fib7 | $SiO_2$ (low-OH)/Hard polymer | 400 | 400–1700 | 0.50 |
| Fib8 | $SiO_2$:$GeO_2$/$SiO_2$ | 125 | 400–2200 | n.d. |

The transmission properties of the module were studied by measuring the power generated by the TJ cells coupled to the OFs listed in Table 5.2. To allow a direct comparison between the various fibres, the output power of the cell ($P_{\text{cell}}$) was normalised to the DNI using the formula

$$\bar{P}_n = \frac{P_{\text{cell}}}{\text{DNI}}, \tag{5.1}$$

with $n$ the fibre identification number (*i.e.* Fib-$n$). The tests have been carried out at the Cyprus Institute (35.1° N, 33.4° E) during the second half of October, under a maximum DNI of $830 \pm 12\,\text{W}\cdot\text{m}^{-2}$. The results reported in Fig. 5.7 indicate that the normalised power outputs of the cells coupled to the chosen fibres are as follows: $\bar{P}_4 = 0.10 \pm 0.03$ mW, $\bar{P}_5 = 4.5 \pm 0.1$ mW, $\bar{P}_6 = 2.0 \pm 0.1$ mW, $\bar{P}_7 = 20 \pm 1$ mW, and $\bar{P}_8 = 0.4 \pm 0.1$ mW. The high uncertainty characterising $\bar{P}_7$ is due to the sub-optimal weather conditions on the day of the measurement. In spite of this, the ratio $\bar{P}_7/\bar{P}_5$ is approximately equal to 4, confirming the expectations given by the cross-sectional areas of the two fibres. The difference between $\bar{P}_5$ and $\bar{P}_6$ may be due to the different cleavage and alignment of the sample with the mirror optical axis. However, we believe that the chemical composition of the two OFs is at the origin of the observed $\bar{P}$ values. In fact, despite being both pure-silica core fibres, Fib5 is characterised by a low concentration of hydroxyl (OH) groups whereas Fib6 has a higher concentration of them. This influences the transmission properties of the fibres and accounts for Fib5 being best suited for transmitting Vis–IR light while Fib6 being more efficient in the UV domain. The higher OH content, however, is known to favour the photoinduced formation of non-bridging hole centres (NBOHCs) which are a main cause of solarisation in OFs. To investigate this aspect, we calculated the spectral irradiance emitted by the back end of the OFs as

$$E_n(\lambda) = E_0(\lambda)\, e^{-A_n(\lambda)\, l_n}, \tag{5.2}$$

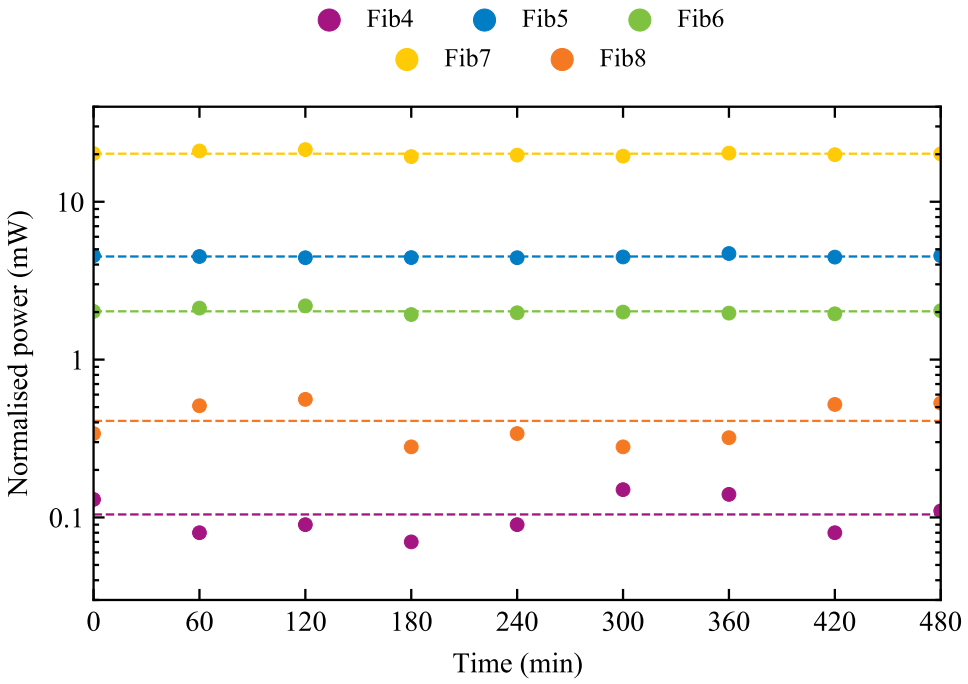


**Figure 5.7.** Time series plot of the normalised power measured during 8 h of concentrated sunlight exposure. The dashed lines indicate the average normalised power transmitted by each fibre.

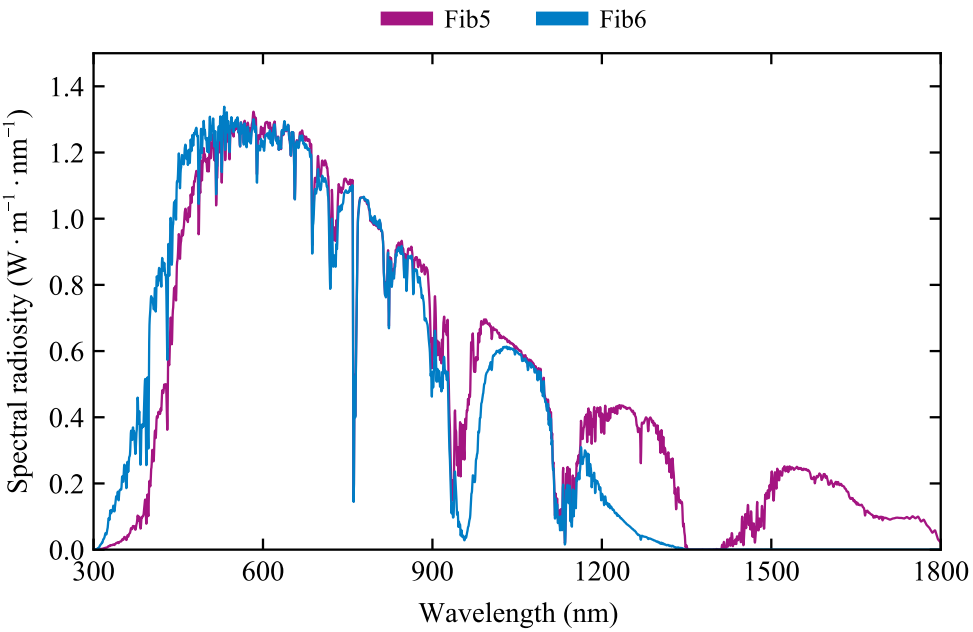


**Figure 5.8.** Solar spectral radiosity transmitted by Fib5 (low-OH) and Fib6 (high-OH). The three coloured areas correspond to the spectral response ranges of the InGaP (300–660 nm), InGaAs (660–885 nm), and Ge (885–1850 nm) layers of the TJ solar cell.

where $l_n$ is the sample length (2.50 m in both cases), $E_0(\lambda)$ is the direct solar irradiation AM1.5D, and $A_n(\lambda)$ is the fibre spectral attenuation declared by the manufacturer. The curves in Fig. 5.8 show that Fib6 has high transparency in the 300–1200-nm range but blocks longer wavelengths whereas Fib5 works better in the range 400–2200 nm but fails at guiding UV light. Since the subcells of the TJ cell are internally connected in series, the photogenerated current is determined by the layer receiving the lowest radiation flux. This means that the spectral distribution of the incident light plays a fundamental role on the correct functioning of the entire TJ cell. The InGaP, InGaAs, and Ge subcells have band gaps approximately equal to 1.88 eV, 1.39 eV, and 0.67 eV, which means that they can absorb light of wavelengths 300–660 nm, 660–885 nm, and 885–1850 nm, respectively. By integrating $E_n(\lambda)$ and $E_0(\lambda)$ over the spectral response range ($\Lambda$) of the three subcells, we can determine the theoretical percent transmittance as

$$T_n = \frac{\int_\Lambda E_n(\lambda)\,d\lambda}{\int_\Lambda E_0(\lambda)\,d\lambda}. \tag{5.3}$$

Table 5.3 reveals that the lowest transmittance of Fib5 is between 660 and 885 nm while that of Fib6 is in the 885–1850-nm spectral range. This implies that the efficiency of the solar cell coupled to these fibres is limited by the current generated by, respectively, the InGaAs and the Ge layer. The ratio between the two limiting $T$ values ($29\%/52\% = 0.56$) is compatible with the ratio $\bar{P}_6/\bar{P}_5 = 0.4 \pm 0.2$, confirming that the difference observed for the two time series is largely determined by the intrinsic absorption of the silica glass.

**Table 5.3.** Percent transmittance of Fib5 and Fib6 in the spectral response range ($\Lambda$) of the InGaP (300–660 nm), InGaAs (660–885 nm), and Ge (885–1850 nm) subcells of the TJ solar cell.

| $\Lambda$ (nm) | $T_5$ | $T_6$ |
|---|---|---|
| 300–660 | 71% | 88% |
| 660–885 | 52% | 51% |
| 885–1850 | 56% | 29% |

Due to the reduced core diameter and NA of Fib4 and Fib8, only a small amount of light was injected into the sample. The produced photocurrent ($\sim 20\,\mu$A) is comparable to the noise current and for this reason the normalised power is close to zero. If the generated power depended only on the fibre cross-section, we would have $\bar{P}_4 = \bar{P}_5/4$. Since this is not the case, the poor light injection observed in our tests is not related to the surface exposed to the sunlight but depends on the fibre

acceptance angle. Even increasing the diameter of the OF or putting many of them together to make a bundle, the transmitted light would still be low as the incident beam angular aperture would be larger than the fibre NA. This finding suggests that fibres with an NA equal to or less than 0.22 are not suitable for the development of the hybrid DL/HCPV module.

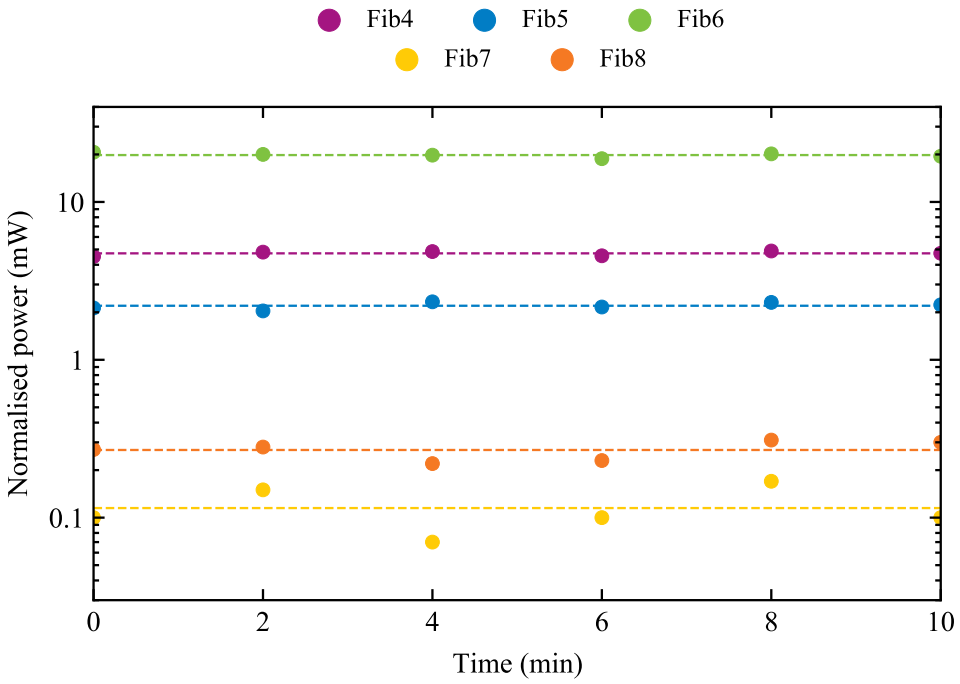


**Figure 5.9.** Time series plot of the normalised power measured during 10 min of concentrated sunlight exposure. The dashed lines indicate the average normalised power transmitted by each fibre.

To further validate the results, we conducted a second test which consisting in the simultaneous exposure of all fibres to concentrated sunlight. For this test five FAE modules were adapted as in Fig. 5.5 and each fibre was coupled to a different TJ cell. This allowed us to exclude any errors caused by the HCPV system alignment and the daily variability of the DNI. As observed in the previous case, the $P_n$ series plotted in Fig. 5.9 are constant over time and their $\bar{P}$ values are: $\bar{P}_4 = 0.11 \pm 0.03$ mW, $\bar{P}_5 = 4.7 \pm 0.2$ mW, $\bar{P}_6 = 2.2 \pm 0.1$ mW, $\bar{P}_7 = 19.8 \pm 0.9$ mW, and $\bar{P}_8 = 0.27 \pm 0.5$ mW. These values are compatible with those shown in Fig. 5.7 and for this reason we can affirm that the outcomes of the day-long tests are reliable and are equivalent to the results we would have obtained by testing all the fibres at once. Furthermore, the obtained results show that the fibres are not affected by concentrated light irradiation, confirming the results of the laser tests reported in the previous chapter.

## 5.4 Efficiency analysis

The total power efficiency of our hybrid system can be calculated as

$$\eta_T = \frac{P_{\text{out}}}{P_{\text{in}}}, \tag{5.4}$$

where $P_{\text{out}}$ is the maximum normalised power generated by the cell and $P_{\text{in}}$ is the radiant flux injected into the fibre (DNI). Since our aim is to calculate the maximum efficiency of the system, in the following calculation we will refer to Fib7 as it is the OF with the highest value of $\bar{P}$. In order to be transmitted, the light hitting the entry face of an optical fibre must form an angle with the optical axis lower than or equal to the acceptance angle $\theta$ of the fibre. Considering that Fib7 has an NA of 0.50, the injection condition is

$$\theta = \sin^{-1}(\text{NA}) = 30^\circ \tag{5.5}$$

and the area of the circle formed by the intersection of the mirror with the light cone subtended by the OF (the dark-blue beam in Fig. 5.5) is calculated as

$$A_{\text{M}} = \pi(\text{EFL} \cdot \tan\theta)^2 = 1380\,\text{cm}^2, \tag{5.6}$$

with EFL being the mirror effective focal length (36.3 cm). Knowing that the maximum solar irradiance measured during the tests is $E_{\text{S}} = 768\,\text{W} \cdot \text{m}^{-2}$, we can calculate the maximum radiant flux injected into the fibre as

$$\Phi_{\text{M}} = E_{\text{S}} A_{\text{M}} = 106\,\text{W}. \tag{5.7}$$

Since the mirror focal image has an area ($A_{\text{MFI}}$) of 1 $\text{cm}^2$ and the cross-sectional area of Fib7 is $A_{\text{F}} = 1.26 \times 10^{-3}\,\text{cm}^2$, the flux collected by the fibre is

$$\Phi_{\text{F}} = \frac{\Phi_{\text{M}} A_{\text{F}}}{A_{\text{MFI}}} = 134\,\text{mW}. \tag{5.8}$$

By considering $\Phi_{\text{F}}$ as the radiant flux injected into the fibre (*i.e.* $P_{\text{in}}$) and the maximum value (21.40 mW) of $\bar{P}_7$ as the maximum normalised power generated by the cell ($P_{\text{out}}$), the total power efficiency of the system is

$$\eta_T = \frac{\max(\bar{P}_7)}{\Phi_{\text{F}}} = 0.16\,. \tag{5.9}$$

This value is useful for estimating the system's ability to produce electricity from sunlight but provides little information about the goodness of the coupling between the mirror and the fibre. This information can be obtained by considering that, for our system, $\eta_T$ is defined as

$$\eta_T = \eta_o\,\eta_e, \tag{5.10}$$

where the first factor is the optical efficiency of the mirror–fibre coupling and the second is the electric conversion efficiency of the cell. Since we know that the TJ cell has an $\eta_e = 0.33$, the optical efficiency of the system is

$$\eta_o = \frac{\eta_e}{\eta_T} = 0.49\,. \tag{5.11}$$

This result clearly proves that (i) the DL/HCPV module is able guide the sunlight to a remote array of solar cells placed in controlled environment and that (ii) the optical fibres resist to high-concentrated sunlight without loosing their transparency in the range of interest. This latter aspect validates the results reported in Chapter 4 on the solarisation resistance of commercial pure-silica high-NA optical fibres.

## 5.5 Optical performance

The optical performance of our hybrid system equipped with Fib7 was evaluated with both spectroscopic and radiometric measurements. By coupling the fibre far end to a spectrophotometer, we studied the evolution of the fibre transmission properties as a function of time. After a full day of exposure to concentrated sunlight, we obtained the *on-line* RIA spectrum shown in Fig. 5.10. A part from the small fluctuations caused by a low signal-to-noise ratio, the attenuation profile is flat over the studied spectral range and has a mean value of $\sim 0.2\,\mathrm{dB}\cdot\mathrm{m}^{-1}$. This result confirms once again that pure-silica core fibres are highly stable under concentrated-light irradiation and do not show any significant photo-induced damages.

Even though the radiant flux transmitted by the fibre is constant during the whole experiment, the intrinsic attenuation of the silica glass may alter the spectral distribution of the injected sunlight and thus change the perceived colour of the emitted light. In order to assess the impact of OF transmission on light quality, we mapped the fibre spectral excitance $M(\lambda, T)$ into three new parameters defined as follows:

$$X_T = \int_0^\infty \bar{x}(\lambda) M(\lambda, T)\, d\lambda,$$

$$Y_T = \int_0^\infty \bar{y}(\lambda) M(\lambda, T)\, d\lambda,$$

$$Z_T = \int_0^\infty \bar{z}(\lambda) M(\lambda, T)\, d\lambda.$$

information given by the calculated the from the measured . This parameter measures the chromaticity (*i.e.* the light flux distribution as a function of the wavelength) of a black body radiator heated to a pre-determined temperature ($T$) and is used to define the colour appearance of a source. Its value is calculated by first mapping to the CIE as follows:

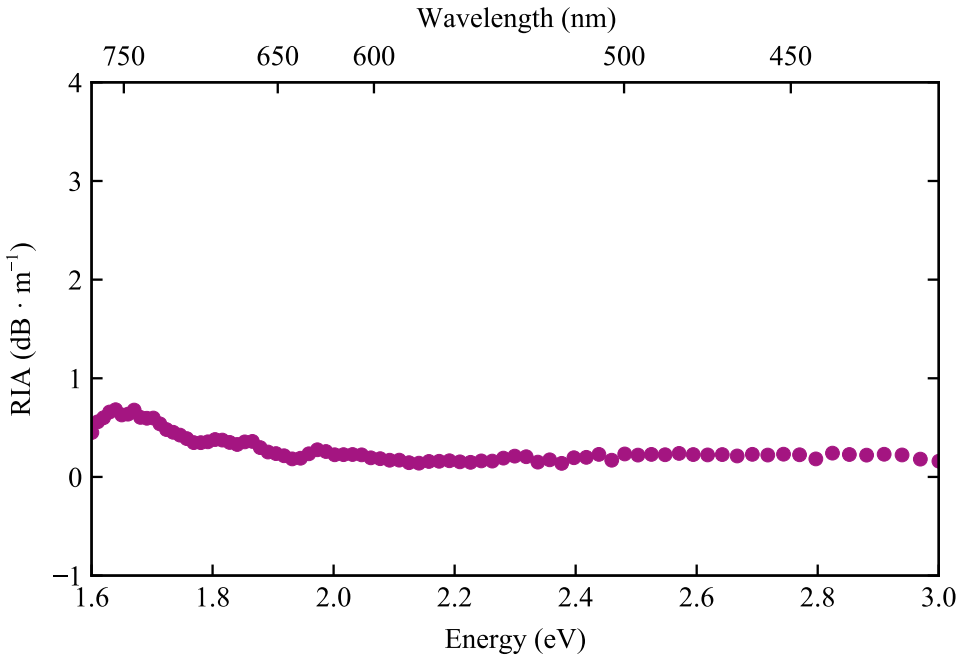


**Figure 5.10.** RIA spectrum measured for Fib7 after a day of concentrated-light exposure in the hybrid module.

The values $X_T$, $Y_T$, and $Z_T$ are called the tristimulus values and correspond to the intensity of the light transmitted by Fib7 based on the three primary colour values (RGB) of the CIE 1931 colour space [233]. The functions $\bar{x}(\lambda)$, $\bar{y}(\lambda)$, and $\bar{z}(\lambda)$ are the CIE colour matching functions and can be thought of as the spectral sensitivity curves of three linear light detectors yielding the CIE tristimulus values [234]. From the $X_T$, $Y_T$, and $Z_T$ we derived the CIE chromaticity coordinates

$$x_T = \frac{X_T}{X_T + Y_T + Z_T} = 0.35$$

$$y_T = \frac{Y_T}{X_T + Y_T + Z_T} = 0.34$$

which define the point $P(x_T, y_T)$ on the chromaticity diagram in Fig. 5.11a. The curved line traced on the diagram is the so-called black body or Planckian locus, that is the path representing the colour of the light produced by a black body when its temperature is changed [235]. Since the point $P$ does not belong to the Planckian locus, the colour of the light transmitted by Fib7 can be described by referring to the temperature of the black body having the nearest chromaticity. In our case, the so-called correlated colour temperature (CCT) of the transmitted light is 4700 K, which is slightly lower than the effective temperature of the Sun (5780 K). This means that the light produced by the hybrid module is slightly red-shifted with respect to natural light, but the extent of this effect is visually negligible (Fig. 5.11) and may be of little significance for the development of hybrid systems for indoor

natural lighting.

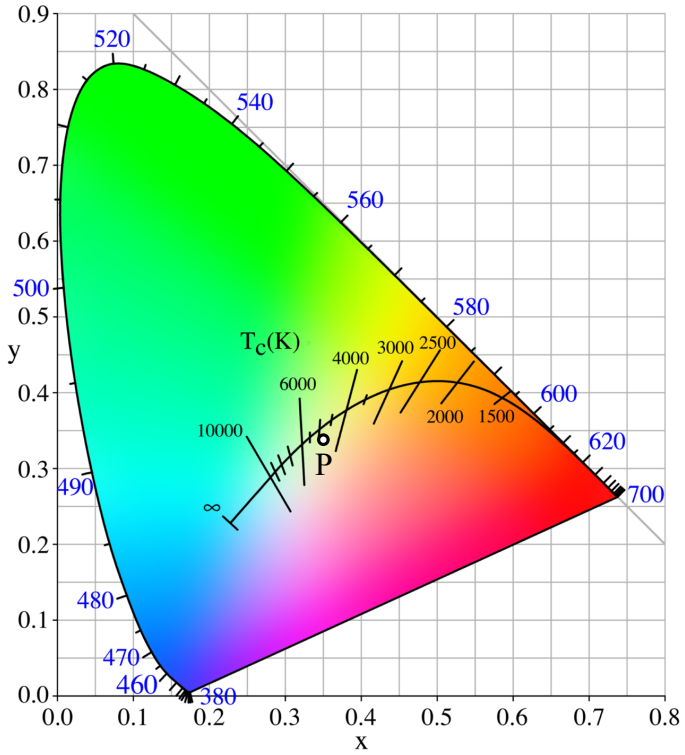


**(a)**

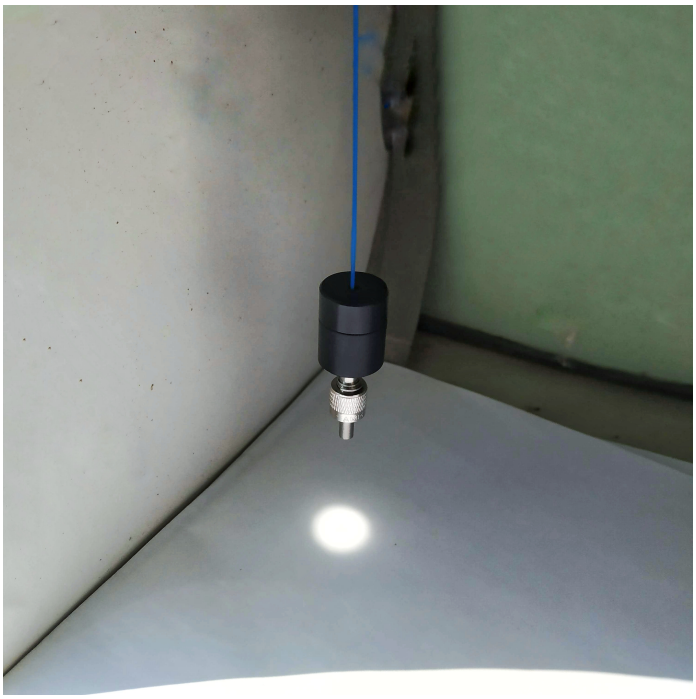

**(b)**

**Figure 5.11.** (a) The CIE 1931 colour space chromaticity diagram showing the Planckian locus (black line) and the point *P* corresponding to the colour of the light transmitted by Fib7. (b) Photography of the sunlight output at the far end of a Fib7.

# Conclusions

This Ph.D. thesis focused on the development of a hybrid daylighting/high-concentration photovoltaic (DL/HCPV) system for building illumination and power supply. The prototypical module was realised as an upgrade of a functioning HCPV system called FAE ("Fotovoltaico ad Alta Efficienza") developed by the industrial partner IDEA Srl and installed at the "Università degli Studi di Palermo", Italy. The FAE system is composed of 40 HCPV modules divided into 4 semi-trackers. Each module consists of an off-axis parabolic mirror concentrating 250 W of sunlight on a InGaP–InGaAs–Ge triple-junction solar cell with a concentration ratio of 2000×. A BK7-glass inverse truncated pyramid is used as a secondary optics to homogenise the beam coming from the concentrator and increase the acceptance angle of the receiver.

The experimental work carried out to build the hybrid module can be summarised as follows:

**First stage – Optical coupling.** As a first step, we used the simulation software Zemax OpticStudio18 to study the optical properties of the original FAE system. The simulations confirmed the data obtained from experimental measurements and gave us important information about the geometry of the beam redirected by the parabolic mirror. Using these results we simulated an upgraded module in which the receiver was replaced with either three bare fibres of different size, a fibre bundle, an end-capped fibre, an aspheric lens, or an aspheric telephoto lens. The results suggested that the two best performing optics are the aspheric telephoto lens and the fibre bundle. The former has the advantage of reducing the image size and angular aperture with virtually no power loss, but accounts for a more complex and expensive design. Conversely, the latter allows the collection of concentrated sunlight without significant loss and has the advantage of being the more cost-effective

and easy-to-handle. The other optics demonstrated to be incompatible with the mirror due to either a low numerical aperture or a low coupling efficiency. For these reasons, we decided to adopt the fibre bundle as the optics for the realisation of our DL/HCPV module.

**Second stage – Fibre resistance.** The second question we aimed to answer is, Which optical fibre is the most suitable for concentrated solar applications? To this end we selected five different optical fibres and tested them using various light sources and lasers. By using a broadband continuous light source, we demonstrated that Al- and P-doped silica core fibres undergo a quick photodarkening which results in the formation of point defects absorbing in the UV–Vis spectral range. On the contrary, Ge-doped fibres proved to resist well to concentrated light and only showed a UV attenuation band which, however, does not prevent the transmission of visible and NIR wavelengths. The light exposure of pure-silica core/hard-polymer cladding samples led to the onset of an absorption band tentatively assigned to chlorine impurities of the silica matrix or to a degradation process occurring inside the polymeric cladding. The only fibre showing no signs of solarisation was the F-doped silica core one, not even after a "2 days/1 night cycle" test consisting in 24 h of light exposure and 12  of recovery.

**Third stage – Prototype development and testing.** The results obtained from the preceding two stages suggested that a convenient way to build a DL/HCPV module is to couple the concentrator to a bundle of either Ge-doped or pure-silica fibres. For this reason we selected the three fibres which gave positive results in the second stage of the investigation (*i.e.* the pure-silica core F-doped silica cladding fibre, the Ge-doped silica core fibre, and pure-silica core hard-polymer cladding fibre) together with other two pure-silica samples and tested the efficiency of the device as a function of the fibre composition.By analysing the optical and energy-production performance of the prototype we verified that the highest transmission efficiency is achieved by using a high-NA (0.50) 400-µm diameter optical fibre made of high purity, low-hydroxyl silica. Thinner fibres (the F- and Ge-doped ones) did not allow the injection of sufficient sunlight and suggested us that 200 µm should be considered as the smallest diameter usable to collect sunlight with the specific geometry of the FAE system. The total power and optical efficiencies measured for the system are respectively 16% and 49%, which represent a good result given that the mirror was coupled with just one bare optical fibre at a time. By carrying out a visual and colorimetric analysis of the output light, we also demonstrated that the quality and intensity of the light is appropriate for indoor illumination purposes.

The results obtained for the prototype system suggest that daylighting and high-concentration photovoltaic technologies can be integrated in a single multifunc-

tional system to provide effective lightning and energy supply for domestic and commercial buildings. The proposed proof-of-concept clearly demonstrate that innovative hybrid DL/HCPV systems can be realised using low-cost, commercially available optical fibres, sensibly reducing the costs of this technology which is one of the major drawbacks to its widespread. Moreover, by transporting sunlight via fibre optics, the solar cells can be installed indoors where temperature, humidity, and dust can be easily controlled. These outcomes opens the way to new research directions that may lead to the large-scale production of hybrid systems and thus help achieving the world's carbon reduction targets.

# Bibliography


[1] Statistical Review of World Energy 2020 (69$^{th}$ edition). bp, 2020. Available online: *https://www.bp.com/content/dam/bp/business-sites/en/global/corporate/pdfs/energy-economics/statistical-review/bp-stats-review-2020-full-report.pdf*.

[2] Energy statistics – An overview. Eurostat, 2020. Available online: *https://ec.europa.eu/eurostat/statistics-explained/pdfscache/29046.pdf*.

[3] World Energy Outlook 2020. International Energy Agency, Paris, 2020. Available online: *https://www.iea.org/reports/world-energy-outlook-2020*.

[4] Energy Outlook: 2020 edition. bp, 2020. Available online: *https://www.bp.com/content/dam/bp/business-sites/en/global/corporate/pdfs/energy-economics/energy-outlook/bp-energy-outlook-2020.pdf*.

[5] Global Renewables Outlook: Energy Transformation 2050. International Renewable Energy Agency, 2020. Available online: *https://www.irena.org/-/media/Files/IRENA/Agency/Publication/2020/Apr/IRENA_Global_Renewables_Outlook_2020.pdf*.

[6] M. Iqbal. The solar constant and its spectral distribution. In *An Introduction to Solar Radiation*, Elsevier BV (1983), pp. 43–58.

[7] National Renewable Energy Laboratory (NREL). Solar Spectra. Available online: *https://www.nrel.gov/grid/solar-resource/spectra.html*

[8] M. Iqbal. Solar spectral radiation under cloudless skies. In *An Introduction to Solar Radiation*, Elsevier BV (1983), pp. 107–168.

[9] J. A. Duffie, W. A. Beckman. Available solar radiation. In *Solar Engineering of Thermal Processes*, John Wiley & Sons, Inc. (2013), pp. 43–137.

[10] C. Gueymard, D. Myers, K. Emery. Proposed reference irradiance spectra for solar energy systems testing. *Sol. Energy* **2002**, *73*, 443–467.

[11] L. L. Vant-Hull. Concentrator optics. In *Solar Power Plants*, Springer Berlin Heidelberg (1991), pp. 84–133.

[12] D. Buie, A. Monger, C. Dey. Sunshape distributions for terrestrial solar simulations. *Sol. Energy* **2003**, *74*, 113–122.

[13] D. F. Grether, D. Evans, A. Hunt, M. Wahlig. Application of circumsolar measurements to concentrating collectors. *Proc. ISES Solar World Congress Atlanta Boer K. W.; Glenn B. H. (Ed.) Newark/DE: American Section of ISES* **1979**.

[14] A. Neumann, A. Witzke, S. A. Jones, G. Schmitt. Representative terrestrial solar brightness profiles. In *Solar Energy* (2002).

[15] Y. Eissa, P. Blanc, A. Oumbe, H. Ghedira, L. Wald. Estimation of the circumsolar ratio in a turbid atmosphere. *Energy Procedia* **2014**, *57*, 1169–1178.

[16] Renewable power generation costs in 2019. International Renewable Energy Agency, 2020. Available online: *https://www.irena.org/-/media/Files/IRENA/Agency/Publication/2020/Jun/IRENA_Power_Generation_Costs_2019.pdf*.

[17] Renewables 2020 Global Status Report. REN21, 2020. Available online: *https://www.ren21.net/wp-content/uploads/2019/05/gsr_2020_full_report_en.pdf*.

[18] D. D. Smith, G. Reich, M. Baldrias, M. Reich, N. Boitnott, G. Bunea. Silicon solar cells with total area efficiency above 25%. In *2016 IEEE 43rd Photovoltaic Specialists Conference* (2016).

[19] Current status of concentrator photovoltaic (CPV) technology, 2015. Available online: *https://www.nrel.gov/docs/fy16osti/65130.pdf*.

[20] N. Taylor, A. Jäger-Waldau. *Photovoltaics: technology development report*. Joint Research Centre (European Commission), 2019.

[21] M. Steiner, G. Siefer, T. Schmidt, M. Wiesenfarth, F. Dimroth, A. W. Bett. 43% sunlight to electricity conversion efficiency using CPV. *IEEE J. Photovolt.* **2016**, *6*, 1020–1024.

[22] H. Zheng. Solar energy utilization and its collection devices. In *Solar Energy Desalination Technology*, Elsevier BV (2017), pp. 47–171.

[23] W. Welford, R. Winston. Concentrators and their uses. In *High Collection Nonimaging Optics*, Elsevier BV (1989), pp. 1–7.

[24] Y. Wu, K. Connelly, Y. Liu, X. Gu, Y. Gao, G. Z. Chen. Smart solar concentrators for building integrated photovoltaic façades. *Sol. Energy* **2016**, *133*, 111–118.

[25] A. Rabl, N. Goodman, R. Winston. Practical design considerations for CPC solar collectors. *Sol. Energy* **1979**, *22*, 373–381.

[26] M. Tian, Y. Su, H. Zheng, G. Pei, G. Li, S. Riffat. A review on the recent research progress in the compound parabolic concentrator (CPC) for solar energy applications. *Renew. Sustain. Energy Rev.* **2018**, *82*, 1272–1296.

[27] R. V. Parupudi, H. Singh, M. Kolokotroni. Low concentrating photovoltaics (LCPV) for buildings and their performance analyses. *Appl. Energy* **2020**, *279*, 115839.

[28] T. Uematsu, Y. Yazawa, Y. Miyamura, S. Muramatsu, H. Ohtsuka, K. Tsutsui, T. Warabisako. Static concentrator photovoltaic module with prism array. *Sol. Energy Materials and Solar Cells* **2001**, *67*, 415–423.

[29] N. Vu, S. Shin. A concentrator photovoltaic system based on a combination of prism-compound parabolic concentrators. *Energies* **2016**, *9*, 645.

[30] M. Al-Najideen, M. Al-Shidhani, G. Min. Optimum design of V-trough solar concentrator for photovoltaic applications. In *15th International Conference on Concentrator Photovoltaic Systems (CPV-15)* (2019).

[31] V. Poulek, A. Khudysh, M. Libra. Innovative low concentration PV systems with bifacial solar panels. *Sol. Energy* **2015**, *120*, 113–116.

[32] R. Tang, X. Liu. Optical performance and design optimization of v-trough concentrators for photovoltaic applications. *Sol. Energy* **2011**, *85*, 2154–2166.

[33] P. Pérez-Higueras, E. Muñoz, G. Almonacid, P. Vidal. High concentrator PhotoVoltaics efficiencies: Present status and forecast. *Renew. Sustain. Energy Rev.* **2011**, *15*, 1810–1815.

[34] D. Talavera, J. Ferrer-Rodrguez, P. Pérez-Higueras, J. Terrados, E. Fernández. A worldwide assessment of levelised cost of electricity of HCPV systems. *Energy Convers. Manag.* **2016**, *127*, 679–692.

[35] D. Chemisana. Building integrated concentrating photovoltaics: A review. *Renew. Sustain. Energy Rev.* **2011**, *15*, 603–611.

[36] K. Lovegrove, J. Pye. Fundamental principles of concentrating solar power (CSP) systems. In *Concentrating Solar Power Technology*, Elsevier BV (2012), pp. 16–67.

[37] K. Shanks, S. Senthilarasu, T. K. Mallick. Optics for concentrating photovoltaics: Trends, limits and opportunities for materials and design. *Renew. Sustain. Energy Rev.* **2016**, *60*, 394–407.

[38] I. Luque-Heredia, P. Magalhães, M. Muller. CPV tracking and trackers. In *Handbook of Concentrator Photovoltaic Technology*, John Wiley & Sons, Inc. (2016), pp. 293–338.

[39] R. Mohedano, R. Leutz. CPV optics. In *Handbook of Concentrator Photovoltaic Technology*, John Wiley & Sons, Inc. (2016), pp. 187–238.

[40] J. Jaus, A. Bett, H. Reinecke, E. Weber. Reflective secondary optical elements for fresnel lens based concentrator modules. *Prog. Photovolt.* **2011**, *19*, 580–590.

[41] S. E. Himer, A. Ahaitouf, S. El-Yahyaoui, A. Mechaqrane, A. Ouagazzaden. A comparative of four secondary optical elements for CPV systems. In *AIP Conference Proceedings* (2018), *Vol. 2012*, p. 030003.

[42] M. Victoria, C. Domnguez, I. Antón, G. Sala. Comparative analysis of different secondary optical elements for aspheric primary lenses. *Opt. Express* **2009**, *17*, 6487.

[43] M. Wiesenfarth, T. Dörsam, F. Eltermann, T. Hornung, G. Siefer, M. Steiner, S. van Riesen, M. Neubauer, A. Boos, S. Wanka et al. CPV module with fresnel lens primary optics and homogenizing secondary optics. In *AIP Conference Proceedings* (2015), *Vol. 1679*, p. 100007.

[44] M. Victoria, S. Askins, I. Antón, G. Sala, G. Duggan. Temperature effects on two-stage optics made of silicone. In *AIP Conference Proceedings* (2014), *Vol. 1616*, pp. 92–96.

[45] T. Schmid, M. Wiesenfarth, T. Hornung, M. Gremmelspacher, P. Manns, P. Nitz. Mass manufactured secondary optics for CPV. In *AIP Conference Proceedings* (2014), *Vol. 1616*, pp. 84–87.

[46] C. A. DiMarzio. *Optics for Engineers*. CRC Press, 2011.

[47] D. J. Brady. *Optical Imaging and Spectroscopy*. John Wiley & Sons, Inc., 2009.

[48] I. Rey-Stolle, J. M. Olson, C. Algora. Concentrator multijunction solar cells. In *Handbook of Concentrator Photovoltaic Technology*, John Wiley & Sons, Inc. (2016), pp. 59–136.

[49] G. Segev, G. Mittelman, A. Kribus. Equivalent circuit models for triple-junction concentrator solar cells. *Sol. Energy Materials and Solar Cells* **2012**, *98*, 57–65.

[50] A. Royne, C. Dey, D. Mills. Cooling of photovoltaic cells under concentrated illumination: A critical review. *Sol. Energy Materials and Solar Cells* **2005**, *86*, 451–483.

[51] P. Gleckman. Achievement of ultrahigh solar concentration with potential for efficient laser pumping. *Appl. Opt.* **1988**, *27*, 4385.

[52] W. T. Welford, R. Winston, D. C. Sinclair. The optics of nonimaging concentrators: Light and solar energy. *Phys. Today* **1980**, *33*, 56–57.

[53] A. Rabl. Comparison of solar concentrators. *Sol. Energy* **1976**, *18*, 93–111.

[54] J. A. Duffie, W. A. Beckman. Concentrating collectors. In *Solar Engineering of Thermal Processes*, John Wiley & Sons, Inc. (2013), pp. 322–372.

[55] D. A. Brannan, M. F. Esplen, J. J. Gray. *Geometry*. Cambridge University Press, 2009.

[56] R. C. Neville. The sun and sunlight. In *Solar Energy Conversion*, Elsevier BV (1995), pp. 39–70.

[57] P. Arguijo, M. S. Scholl. Exact ray-trace beam for an off-axis paraboloid surface. *Appl. Opt.* **2003**, *42*, 3284.

[58] J. E. Howard. Imaging properties of off-axis parabolic mirrors. *Appl. Opt.* **1979**, *18*, 2714.

[59] K. Shanks, S. Senthilarasu, T. K. Mallick. High-concentration optics for photovoltaic applications. In *High Concentrator Photovoltaics*, Springer International Publishing (2015), pp. 85–113.

[60] S. Horne. Concentrating photovoltaic (CPV) systems and applications. In *Concentrating Solar Power Technology*, Elsevier BV (2012), pp. 323–361.

[61] M. Kischkoweit-Lopin. An overview of daylighting systems. *Sol. Energy* **2002**, *73*, 77–82.

[62] M. Nair, K. Ramamurthy, A. Ganesan. Classification of indoor daylight enhancement systems. *Light. Res. Technol.* **2013**, *46*, 245–267.

[63] N. Ruck, Ø. Aschehoug, S. Aydinli, J. Christoffersen, G. Courret, I. Edmonds, R. Jakobiak, M. Kischkoweit-Lopin, M. Klinger, E. Lee, L. Michel, J.-L. Scartezzini, S. Selkowitz. Daylight in buildings – a source book on daylighting systems and components, **2000**.

[64] A. Kontadakis, A. Tsangrassoulis, L. Doulos, S. Zerefos. A review of light shelf designs for daylit environments. *Sustainability* **2017**, *10*, 71.

[65] H. Lee, S. Park, J. Seo. Development and performance evaluation of light shelves using width-adjustable reflectors. *Adv. Civ. Eng.* **2018**, *2018*, 1–9.

[66] K. Vasilakopoulou, D. Kolokotsa, M. Santamouris, I. Kousis, H. Asproulias, I. Giannarakis. Analysis of the experimental performance of light pipes. *Energy Build.* **2017**, *151*, 242–249.

[67] D. Vázquez-Molin, M. González-Montes, A. Á. Fernández-Balbuena, Á. Garca-Botella, W. Pohl, T. Galan, E. Bernabéu. Horizontal daylighting system for office buildings. *Energy Build.* **2013**, *67*, 525–530.

[68] V. Garcia-Hansen, I. Edmonds. Methods for the illumination of multilevel buildings with vertical light pipes. *Sol. Energy* **2015**, *117*, 74–88.

[69] M. Al-Marwaee, D. Carter. Tubular guidance systems for daylight: Achieved and predicted installation performances. *Appl. Energy* **2006**, *83*, 774–788.

[70] J. T. Kim, G. Kim. Overview and new developments in optical daylighting systems for building a healthy indoor environment. *Build. Environ.* **2010**, *45*, 256–269.

[71] La Foret Engineering Co., Ltd. Himawari Solar Lighting System. Available online: *https://www.himawari-net.co.jp/e-pdf/New-Himawari-Catalogue-140331-1.pdf*

[72] M. Mayhoub, D. Carter. Towards hybrid lighting systems: A review. *Light. Res. Technol.* **2009**, *42*, 51–71.

[73] A. J.-W. Whang, T.-H. Yang, Z.-H. Deng, Y.-Y. Chen, W.-C. Tseng, C.-H. Chou. A review of daylighting system: For prototype systems performance and development. *Energies* **2019**, *12*, 2863.

[74] Parans Solar Lighting AB (publ). SP4 Sunlight Collector. Available online: *https://www.parans.com/wp-content/uploads/2020/06/Parans_Product_information_2020_2.0.pdf*

[75] M. Mayhoub, D. Carter. Hybrid lighting systems: Performance and design. *Light. Res. Technol.* **2011**, *44*, 261–276.

[76] European Committee for Standardization. European Standard EN 12464-1:2011. Light and lighting – Lighting of work places – Part 1: Indoor work places. Available online: *https://lumenlightpro.com/wp-content/themes/lumenlightpro/assets/EN_12464-1.pdf*

[77] A. Tsangrassoulis, L. Doulos, M. Santamouris, M. Fontoynont, F. Maamari, M. Wilson, A. Jacobs, J. Solomon, A. Zimmerman, W. Pohl, G. Mihalakakou. On the energy efficiency of a prototype hybrid daylighting system. *Sol. Energy* **2005**, *79*, 56–64.

[78] S. Amara, B. Nordell, B. Benyoucef, A. Benmoussat. Concentration heating system with optical fiber supply. *Energy Procedia* **2011**, *6*, 805–814.

[79] A. Aslian, B. H. S. Asli, C. J. Tan, F. R. M. Adikan, A. Toloei. Design and analysis of an optical coupler for concentrated solar light using optical fibers in residential buildings. *Int. J. Photoenergy* **2016**, *2016*, 1–11.

[80] L. Sedki, M. Maaroufi. Design of parabolic solar daylighting systems based on fiber optic wires: A new heat filtering device. *Energy Build.* **2017**, *152*, 434–441.

[81] I. Ullah, A. Whang. Development of optical fiber-based daylighting system and its comparison. *Energies* **2015**, *8*, 7185–7201.

[82] N. H. Vu, S. Shin. Flat optical fiber daylighting system with lateral displacement sun-tracking mechanism for indoor lighting. *Energies* **2017**, *10*, 1679.

[83] N.-H. Vu, T.-T. Pham, S. Shin. Modified optical fiber daylighting system with sunlight transportation in free space. *Opt. Express* **2016**, *24*, A1528.

[84] N. H. Vu. Optical fiber daylighting system featuring alignment-free. *Int. J. Energy Eng.* **2016**, *5*, 60.

[85] O. N. Obianuju, K.-K. Chong. High acceptance angle optical fiber based daylighting system using two-stage reflective non-imaging dish concentrator. *Energy Procedia* **2017**, *105*, 498–504.

[86] M. V. Lapsa, L. C. Maxey, D. D. Earl, D. L. Beshears, C. D. Ward, J. E. Parks. Hybrid solar lighting provides energy savings and reduces waste heat. *Energy Engineering* **2007**, *104*, 7–20.

[87] C. Wang, H. Abdul-Rahman, S. Rao. Daylighting can be fluorescent: Development of a fiber solar concentrator and test for its indoor illumination. *Energy Build.* **2010**, *42*, 717–727.

[88] I. Antón, D. Silva, G. Sala, A. Bett, G. Siefer, I. Luque-Heredia, T. Trebst. The PV-FIBRE concentrator: A system for indoor operation of 1000× MJ solar cells. *Prog. Photovolt.* **2007**, *15*, 431–447.

[89] R. Núñez, I. Antón, G. Sala. Hybrid lighting-CPV, a new efficient concept mixing illumination with CPV. *Opt. Express* **2013**, *21*, 4864.

[90] R. Núñez, I. Antón, G. Sala. Proof-of-concept of a building-integrated hybrid concentrator photovoltaics-lighting system. *Light. Res. Technol.* **2017**, *50*, 1082–1090.

[91] E. Ringdalen. Changes in quartz during heating and the possible effects on Si production. *JOM* **2014**, *67*, 484–492.

[92] L. R. Drees, L. P. Wilding, N. E. Smeck, A. L. Senkayi. Silica in soils: Quartz and disordered silica polymorphs. In *Minerals in Soil Environments (2nd ed., Vol. 1)*, Soil Science Society of America (2018), pp. 913–974.

[93] C. V. Raman, T. M. K. Nedungadi. The $\alpha$–$\beta$ transformation of quartz. *Nature* **1940**, *145*, 147–147.

[94] O. W. Flörke, H. A. Graetsch, F. Brunk, L. Benda, S. Paschen, H. E. Bergna, W. O. Roberts, W. A. Welsh, C. Libanati, M. Ettlinger et al. Silica. In *Ullmann's Encyclopedia of Industrial Chemistry*, Wiley (2000).

[95] L. Pauling. The nature of siliconoxygen bonds. *American Mineralogist* **1980**, *65*, 321–323.

[96] K. Awazu, H. Kawazoe. Strained Si–O–Si bonds in amorphous $SiO_2$ materials: A family member of active centers in radio, photo, and chemical responses. *J. Appl. Phys.* **2003**, *94*, 6243–6262.

[97] J. P. Rino, I. Ebbsjö, R. K. Kalia, A. Nakano, P. Vashishta. Structure of rings in vitreous $SiO_2$. *Phys. Rev. B* **1993**, *47*, 3053–3062.

[98] A. C. Wright. Neutron scattering from vitreous silica. v. the structure of vitreous silica: What have we learned from 60 years of diffraction studies? *J. Non-Cryst. Solids* **1994**, *179*, 84–115.

[99] T. Charpentier, P. Kroll, F. Mauri. First-principles nuclear magnetic resonance structural analysis of vitreous silica. *J. Phys. Chem. C* **2009**, *113*, 7917–7929.

[100] U. Sternberg. The bond angle dependence of the asymmetry parameter of the oxygen-17 electric field gradient tensor. *Solid State Nucl. Magn. Reson.* **1993**, *2*, 181–190.

[101] T. M. Clark, P. J. Grandinetti. Dependence of bridging oxygen $^{17}O$ quadrupolar coupling parameters on Si–O distance and Si–O–Si angle. *J. Phys. Condens. Matter* **2003**, *15*, S2387–S2395.

[102] J. V. Smith, C. S. Blackwell. Nuclear magnetic resonance of silica polymorphs. *Nature* **1983**, *303*, 223–225.

[103] T. M. Clark, P. J. Grandinetti, P. Florian, J. F. Stebbins. Correlated structural distributions in silica glass. *Phys. Rev. B* **2004**, *70*.

[104] X. Yuan, A. Cormack. Si–O–Si bond angle and torsion angle distribution in vitreous silica and sodium silicate glasses. *J. Non-Cryst. Solids* **2003**, *319*, 31–43.

[105] W. J. Malfait, W. E. Halter, R. Verel. $^{29}Si$ NMR spectroscopy of silica glass: $T_1$ relaxation and constraints on the Si–O–Si bond angle distribution. *Chem. Geol.* **2008**, *256*, 269–277.

[106] A. C. Wright. Diffraction studies of glass structure. *J. Non-Cryst. Solids* **1990**, *123*, 129–148.

[107] R. M. V. Ginhoven, H. Jónsson, L. R. Corrales. Silica glass structure generation for *ab initio* calculations using small samples of amorphous silica. *Phys. Rev. B* **2005**, *71*.

[108] S. V. King. Ring configurations in a random network model of vitreous silica. *Nature* **1967**, *213*, 1112–1113.

[109] L. Guttman. Ring structure of the crystalline and amorphous forms of silicon dioxide. *J. Non-Cryst. Solids* **1990**, *116*, 145–147.

[110] D. S. Franzblau. Computation of ring statistics for network models of solids. *Phys. Rev. B* **1991**, *44*, 4925–4930.

[111] E. Görlich. The structure of $SiO_2$ — Current views. *Ceram. Int.* **1982**, *8*, 3–16.

[112] J. J. Papike. Chemistry of the rock-forming silicates: Multiple-chain, sheet, and framework structures. *Rev. Geophys.* **1988**, *26*, 407.

[113] F. Galeener. Planar rings in glasses. *Solid State Commun.* **1982**, *44*, 1037–1040.

[114] R. A. Barrio, F. L. Galeener, E. Martínez, R. J. Elliott. Regular ring dynamics in $AX_2$ tetrahedral glasses. *Phys. Rev. B* **1993**, *48*, 15672–15689.

[115] Y. Hibino, F. Hanawa, M. Horiguchi. Drawing-induced residual stress effects on optical characteristics in pure-silica-core single-mode fibers. *J. Appl. Phys.* **1989**, *65*, 30–34.

[116] E. J. Friebele, G. H. Sigel, D. L. Griscom. Drawing-induced defect centers in a fused silica core fiber. *Appl. Phys. Lett.* **1976**, *28*, 516–518.

[117] A. Alessi, S. Girard, M. Cannas, S. Agnello, A. Boukenter, Y. Ouerdane. Influence of drawing conditions on the properties and radiation sensitivities of pure-silica-core optical fibers. *J. Light. Technol.* **2012**, *30*, 1726–1732.

[118] H. Hosono, Y. Ikuta, T. Kinoshita, K. Kajihara, M. Hirano. Physical disorder and optical properties in the vacuum ultraviolet region of amorphous $SiO_2$. *Phys. Rev. Letters* **2001**, *87*.

[119] K. S. Song, R. T. Williams. Silicon dioxide. In *Self-Trapped Excitons*, Springer Berlin Heidelberg (1993).

[120] R. M. V. Ginhoven, H. Jónsson, L. R. Corrales. Characterization of exciton self-trapping in amorphous silica. *J. Non-Cryst. Solids* **2006**, *352*, 2589–2595.

[121] S. Ismail-Beigi, S. G. Louie. Self-trapped excitons in silicon dioxide: Mechanism and properties. *Phys. Rev. Letters* **2005**, *95*.

[122] A. L. Shluger. The model of a triplet self-trapped exciton in crystalline $SiO_2$. *J. Phys. C: Solid State Phys.* **1988**, *21*, L431–L434.

[123] M. Stapelbroek, D. Griscom, E. Friebele, G. Sigel. Oxygen-associated trapped-hole centers in high-purity fused silicas. *J. Non-Cryst. Solids* **1979**, *32*, 313–326.

[124] D. Donadio, M. Bernasconi. *Ab initio* simulation of photoinduced transformation of small rings in amorphous silica. *Phys. Rev. B* **2005**, *71*.

[125] T. E. Tsai, D. L. Griscom. Experimental evidence for excitonic mechanism of defect generation in high-purity silica. *Phys. Rev. Letters* **1991**, *67*, 2517–2520.

[126] H. Hosono, H. Kawazoe, N. Matsunami. Experimental evidence for frenkel defect formation in amorphous $SiO_2$ by electronic excitation. *Phys. Rev. Letters* **1998**, *80*, 317–320.

[127] D. L. Griscom. Trapped-electron centers in pure and doped glassy silica: A review and synthesis. *J. Non-Cryst. Solids* **2011**, *357*, 1945–1962.

[128] S. Agnello, R. Boscaino, G. Buscarino, M. Cannas, F. M. Gelardi. Structural relaxation of $E'_\gamma$ centers in amorphous silica. *Phys. Rev. B* **2002**, *66*.

[129] R. A. B. Devine. Defect creation and two-photon absorption in amorphous $SiO_2$. *Phys. Rev. Letters* **1989**, *62*, 340–340.

[130] Y. Glinka, S.-H. Lin, Y.-T. Chen. Two-photon-excited luminescence and defect formation in $SiO_2$ nanoparticles induced by 6.4-eV ArF laser light. *Phys. Rev. B* **2000**, *62*, 4733–4743.

[131] K. Kajihara, Y. Ikuta, M. Hirano, H. Hosono. Power dependence of defect formation in $SiO_2$ glass by $F_2$ laser irradiation. *Appl. Phys. Lett.* **2002**, *81*, 3164–3166.

[132] H. Imai, K. Arai, H. Imagawa, H. Hosono, Y. Abe. Two types of oxygen-deficient centers in synthetic silica glass. *Phys. Rev. B* **1988**, *38*, 12772–12775.

[133] K. Kajihara, Y. Ikuta, M. Oto, M. Hirano, L. Skuja, H. Hosono. UV–VUV laser induced phenomena in $SiO_2$ glass. *Nucl. Instrum. Methods Phys. Res. B* **2004**, *218*, 323–331.

[134] L. Skuja, H. Hosono, M. Hirano. Laser-induced color centers in silica. In *Laser-Induced Damage in Optical Materials: 2000* (2001), G. J. Exarhos, A. H. Guenther, M. R. Kozlowski, K. L. Lewis, M. J. Soileau (Eds).

[135] L. Skuja. Optical properties of defects in silica. In *Defects in $SiO_2$ and Related Dielectrics: Science and Technology*, Springer Netherlands (2000), pp. 73–116.

[136] S. Agnello, G. Buscarino, F. M. Gelardi, R. Boscaino. Optical absorption band at 5.8 eV associated with the $E'_\gamma$ centers in amorphous silicon dioxide: Optical absorption and EPR measurements. *Phys. Rev. B* **2008**, *77*.

[137] L. Giordano, P. V. Sushko, G. Pacchioni, A. L. Shluger. Optical and EPR properties of point defects at a crystalline silica surface: *Ab initio* embedded-cluster calculations. *Phys. Rev. B* **2007**, *75*.

[138] M. Cannas, M. Leone. Photoluminescence at 1.9 eV in synthetic wet silica. *J. Non-Cryst. Solids* **2001**, *280*, 183–187.

[139] L. Skuja. Optically active oxygen-deficiency-related centers in amorphous silicon dioxide. *J. Non-Cryst. Solids* **1998**, *239*, 16–48.

[140] D. L. Griscom. Characterization of three $E'$-center variants in X- and $\gamma$-irradiated high purity $a$-$SiO_2$. *Nucl. Instrum. Methods Phys. Res. B* **1984**, *1*, 481–488.

[141] D. L. Griscom. Optical properties and structure of defects in silica glass. *Journal of the Ceramic Society of Japan* **1991**, *99*, 923–942.

[142] K. Kajihara, L. Skuja, M. Hirano, H. Hosono. In situobservation of the formation, diffusion, and reactions of hydrogenous species in $F_2$-laser-irradiated $SiO_2$ glass using a pump-and-probe technique. *Phys. Rev. B* **2006**, *74*.

[143] H. Nishikawa, R. Nakamura, Y. Ohki, Y. Hama. Correlation of preexisting diamagnetic defect centers with induced paramagnetic defect centers by ultraviolet or vacuum-ultraviolet photons in high-purity silica glasses. *Phys. Rev. B* **1993**, *48*, 15584–15594.

[144] T. Suzuki, L. Skuja, K. Kajihara, M. Hirano, T. Kamiya, H. Hosono. Electronic structure of oxygen dangling bond in glassy $SiO_2$: The role of hyperconjugation. *Phys. Rev. Letters* **2003**, *90*.

[145] L. Skuja, K. Kajihara, M. Hirano, H. Hosono. Visible to vacuum-UV range optical absorption of oxygen dangling bonds in amorphous $SiO_2$. *Phys. Rev. B* **2011**, *84*.

[146] H. Hosono, K. Kajihara, T. Suzuki, Y. Ikuta, L. Skuja, M. Hirano. Vacuum ultraviolet optical absorption band of non-bridging oxygen hole centers in $SiO_2$ glass. *Solid State Commun.* **2002**, *122*, 117–120.

[147] Y. Sakurai. Low temperature dependence of photoluminescence band near 2.0 eV in silica glass. *J. Appl. Phys.* **2000**, *87*, 755–759.

[148] L. Skuja. The origin of the intrinsic 1.9 eV luminescence band in glassy $SiO_2$. *J. Non-Cryst. Solids* **1994**, *179*, 51–69.

[149] L. Vaccaro, M. Cannas, R. Boscaino. Phonon coupling of non-bridging oxygen hole center with the silica environment: Temperature dependence of the 1.9 eV emission spectra. *Journal of Luminescence* **2008**, *128*, 1132–1136.

[150] L. Skuja, T. Suzuki, K. Tanimura. Site-selective laser-spectroscopy studies of the intrinsic 1.9-eV luminescence center in glassy $SiO_2$. *Phys. Rev. B* **1995**, *52*, 15208–15216.

[151] A. Amossov, A. Rybaltovsky. Oxygen-deficient centers in silica glasses: A review of their properties and structure. *J. Non-Cryst. Solids* **1994**, *179*, 75–83.

[152] V. Garino-Canina. *Comptes rendus de l'Academie des Sciences* **1954**, *238*, 1577.

[153] E. W. J. Mitchell, E. G. S. Paige. CXI. The optical effects of radiation induced atomic damage in quartz. *Philos. Mag.* **1956**, *1*, 1085–1115.

[154] A. J. Cohen. Neutron specific color center in fused silica and an impurity band of identical wavelength. *Phys. Rev.* **1957**, *105*, 1151–1155.

[155] E. P. O'Reilly, J. Robertson. Theory of defects in vitreous silicon dioxide. *Phys. Rev. B* **1983**, *27*, 3780–3795.

[156] H. Hosono, Y. Abe, H. Imagawa, H. Imai, K. Arai. Experimental evidence for the Si–Si bond model of the 7.6-eV band in $SiO_2$ glass. *Phys. Rev. B* **1991**, *44*, 12043–12045.

[157] H. Imagawa, T. Arai, H. Hosono, H. Imai, K. Arai. Reaction kinetics of oxygen-deficient centers with diffusing oxygen molecules in silica glass. *J. Non-Cryst. Solids* **1994**, *179*, 70–74.

[158] H. Imai, K. Arai, H. Hosono, Y. Abe, T. Arai, H. Imagawa. Dependence of defects induced by excimer laser on intrinsic structural defects in synthetic silica glasses. *Phys. Rev. B* **1991**, *44*, 4812–4818.

[159] L. Skuja, A. Streletsky, A. Pakovich. A new intrinsic defect in amorphous $SiO_2$: Twofold coordinated silicon. *Solid State Commun.* **1984**, *50*, 1069–1072.

[160] T.-E. Tsai, D. L. Griscom. On the structures of hydrogen-associated defect centers in irradiated high-purity *a*-$SiO_2$:OH. *J. Non-Cryst. Solids* **1987**, *91*, 170–179.

[161] V. Radtsig. *Kinet. Katal.* **1979**, *20*, 456.

[162] A. Amosov, S. Malyshkin. *Fizika i Khimiya Stekla* **1984**, *10*, 305–309.

[163] H. Nishikawa, R. Nakamura, Y. Ohki, Y. Hama. Enhanced photogeneration of $E'$ centers from neutral oxygen vacancies in the presence of hydrogen in high-purity silica glass. *Phys. Rev. B* **1993**, *48*, 2968–2973.

[164] V. A. Radzig, V. N. Bagratashvili, S. I. Tsypina, P. V. Chernov, A. O. Rybaltovskii. Photoinduced reactions of oxygen-deficient centers with molecular hydrogen in silica glasses. *J. Phys. Chem.* **1995**, *99*, 6640–6647.

[165] A. H. Edwards, G. Germann. Interaction of hydrogenated molecules with intrinsic defects in *a*-$SiO_2$. *Nucl. Instrum. Methods Phys. Res. B* **1988**, *32*, 238–247.

[166] R. Tohmon, H. Mizuno, Y. Ohki, K. Sasagane, K. Nagasawa, Y. Hama. Correlation of the 5.0- and 7.6-eV absorption bands in $SiO_2$ with oxygen vacancy. *Phys. Rev. B* **1989**, *39*, 1337–1345.

[167] M. Kohketsu, K. Awazu, H. Kawazoe, M. Yamane. Photoluminescence centers in VAD $SiO_2$ glasses sintered under reducing or oxidizing atmospheres. *Jpn. J. Appl. Phys.* **1989**, *28*, 615–621.

[168] L. N. Skuja, A. R. Silin, J. Mare. Decay time and polarization properties of luminescence centers in vitreous silica. *pss (a)* **1978**, *50*, K149–K152.

[169] J. H. Stathis, M. A. Kastner. Time-resolved photoluminescence in amorphous silicon dioxide. *Phys. Rev. B* **1987**, *35*, 2972–2979.

[170] L. Skuja. Isoelectronic series of twofold coordinated Si, Ge, and Sn atoms in glassy $SiO_2$: A luminescence study. *J. Non-Cryst. Solids* **1992**, *149*, 77–95.

[171] A. Anedda, F. Congiu, F. Raga, A. Corazza, M. Martini, G. Spinolo, A. Vedda. Time resolved photoluminescence of a centers in neutron irradiated $SiO_2$. *Nucl. Instrum. Methods Phys. Res. B* **1994**, *91*, 405–409.

[172] L. Skuja. Direct singlet-to-triplet optical absorption and luminescence excitation band of the twofold-coordinated silicon center in oxygen-deficient glassy $SiO_2$. *J. Non-Cryst. Solids* **1994**, *167*, 229–238.

[173] L. N. Skuja, A. N. Trukhin, A. E. Plaudis. Luminescence in germanium-doped glassy $SiO_2$. *pss (a)* **1984**, *84*, K153–K157.

[174] B. L. Zhang, K. Raghavachari. Photoabsorption and photoluminescence of divalent defects in silicate and germanosilicate glasses: First-principles calculations. *Phys. Rev. B* **1997**, *55*, R15993–R15996.

[175] G. Pacchioni, R. Ferrario. Optical transitions and EPR properties of two-coordinated Si, Ge, Sn and related H(I), H(II), and H(III) centers in pure and doped silica from *ab initio* calculations. *Phys. Rev. B* **1998**, *58*, 6090–6096.

[176] G. Pacchioni. *Ab initio* theory of point defects in $SiO_2$. In *Defects in $SiO_2$ and Related Dielectrics: Science and Technology*, Springer Netherlands (2000), pp. 161–195.

[177] V. O. Sokolov, V. B. Sulimov. Theory of twofold coordinated silicon and germanium atoms in solid silicon dioxide. *pss (b)* **1994**, *186*, 185–198.

[178] S. Agnello, R. Boscaino, M. Cannas, F. M. Gelardi, M. Leone. $\gamma$-ray-induced bleaching in silica: Conversion from optical to paramagnetic defects. *Phys. Rev. B* **2000**, *61*, 1946–1951.

[179] F. Gelardi, S. Agnello. Gamma rays induced conversion of native defects in natural silica. In *Defects in $SiO_2$ and Related Dielectrics: Science and Technology*, Springer Netherlands (2000), pp. 285–305.

[180] S. Agnello, R. Boscaino, F. L. Mattina, S. Grandi, A. Magistris. Hydrogen-related paramagnetic centers in Ge-doped sol-gel silica induced by $\gamma$-ray irradiation. *J. Sol-Gel Sci. Technol.* **2006**, *37*, 63–68.

[181] A. Paleari. Ge and SN doping in silica: Structural changes, optically active defects, paramagnetic sites. In *Defects in $SiO_2$ and Related Dielectrics: Science and Technology*, Springer Netherlands (2000), pp. 307–327.

[182] S. Girard, A. Alessi, N. Richard, L. Martin-Samos, V. De Michele, L. Giacomazzi, S. Agnello, D. Di Francesca, A. Morana, B. Winkler, I. Reghioua, P. Paillet, M. Cannas, T. Robin, A. Boukenter, Y. Ouerdane. Overview of radiation induced point defects in silica-based optical fibers. *Rev. Mod. Phys.* **2019**, *4*, 100032.

[183] A. Alessi, S. Agnello, D. Sporea, C. Oproiu, B. Brichard, F. Gelardi. Formation of optically active oxygen deficient centers in Ge-doped $SiO_2$ by $\gamma$- and $\beta$-ray irradiation. *J. Non-Cryst. Solids* **2010**, *356*, 275–280.

[184] D. Di Francesca, A. Boukenter, S. Agnello, S. Girard, A. Alessi, P. Paillet, C. Marcandella, N. Richard, F. Gelardi, Y. Ouerdane. X-ray irradiation effects on fluorine-doped germanosilicate optical fibers. *Opt. Mater. Express* **2014**, *4*, 1683.

[185] L. Skuja, A. Naber. Site-selective luminescence study of defects in gamma-irradiated glassy germanium dioxide. *Nucl. Instrum. Methods Phys. Res. B* **1996**, *116*, 549–553.

[186] V. B. Neustruev. Colour centres in germanosilicate glass and optical fibres. *J. Phys. Condens. Matter* **1994**, *6*, 6901–6936.

[187] L. N. Skuja. Photoluminescence of intrinsic defects in glassy $GeO_2$. two-fold coordinated Ge and nonbridging oxygen. *pss (a)* **1989**, *114*, 731–737.

[188] A. Alessi, S. Agnello, Y. Ouerdane, F. M. Gelardi. Dependence of the emission properties of the germanium lone pair center on Ge doping of silica. *J. Phys. Condens. Matter* **2010**, *23*, 015903.

[189] A. Alessi, S. Girard, C. Marcandella, S. Agnello, M. Cannas, A. Boukenter, Y. Ouerdane. X-ray irradiation effects on a multistep Ge-doped silica fiber produced using different drawing conditions. *J. Non-Cryst. Solids* **2011**, *357*, 1966–1970.

[190] L. Giacomazzi, L. Martin-Samos, A. Boukenter, Y. Ouerdane, S. Girard, N. Richard. Ge(2), Ge(1) and Ge-$E'$ centers in irradiated Ge-doped silica: A first-principles EPR study. *Opt. Mater. Express* **2015**, *5*, 1054.

[191] M. Fujimaki, T. Kasahara, S. Shimoto, N. Miyazaki, S. Tokuhiro, K. S. Seol, Y. Ohki. Structural changes induced by KrF excimer laser photons in $H_2$-loaded Ge-doped $SiO_2$ glass. *Phys. Rev. B* **1999**, *60*, 4682–4687.

[192] A. Alessi, S. Girard, M. Cannas, S. Agnello, A. Boukenter, Y. Ouerdane. Evolution of photo-induced defects in Ge-doped fiber/preform: Influence of the drawing. *Opt. Express* **2011**, *19*, 11680.

[193] D. L. Griscom. On the natures of radiation-induced point defects in $GeO_2$–$SiO_2$ glasses: Reevaluation of a 26-year-old ESR and optical data set. *Opt. Mater. Express* **2011**, *1*, 400.

[194] D. L. Griscom. A minireview of the natures of radiation-induced point defects in pure and doped silica glasses and their visible/near-IR absorption bands, with emphasis on self-trapped holes and how they can be controlled. *Phys. Res. Int.* **2013**, *2013*, 1–14.

[195] G. Pacchioni, C. Mazzeo. Paramagnetic centers in Ge-doped silica: A first-principles study. *Phys. Rev. B* **2000**, *62*, 5452–5460.

[196] S. Girard, J. Kuhnhenn, A. Gusarov, B. Brichard, M. V. Uffelen, Y. Ouerdane, A. Boukenter, C. Marcandella. Radiation effects on silica-based optical fibers: Recent advances and future challenges. *IEEE Transactions on Nuclear Science* **2013**, *60*, 2015–2036.

[197] J. C. Lagomacini, D. Bravo, A. Martn, F. J. López, P. Martn, Á. Ibarra. Growth kinetics of AlOHC defects in $\gamma$-irradiated silica glasses. *J. Non-Cryst. Solids* **2014**, *403*, 5–8.

[198] J. Griffiths, J. Owen, I. Ward. The structure of the colour centres in smoky quartz. *Proc. R. Soc. A* **1955**, *231*, 404–414.

[199] F. Sim, C. R. A. Catlow, M. Dupuis, J. D. Watts. *Ab initio* self-consistent-field molecular orbital calculations on defects associated with radiation damage in alpha quartz. *J. Chem. Phys.* **1991**, *95*, 4215–4224.

[200] G. Pacchioni, F. Frigoli, D. Ricci, J. A. Weil. Theoretical description of hole localization in a quartz al center: The importance of exact electron exchange. *Phys. Rev. B* **2000**, *63*.

[201] A. S. Zyubin, A. M. Mebel, S. H. Lin. Quantum chemical modeling of photoabsorption and photoluminescence of the $[AlO_4]^0$ defect in bulk $SiO_2$. *J. Chem. Phys.* **2003**, *119*, 11408–11414.

[202] H. Hosono, H. Kawazoe. Radiation-induced coloring and paramagnetic centers in synthetic $SiO_2$:Al glasses. *Nucl. Instrum. Methods Phys. Res. B* **1994**, *91*, 395–399.

[203] A. Alessi, A. Guttilla, S. Girard, S. Agnello, M. Cannas, T. Robin, A. Boukenter, Y. Ouerdane. Radiation effects on aluminosilicate optical fibers: Spectral investigations from the ultraviolet to near-infrared domains. *pss (a)* **2018**, *216*, 1800485.

[204] U. Hoppe, G. Walter, A. Barz, D. Stachel, A. C. Hannon. The P–O bond lengths in vitreous probed by neutron diffraction with high real-space resolution. *J. Phys. Condens. Matter* **1998**, *10*, 261–270.

[205] R. K. Brow. Review: The structure of simple phosphate glasses. *J. Non-Cryst. Solids* **2000**, *263-264*, 1–28.

[206] V. G. Plotnichenko, V. O. Sokolov, V. V. Koltashev, V. B. Sulimov, E. M. Dianov. UV-irradiation-induced structural transformation in phosphosilicate glass fiber. *Opt. Lett.* **1998**, *23*, 1447.

[207] D. W. J. Cruickshank. 1077. The role of 3*d*-orbitals in $\pi$-bonds between (a) silicon, phosphorus, sulphur, or chlorine and (b) oxygen or nitrogen. *J. Chem. Soc.* **1961**, 5486–5504.

[208] K. A. R. Mitchell. Use of outer *d* orbitals in bonding. *Chem. Rev.* **1969**, *69*, 157–178.

[209] M. Fanciulli, E. Bonera, S. Nokhrin, G. Pacchioni. Phosphorousoxygen hole centers in phosphosilicate glass films. *Phys. Rev. B* **2006**, *74*.

[210] L. Giacomazzi, L. Martin-Samos, A. Alessi, M. Valant, K. C. Gunturu, A. Boukenter, Y. Ouerdane, S. Girard, N. Richard. Optical absorption spectra of P defects in vitreous silica. *Opt. Mater. Express* **2018**, *8*, 385.

[211] D. L. Griscom, E. J. Friebele, K. J. Long, J. W. Fleming. Fundamental defect centers in glass: Electron spin resonance and optical absorption studies of irradiated phosphorus-doped silica glass and optical fibers. *J. Appl. Phys.* **1983**, *54*, 3743–3762.

[212] G. Origlio, F. Messina, M. Cannas, R. Boscaino, S. Girard, A. Boukenter, Y. Ouerdane. Optical properties of phosphorus-related point defects in silica fiber preforms. *Phys. Rev. B* **2009**, *80*.

[213] H. Hosono, K. Kajihara, M. Hirano, M. Oto. Photochemistry in phosphorus-doped silica glass by ArF excimer laser irradiation: Crucial effect of $H_2$ loading. *J. Appl. Phys.* **2002**, *91*, 4121–4124.

[214] H. Hosono, K.-I. Kawamura, M. Hirano. Defect formation in $SiO_2$:$P_2O_5$ glasses by excimer laser irradiation: Effects of hydrogen loading. In *Bragg Gratings Photosensitivity and Poling in Glass Waveguides* (2001).

[215] D. Di Francesca, S. Girard, S. Agnello, A. Alessi, C. Marcandella, P. Paillet, Y. Ouerdane, Y. Kadi, M. Brugger, A. Boukenter. Combined temperature radiation effects and influence of drawing conditions on phosphorous-doped optical fibers. *pss (a)* **2018**, *216*, 1800553.

[216] G. Pacchioni, D. Erbetta, D. Ricci, M. Fanciulli. Electronic structure of defect centers P1, P2, and P4 in P-doped $SiO_2$. *J. Phys. Chem. B* **2001**, *105*, 6097–6102.

[217] F. Paredes, F. M. Montagnino, P. Salinari, G. Bonsignore, S. Milone, S. Agnello, M. Barbera, F. M. Gelardi, L. Sciortino, A. Collura, U. L. Cicero, M. Cannas. Combined heat and power generation with a HCPV system at 2000 suns. In *AIP Conference Proceedings **1679** 100003* (2015).

[218] L. Sciortino, S. Agnello, M. Barbera, G. Bonsignore, A. Buscemi, R. Candia, M. Cannas, A. Collura, G. D. Cicca, F. M. Gelardi, U. L. Cicero, F. M. Montagnino, G. Napoli, F. Paredes, L. Spallino, S. Varisco. Direct sunlight facility for testing and research in HCPV. In *AIP Conference Proceedings **1616** 158* (2014).

[219] G. Bonsignore, A. A. Gallitto, S. Agnello, M. Barbera, R. Candia, M. Cannas, A. Collura, I. Dentici, F. M. Gelardi, U. L. Cicero, F. M. Montagnino, F. Paredes, L. Sciortino. Electrical-optical characterization of multijunction solar cells under 2000× concentration. In *AIP Conference Proceedings **1616** 102* (2014).

[220] G. Bonsignore, A. A. Gallitto, S. Agnello, M. Barbera, F. M. Gelardi, L. Sciortino, A. Collura, U. L. Cicero, S. Milone, F. M. Montagnino, F. Paredes, M. Cannas. CHP efficiency of a 2000× CPV system with reflective optics. In *AIP Conference Proceedings **1679** 050004* (2015).

[221] E. Shittu, F. Paredes, B. Schiavo, L. Venezia, S. Milone, F. Montagnino, M. Kolokotroni. Comparison of operational performance and analytical model of high concentrator photovoltaic thermal system at 2000 concentration ratio. *E3S Web of Conferences* **2019**, *111*, S. Tanabe, H. Zhang, J. Kurnitski,

M. G. da Silva, I. Nastase, P. Wargocki, G. Cao, L. Mazzarela, C. Inard (Eds), 06007.

[222] D. Buie, A. Monger, C. Dey. Sunshape distributions for terrestrial solar simulations. *Sol. Energy* **2003**, *74*, 113–122.

[223] A. April, P. Bilodeau, M. Piché. Focusing a TM_01 beam with a slightly tilted parabolic mirror. *Opt. Express* **2011**, *19*, 9201.

[224] Filmetrics. Refractive Index Database. Available online: *https://www.filmetrics.com/refractive-index-database*

[225] C. Pruss, E. Garbusi, W. Osten. Testing aspheres. *Optics and Photonics News* **2008**, *19*, 24.

[226] S. Girard, A. Alessi, N. Richard, L. Martin-Samos, V. D. Michele, L. Giacomazzi, S. Agnello, D. D. Francesca, A. Morana, B. Winkler, I. Reghioua, P. Paillet, M. Cannas, T. Robin, A. Boukenter, Y. Ouerdane. Overview of radiation induced point defects in silica-based optical fibers. *Rev. Mod. Phys.* **2019**, *4*, 100032.

[227] G. Origlio, F. Messina, M. Cannas, R. Boscaino, S. Girard, A. Boukenter, Y. Ouerdane. Optical properties of phosphorus-related point defects in silica fiber preforms. *Phys. Rev. B* **2009**, *80*.

[228] D. D. Francesca, S. Girard, S. Agnello, A. Alessi, C. Marcandella, P. Paillet, Y. Ouerdane, Y. Kadi, M. Brugger, A. Boukenter. Combined temperature radiation effects and influence of drawing conditions on phosphorous-doped optical fibers. *pss (a)* **2018**, *216*, 1800553.

[229] L. Skuja, K. Kajihara, K. Smits, A. Silins, H. Hosono. Luminescence and raman detection of molecular cl2 and ClClO molecules in amorphous SiO2 matrix. *J. Phys. Chem. C* **2017**, *121*, 5261–5266.

[230] A. Alessi, S. Girard, C. Marcandella, L. Vaccaro, M. Cannas, A. Boukenter, Y. Ouerdane. Influence of the manufacturing process on the radiation sensitivity of fluorine-doped silica-based optical fibers. *IEEE Transactions on Nuclear Science* **2012**, *59*, 760–766.

[231] D. L. Griscom. Trapped-electron centers in pure and doped glassy silica: A review and synthesis. *J. Non-Cryst. Solids* **2011**, *357*, 1945–1962.

[232] V. D. Michele, C. Marcandella, D. D. Francesca, P. Paillet, A. Alessi, M. Cannas, Y. Ouerdane, A. Boukenter, S. Girard. Pulsed x-ray radiation responses of solarization-resistant optical fibers. *pss (a)* **2018**, *216*, 1800487.

[233] T. Smith, J. Guild. The c.i.e. colorimetric standards and their use. *Transactions of the Optical Society* **1931**, *33*, 73–134.

[234] M. Bertalmo. Colour representation and colour gamuts. In *Vision Models for High Dynamic Range and Wide Colour Gamut Imaging*, Elsevier (2020), pp. 131–155.

[235] D. L. MacAdam. Visual sensitivities to color differences in daylight. *Journal of the Optical Society of America* **1942**, *32*, 247.

La borsa di dottorato è stata cofinanziata con risorse del
Programma Operativo Nazionale Ricerca e Innovazione 2014-2020 (CCI 2014IT16M2OP005),
Fondo Sociale Europeo, Azione I.1 “Dottorati Innovativi con caratterizzazione Industriale”

UNIONE EUROPEA
Fondo Sociale Europeo

Ministero dell'Università e della Ricerca